Light-Absorbing Carbonaceous Particles in Urban Regions: Physicochemical Properties and the Application of Data-Driven Modeling

Houjie Li

Department of Chemistry

McGill University

Montreal, Quebec, Canada

April 2024

A thesis submitted to McGill University in partial fulfillment of the requirements of the degree of Doctor of Philosophy

Acknowledgement

I would like to thank my supervisor, Professor Parisa A. Ariya, for continuously supporting me during my journey of pursuing my PhD degree, for her mentorship and patience to allow me to build up my academic skills. Thanks to my review committee members, Professor Thomas Preston and Professor Janine Mauzeroll, for their help and advice.

I would also like to thank my past and current research group members Yevgen Nazarenko, Rodrigo Rangel-Alvarado, Ryan Hall, Mattie Hibbs, Benilde Mizero, Zaki Nasreddine, Negin Rezaei Nokandeh, Sandeep Bose, and Swarbhanu Ghosh for their assistance with laboratory work, research discussions, and emotional support over the course of my degree. I would especially like to thank Zi Wang and Devendra Pal for supporting me and providing me advice. I would also like to thank Robert Panetta for his splendid help managing our laboratory and collaboration on my research. I thank the staff from the chemistry department, especially Chantal Marotte, and Dr. David Liu from the Facility for Electron Microscopy Research, for their help making both my degree and experimental progress easier during these years.

I am also thankful to my friends from McGill Kendo Club for our wonderful memory of kendo practice and trips: Zhuoqun Zhou, William Wong, Lesley Roberts, Vincent Trinh, Yantong Chen, Muzhi Qi, Ell Kwon, Simon Lecoq, Muhang Li, Jingyang Jiang, Maria Manea, Hajar Ouali, Zoe Zhou, Mohib Hossain, Priscilia Momo, and Simon Bruins. I wish we could explore more in the world of kendo altogether and enjoy our kendo life forever.

Thanks to my friends in China who always treated me as a brother: Jinyang Guo, Yajie Hu, Qi Zheng, Yiren Chen, Wenhao Wu, Lei Huang, Chen Zhu, Chengxi Huang, Yiwen Han, Manning Wang.

Finally, I must thank my wonderful family for their constant understanding and support during my time at McGill and all the years of my life.

Statement of Originality

This thesis contains original research and represents distinct contributions to knowledge in the field of aerosol science and environmental science as follows:

Black carbon characteristics in urban cold climate settings and impact of COVID-19 (Chapter 2).

- First, we acquired the datasets of one-year real-time black carbon (BC) mass concentration by using photoacoustic extinctiometer (PAX) and co-pollutants including $PM_{2.5}$, NO_x, O_3, and CO in Montreal, a cold-climate city. We found that BC mass concentration exhibited a bimodal distribution with a summer peak and a long winter peak, and the winter peak could last more than 3 months. Furthermore, A comparative study between two air pollution hotspots, downtown and the Montreal international airport, indicated that BC mass concentrations at the airport were over 400% higher, revealing the significant contribution of aviation to BC emission.
- A case study of COVID-19 was carried out by comparing the emissions of BC and other air pollutants before, during, and after COVID-19 lockdown. The results demonstrated a sharp decrease of each pollutant except O_3 during the lockdown, highlighting the significant impact of anthropogenic sources in urban regions.
- This study offers the first long-term BC dataset in urban cold-climate regions where BC data are still scarce. This dataset is crucial for improving air quality and climate models and assessing health effects of BC.

Black carbon and brown carbon in urban regions and impact of wildfires (Chapter 3).

- In this work, we presented unique one-year observation data on the variations of BC, BrC, and their absorption coefficients from July 2022 to July 2023, covering the period of significant forest fires in the north of Eastern Canada. The bimodal seasonal trends of BC and BrC confirmed the summer and winter peaks.
- During the summer of 2023, the record-breaking wildfires which occurred in North Quebec were analyzed. Our results confirmed that wildfires, as an important format of biomass burning, not only increased the concentration of BC, but also emitted a large amount of BrC which dominated the light absorption at short wavelengths.

- This study highlighted the significant impacts of wildfires which are expected to increase globally due to climate change. This study provides important datasets and insights into the complicated situation of air pollution in urban regions under the threat of wildfires.

The application of data-driven modeling on simulating black carbon concentration (Chapter 4).

- We developed a machine learning model based on recurrent neural network and long short-term memory algorithm to simulate the variation of black carbon. The input data included concentrations of $PM_{2.5}$, NO_x, O_3, and CO, whereas the output data were concentrations of BC.
- This study provides a method to estimate BC mass concentration in situations where BC data are unavailable but other common air pollutants are measured. It can enrich BC data for areas where BC measurement is still scarce and facilitate a comprehensive evaluation of BC mass concentration in urban environments and beyond.

Abstract

Light-absorbing carbonaceous particles (LACs), consisting of black carbon (BC) and brown carbon (BrC), are a group of radiatively-active aerosols which could significantly impact the environment and climate by absorbing solar radiation, darkening snow/ice surfaces, and serving as cloud condensation nuclei or ice nuclei. Yet the climate and health effects of LACs remain uncertain because of insufficient measurements of their physicochemical properties. In urban areas, anthropogenic emissions are the predominant sources of LACs, but natural sources such as wildfires can also contribute to LAC emissions. Studying the seasonal trend of LACs in cities is crucial for developing targeted policies to mitigate air pollution and reduce exposure of residents to LACs. Furthermore, the occurrence of wildfires worldwide is rising sharply due to climate change. LACs emitted by wildfires could undergo long range transport from their origins to urban areas, complicating the understanding of urban air pollution. To systematically evaluate the total effects of LACs on the climate and human health, it is essential to conduct more thorough observation on the physicochemical properties and emission sources of LACs.

This thesis presents the mass concentrations and absorption coefficients of BC and BrC, as well as their spatial-temporal variations in Montreal, a cold-climate city facing an increasing threat of wildfires, but the measurement of LACs is still scare. The first work used one-year real-time observation of BC and other co-pollutants to demonstrate a bimodal distribution of BC mass concentration, showing a winter peak lasting more than 3 months in addition to a summer peak. Comparisons between downtown Montreal and the Montreal internation airport revealed that average BC mass concentration near the airport was 4 times higher than the concentration in downtown Montreal. The COVID-19 pandemic lockdown caused a drastic drop of concentrations

of BC and other air pollutants by up to 72%, revealing the significant anthropogenic influence on urban air pollution.

The second study presents one-year variations of LAC mass concentration and absorption coefficients during July 2022 to July 2023. We firstly demonstrated the seasonal trend of LACs in Montreal. Secondly, data from June and July 2023 revealed smokes from wildfire brought a large proportion of primary BrC and secondary BrC precursors and increased BC mass concentration by over 26% in Montreal. Although fossil fuel combustion is usually the major source of LACs in urban areas, when biomass burning became the predominant source, BrC could contribute over 50% of total light absorption at 370 nm wavelength with secondary BrC accounting for more than 20% of BrC absorption. This clearly demonstrates the significant importance of BrC on light absorption.

In the third part of the dissertation, we developed a machine learning (ML) model to predict BC mass concentration based on common air pollutants including CO, NO_x, $PM_{2.5}$ and O_3. The World Health Organization (WHO) has suggested that monitoring BC mass concentration is necessary, considering the unique health and climate effects of BC. However, purchasing new instruments for BC at each air quality station would require a large amount of budget, which makes it difficult to achieve. Thus, we developed a ML model based on recurrent neural network and long short-term memory algorithms which are good at capturing long term patterns and making more accurate prediction. We trained and tested our model with four years of data and demonstrated its high performance with one year of new data.

This thesis contributes to the understanding of sources, variations and properties of LACs in Montreal, a cold-climate site where winter can last 5 months, and provided results that will help understand their effects on climate and human health. With increasing emissions from

anthropogenic sources and more frequent summer wildfires, keeping observations of LACs in urban regions will help to mitigate climate change and improve air quality, protecting people from potential hazards.

Résumé

Les particules carbonées absorbant la lumière (LAC), composées de carbone noir (BC) et de carbone brun (BrC), sont un groupe d'aérosols radiativement actifs qui peuvent avoir un impact significatif sur l'environnement et le climat en absorbant le rayonnement solaire, en assombrissant les surfaces de neige/glace et en servant de noyaux de condensation des nuages ou de noyaux de glace. Cependant, les effets des LACs sur le climat et la santé restent incertains en raison de mesures insuffisantes de leurs propriétés physico-chimiques. Dans les zones urbaines, les émissions anthropiques sont les principales sources de LACs, mais des sources naturelles telles que les feux de forêt peuvent également contribuer aux émissions de LACs. Étudier la tendance saisonnière des LACs dans les villes est crucial pour développer des politiques ciblées visant à atténuer la pollution de l'air et à réduire l'exposition des résidents aux LACs. De plus, la fréquence des feux de forêt dans le monde augmente fortement en raison du changement climatique. Les LACs émis par les feux de forêt peuvent subir un transport à longue distance depuis leurs origines jusqu'aux zones urbaines, compliquant la compréhension de la pollution atmosphérique urbaine. Pour évaluer systématiquement les effets totaux des LACs sur le climat et la santé humaine, il est essentiel de mener des observations plus approfondies sur les propriétés physico-chimiques et les sources d'émission des LACs.

Cette thèse présente les concentrations massiques et les coefficients d'absorption du BC et du BrC, ainsi que leurs variations spatio-temporelles à Montréal, une ville au climat froid confrontée à une menace croissante de feux de forêt, mais la mesure des LACs reste rare. Le premier travail a utilisé une année d'observation en temps réel du BC et d'autres co-polluants pour démontrer une distribution bimodale de la concentration massique de BC, montrant un pic hivernal

durant plus de 3 mois en plus d'un pic estival. Les comparaisons entre le centre-ville de Montréal et l'aéroport international de Montréal ont révélé que la concentration massique moyenne de BC près de l'aéroport était 4 fois plus élevée que la concentration au centre-ville de Montréal. Le confinement dû à la pandémie de COVID-19 a provoqué une baisse drastique des concentrations de BC et d'autres polluants atmosphériques jusqu'à 72%, révélant l'influence anthropique significative sur la pollution atmosphérique urbaine.

La deuxième étude présente les variations sur un an de la concentration massique de LAC et des coefficients d'absorption de juillet 2022 à juillet 2023. Nous avons d'abord démontré la tendance saisonnière des LACs à Montréal. Ensuite, les données de juin et juillet 2023 ont révélé que les fumées des feux de forêt apportaient une grande proportion de BrC primaire et de précurseurs de BrC secondaire et augmentaient la concentration massique de BC de plus de 26% à Montréal. Bien que la combustion de combustibles fossiles soit généralement la principale source de LACs dans les zones urbaines, lorsque la combustion de biomasse devient la source prédominante, le BrC peut contribuer à plus de 50% de l'absorption totale de la lumière à une longueur d'onde de 370 nm, le BrC secondaire représentant plus de 20% de l'absorption du BrC. Cela démontre clairement l'importance significative du BrC sur l'absorption de la lumière.

Dans la troisième partie de la thèse, nous avons développé un modèle d’apprentissage machine (AM) pour prédire la concentration massique de BC en fonction des polluants atmosphériques courants tels que le CO, les NO_x, les $PM_{2.5}$ et l'O_3. L'Organisation Mondiale de la Santé (OMS) a suggéré que la surveillance de la concentration massique de BC est nécessaire, compte tenu des effets uniques du BC sur la santé et le climat. Cependant, l'achat de nouveaux instruments pour le BC à chaque station de qualité de l'air nécessiterait un budget important, ce

qui rend difficile sa réalisation. Ainsi, nous avons développé un modèle de AM basé sur des algorithmes de réseau neuronal récurrent et de mémoire à court terme long (MCTL) qui sont bons pour capturer les modèles à long terme et faire des prédictions plus précises. Nous avons entraîné et testé notre modèle avec quatre ans de données et démontré ses performances élevées avec une année de nouvelles données.

Cette thèse contribue à la compréhension des sources, des variations et des propriétés des LACs à Montréal, un site au climat froid où l'hiver peut durer 5 mois, et a fourni des résultats qui aideront à comprendre leurs effets sur le climat et la santé humaine. Avec des émissions croissantes provenant de sources anthropiques et des feux de forêt estivaux plus fréquents, continuer à observer les LACs dans les régions urbaines aidera à atténuer le changement climatique et à améliorer la qualité de l'air, protégeant les personnes des dangers potentiels.

Table of Content

List of Figures

List of Tables

List of abbreviations

AAE	Absorption Ångström Exponent
AE43	Aethalometer, Model 43
AMS	Aerosol Mass Spectrometer
AMS	Aerosol Mass Spectrometry
ANN	Artificial Neural Network
APCI	Atmospheric pressure chemical ionization
B_{abs} (λ)	Absorption coefficient at the wavelength of λ
BB	Biomass Burning
BC	Black Carbon
B_{ext} (λ)	Extinction coefficient at the wavelength of λ
BrC	Brown Carbon
B_{scat} (λ)	Scattering coefficient at the wavelength of λ
CCN	Cloud Condensation Nuclei
CFI	Canadian Foundation for Innovation
CMT	Chemical Transport Model
CNN	Convolutional Neural Network
COVID-19	SARS-CoV-2 coronavirus caused disease
EC	Elemental Carbon
ECCC	Environment and Climate Change Canada
EDS	Energy-Dispersive X-ray Spectroscopy
ESI	Electrospray ionization
FEMR	Facility for Electron Microscopy Research
FF	Fossil Fuel combustion
GC-MS	Gas Chromatography-Mass Spectrometry
GCS	Glassy Carbon Spheres
GEOS-Chem	Goddard Earth Observing System coupled to Chemistry
GMAO	Global Modeling and Assimilation Office
HPLC-MS	High Performance Liquid Chromatography-Mass Spectrometry

HR-S/TEM-EDS	High-Resolution Scanning/Transmission Electron Microscopy with Energy Dispersive X-ray Spectroscopy
HULIS	Humic-like substances
ICAO	International Civil Aviation Organization
IN	Ice Nuclei
IPCC	International Panel on Climate Change
IUPAC	International Union of Pure and Applied Chemistry
LACs	Light-Absorbing Carbonaceous Particles
LSTM	Long Short-Term Memory
LUR	Land Use Regression
MAAP	Multi-Angle Absorption Photometer
MAC (λ)	Mass Absorption Cross-section at the wavelength of λ
MAE	Mean Absolute Error
MAE (λ)	Mass Absorption Efficiency at the wavelength of λ
M-BrC	Moderately absorptive BrC
MERRA-2	The Modern-Era Retrospective analysis for Research and Applications, Version 2
ML	Machine Learning
MOUDI	Micro Orifice Uniform Deposit Impactor
MRS	Minimum R-Square
MS	Mass Spectroscopy
MSE	Mean Square Error
NAPS	National Air Pollution Surveillance Program
NASA	National Aeronautics and Space Administration
NSERC	National Science and Engineering Research of Canada
NSERC CREATE PURE	National Sciences and Engineering Council of Canada - Collaborative Research and training Experience Program - Pollution in Urban Environments
OA	Organic Aerosols
OC	Organic Carbon
PAHs	Polycyclic Aromatic Hydrocarbons

PAS	Photoacoustic Spectrometer
PASS	Photoacoustic Soot Spectrometer
PAX	Photoacoustic extintiometer
PBL	Planetary Boundary Layer
PM	Particulate Matter
$PM_{2.5}$	Particulate Matter with aerodynamic diameter less than 2.5 μm
POA	Primary Organic Aerosols
PSAP	Particle Soot Absorption Photometer
R^2	Correlation coefficient
RF	Random Forest
RH	Relative Humidity
RMSE	Root Mean Square Error
RNN	Recurrent Neural Network
RSQA	Air Quality Monitoring Network
S/TEM or (S)TEM	Scanning/Transmission Electron Microscopy
S-BrC	Strongly absorptive BrC
SEM	Scanning Electron Microscopy
SOA	Secondary Organic Aerosols
SP2	Single Particle Soot Photometer
SP-AMS	Soot Particle-Aerosol Mass Spectrometry
SSA	Single Scattering Albedo
SVM	Support Vector Machine
SVR	Support Vector Regression
TEM	Transmission Electron Microscopy
UV	Ultra-violet
VOCs	Volatile Organic Compounds
VW-BrC	Very Weakly absorptive BrC
W-BrC	Weakly absorptive BrC
WHO	World Health Organization
WRF-Chem	Weather Research and Forecasting model coupled to Chemistry
WSOC	Water-Soluble Organic Carbon

XGBoost	eXtreme Gradient Boosting
YUL Airport	Montréal-Pierre-Elliott-Trudeau International Airport

Chapter 1 Introduction

1.1 Atmospheric Aerosols

Aerosols are solid particles and/or liquid suspended in the atmosphere. Since aerosols are also interchangeable with particulate matter (PM) when focusing on particles suspended in the air, these two terms are used interchangeably throughout this thesis. Aerosols are emitted from a large variety of anthropogenic and natural sources, which contributes to the complex chemical compositions and various physicochemical properties of aerosols, such as size, morphology, optical properties, and hygroscopicity. The size of aerosols ranges from a few nanometers to several tens of micrometers, which strongly affects the properties, health effects, and climate effects of aerosols. Yet aerosols are short-lived relative to greenhouse gases, on the order of days to several weeks in the atmosphere, therefore their effects on the environment and climate tend to be mostly local or regional. The short lifetime brings significant uncertainty when evaluating the total impact of aerosols on human health and climate. Thus, the World Health Organization (WHO) and the Intergovernmental Panel on Climate Change (IPCC) have suggested to do thorough research on the physical and chemical properties of aerosols to comprehensively evaluate their impacts on climate change and human health (IPCC 2021; WHO 2021a).

Depending on the formation process, aerosols enter the atmosphere directly as primary particles or indirectly as products of secondary particle formation by gas-particle conversion. Primary particles are emitted by anthropogenic and natural sources directly into the atmosphere. For instance, black carbon (BC) particles are emitted from vehicles and industries in urban regions or emitted by wildfires as product of biomass burning. Wind brings a large amount of mineral dust from soil and deserts to the earth's surface every year. Sea-spray aerosols are directly ejected into

the atmosphere, which is another example of natural sources. In addition, biota also contributes bioaerosols such as bacteria and fungi as primary particles. Forests, especially rainforests, emit a large proportion of organic aerosols (OA), for example terpene and isoprene, which could undergo photochemical and heterogeneous reactions. Meanwhile, secondary particle formation includes oxidation of NO_x and SO_2 to generate nitrate and sulfate, and formation of secondary organic aerosol (SOA) from volatile organic compounds (VOC). It is noteworthy that primary particles and secondary particles are not isolated. Instead, aerosols are usually complex mixtures of both primary and secondary particles, and the mixtures can be internally mixed, externally mixed or both, which further complicates their physicochemical properties and impacts on the climate.

As air pollutants, aerosols or PM have been proved to cause a series of adverse effects on human health. The WHO suggests that ambient air pollutant is estimated to have caused 4.2 million premature deaths worldwide per year by inducing heart disease, stroke, pulmonary disease, respiratory disease, and other chronic diseases (WHO 2021a). Unfortunately, 99% of the global population lives where air pollution levels are worse than the WHO air quality guideline suggested. There is abundant evidence showing the health effects of PM, especially $PM_{2.5}$ (particulate matter with an aerodynamic diameter less than 2.5 μm) (Thornburg et al., 2021; Vreeland et al., 2016; Wen et al., 2023a; Wen et al., 2023b; X Zhang et al., 2023a). In addition, some anthropogenic OA, such as polycyclic aromatic hydrocarbons (PAHs), have been confirmed carcinogens (Fang et al., 2021; Kitanovski et al., 2021; Lenssen et al., 2022).

Apart from health effects, aerosols can impact the climate directly via aerosol-radiation effects, or indirectly via aerosol-cloud effects. Most aerosols, such as sulfate and most organic aerosols, scatter solar radiation in the atmosphere, cooling the Earth's surface. However, BC, light-

absorbing organic carbon which is also named “brown carbon” (BrC), and mineral dust could absorb solar radiation, which have warming effects on the climate.

As for aerosol-cloud effects, aerosols can act as cloud condensation nuclei (CCN) upon which cloud droplets can be formed. An increase of aerosol concentrations will lead to an increase of CCN concentrations, and thus an augment of cloud droplet concentrations. An increase in cloud droplet concentrations results in smaller cloud droplets but increases the total scattering cross section, and therefore amplifies the cloud reflectivity and cloud lifetime, causing a cooling effect. Water-soluble aerosols, such as sulfate, nitrate, sea salt, and SOA, tend to be efficient CCN, making them play more important roles in aerosol-cloud interactions than water-insoluble aerosols such as BC and mineral dust. However, smaller cloud droplets will evaporate more quickly, which enhances the mixing of clouds and ambient dry air, leading to a warming effect. On the other hand, some aerosols are good ice nucleating particles (INPs) which can facilitate heterogeneous ice nucleation, forming ice clouds in the atmosphere. The aerosol-ice-cloud interaction is more complex and less understood, especially when considering the competing effects of homogeneous ice nucleation by liquid droplets and heterogeneous ice nucleation by INPs. An increase of INP concentrations in ice clouds could lead to either a warming or a cooling effect depending on which ice nucleation pathway dominates the formation of the clouds. Overall, the aerosol-cloud interaction contributes to a net cooling effect (IPCC 2021).

1.2 Light absorbing carbonaceous particles (LACs) as a unique type of aerosols

Light-absorbing carbonaceous particles (LACs), including BC and BrC, are one of the most important types of aerosols because they are one of the radiatively-active components in the Earth’s

atmosphere (Liu et al., 2020). LACs can absorb light from ultraviolet (UV) to near infrared (IR), darken the surface of snow/ice, act as CCN and INP, leading to warming effects on the climate system. LACs are ubiquitously emitted from anthropogenic and natural sources. They undergo various processes in the atmosphere, such as forming clouds and precipitation, and photochemical and heterogenous reactions which can alter the properties and lifetime of LACs. Meanwhile, it is likely that LACs will be transported great distances from the emission sources, termed "long-range atmospheric transport" (LRAT). During LRAT, LACs can be deposited on the Earth's surface via dry or wet deposition. Wet deposition is the main deposition pathway of LACs. For instance, Serving as CCN or INPs to form cloud droplets or snow is one of essential wet deposition formats. Additionally, LACs that remain suspended in the atmosphere can be scavenged by precipitation like rain droplets or snowflakes. As for dry deposition, with the particle size and weight gradually increasing, it is more likely for LACs to be deposited by wind and gravity. Because of LRAT, LACs can be deposited in the remote cryosphere such as Arctic and Tibetan Plateau where both human activities and local emission sources of LACs are very limited, affecting regional and global climate in the end.

In the following sections, "LACs" will be used when describing the common properties. "BC" and "BrC" will be used when discussing their own unique properties, respectively.

1.2.1 Source of LACs

BC is the by-product of fossil fuel combustion and biomass burning. Thus, BC is predominantly emitted from primary sources such as transportation, industry, and open burning of forests and savannas. The total global emission of BC is estimated to be 7.5 Tg/year in the year of

2000 with an uncertainty range of 2 to 29 Tg/year (Bond et al. 2013). Fig. 1.1A provides a summary of global BC emission sources. Among these sources, the largest is the open burning of forests, savannas, and agricultural residues, which contributes to around 2.7 Tg/year globally. The remaining emissions are from anthropogenic energy-related combustion. It is noteworthy that contributions from aviation and marine shipping emissions account for less than 9% of total BC emissions. However, since they usually occur at high altitudes and/or remote oceans, where BC emissions are scarce, they play a significant role in climate forcing and are therefore considered more climatically sensitive (Liu et al., 2020). In addition, the major BC emission source varies with location and tends to be region-specific. For example, the dominant sources of BC in Asia and Africa is combustion of residential solid fuels (e.g., coal and agricultural residues) which accounts for 60% to 80% of BC emissions. But in Europe, North America, and Latin America, about 70% of BC emissions come from diesel engines. It is evident that anthropogenic sources of BC emissions are correlated with the development of countries, reflecting the global inequality with respect to climate change contribution and impacts.

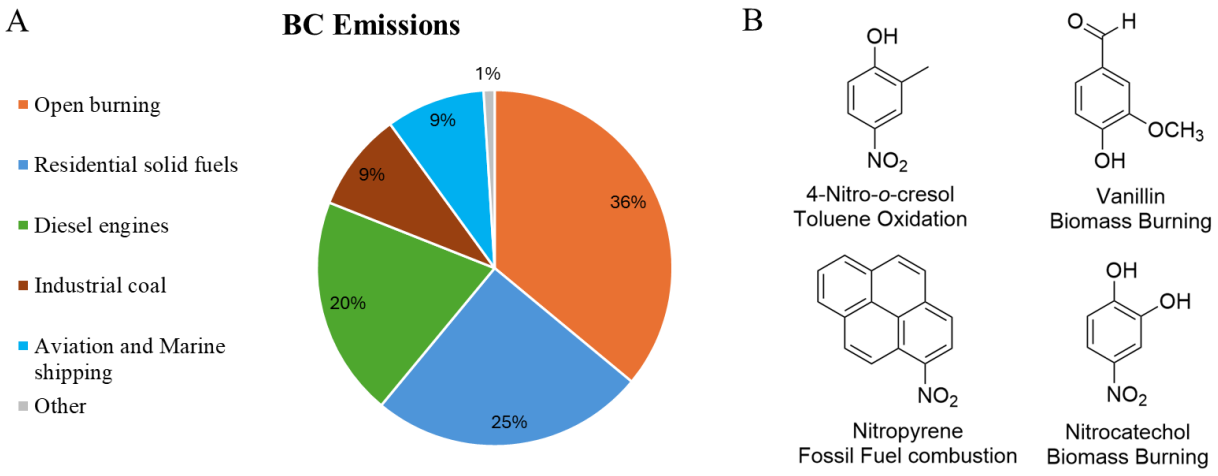

Figure 1.1. (A) Global BC emission sources and (B) representative BrC components.

The sources of BrC are more diverse than BC. Although biomass burning is the predominant and primary source, BrC can also be generated by various secondary sources. Fig. 1.1B demonstrates some representative BRC components and their sources. Depending on their origins, BrC particles demonstrate a large variation in optical and chemical properties. For example, Humic-like substances (HULIS) are one of major components of BrC which can be emitted from biomass burning or formed via secondary reactions from VOC (Wu et al., 2018). Anthropogenic sources in urban regions such as diesel engines primarily emit polycyclic aromatic hydrocarbons (PAHs) which are also considered as precursors of nitro-PAHs (a type of BrC) via heterogeneous oxidation with NO_3 radical (Saleh, 2020). There is currently no systematic inventory of BrC emissions because the complex and varied nature of BrC makes it a difficult class to systematically define.

1.2.2 Microphysical properties of LACs

Most BrC components are amorphous and unstable under electron beams and high vacuum, exacerbating their characterization. Therefore, it is inappropriate to generally discuss the size and morphology of BrC particles. However, there is one prominent component of BrC, so-called “tar ball”, which is a large homogeneous particle and stable enough to be detected by transmission electron microscopy (TEM). As is shown in Fig. 1.2A, a single particle of tar balls is usually spherical with a diameter in the nanometer range. But tar balls could also group together to form agglomerates achieving micron size.

As mentioned above, the emission sources strongly influence the properties of BrC particles. Herein we will treat BrC and BC particles based on their light absorption properties as

shown in Fig. 1.3. As the mass absorption cross-section (MAC) increases, the molecular size of BrC composing the particles becomes larger, and in return, the particles become more stable and more absorptive. In contrast, BrC particles with a smaller MAC show weaker light absorption and tend to be more volatile and more soluble in water or common organic solvents such as methanol and acetone. Tar balls and HULIS are regarded as two groups of strongly absorptive BrC particles (S-BrC), whereby tar balls are probably the most absorptive and most refractory BrC particles.

Fig. 1.3 shows the transition from very weekly absorptive BrC (VW-BrC) to BC, and tar balls are closest to BC (Saleh, 2020). Indeed, BC is more refractory than tar balls with vaporization temperature approaching 4000 K. BC demonstrates strong light absorption from UV to near infrared, whereas BrC strongly absorb light with shorter wavelength but with negligible absorption above 500 nm. Furthermore, BC is insoluble in either water or organic solvents. BC exists as an aggregate of small spheres with diameters in tens of nanometers. However, the size and morphology of the aggregate varies as indicated by Fig. 1.2B, C, and D with size ranging from a few nanometers to 2 μm, peaking at 150 to 200 nm (Li et al., 2024). Thus, BC particles are considered as a subset of $PM_{2.5}$. Freshly emitted BC aggregates tend to be chain-like. During LRAT, BC aggregates may servs as CCN or INPs, which can alter their morphology, making the aggregates more compact (Fig. 1.2D). In summary, these four properties make BC unique and distinguished from BrC and other aerosols. It is noteworthy that the microphysical properties of BC and BrC are not constant throughout their lifetime but will change during atmospheric evolution or so-called “aging process”. Aging mainly affects the chemical properties of BrC via photochemical reactions or heterogeneous reactions, which will be discussed further in Section 1.2.4. Here we focus on how aging affects BC particles.

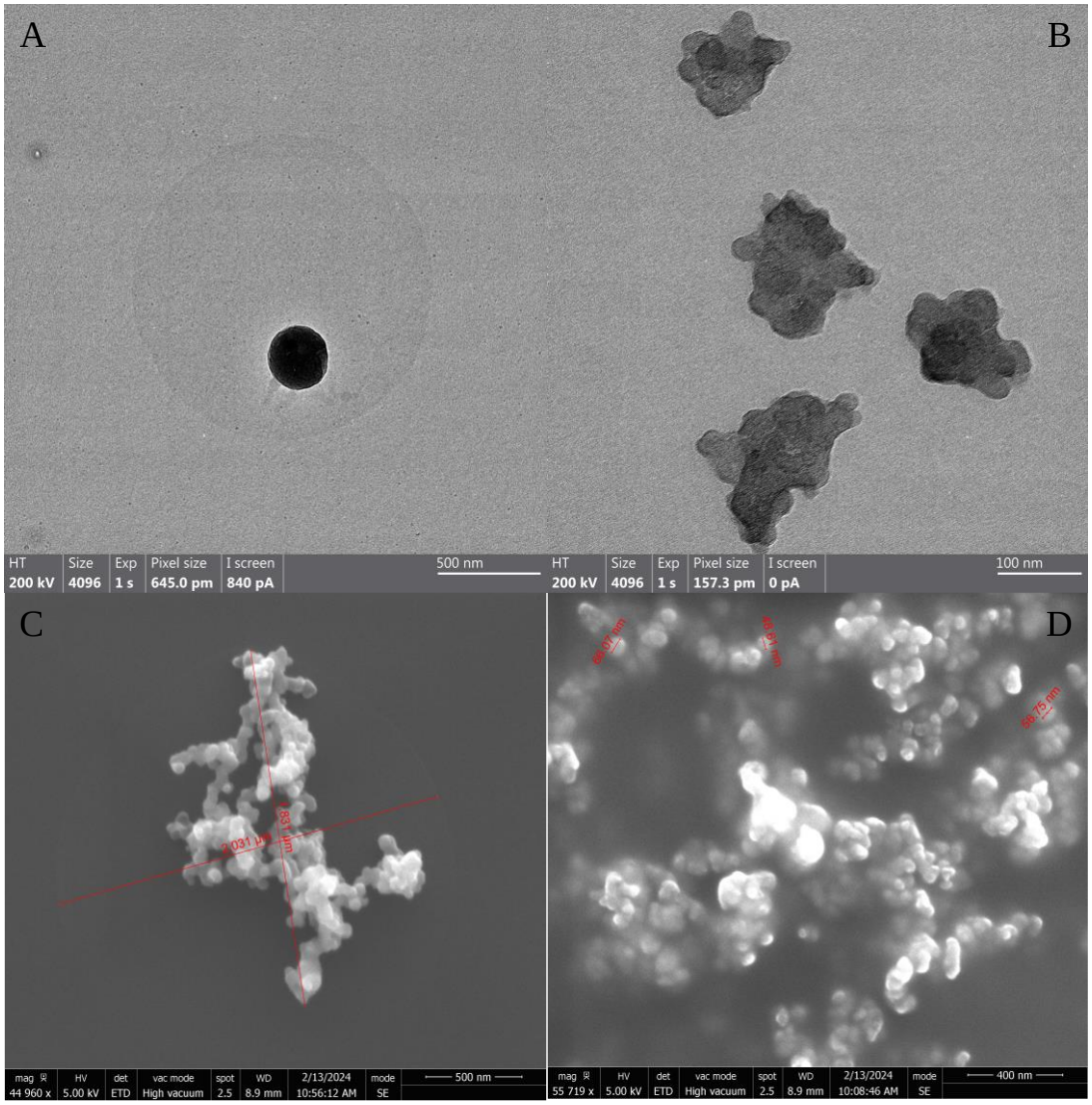

Figure 1.2. TEM and SEM (scanning electron microscopy) images of (A) BrC (tar ball) and (B, C, D) BC particles with diverse morphology.

Freshly emitted BC particles are usually hydrophobic and externally mixed with other pollutants such as organic matters and metals. Aging will not only change the size and morphology of BC particles from chain-like aggregates to larger and more compact aggregates, but also alter their mixing state. The term “mixing state” is used to describe how aerosols are mixed with other aerosols, like internal mixing, external mixing, homogeneous mixing, or heterogeneous mixing. For BC, external mixing with hydrophilic aerosols such as sulfate, nitrate, and water-soluble OA will increase the hygroscopicity of BC particles, making it easier for water vapor to condense on

the surface of BC particles, therefore amplifying the likelihood of BC particles to serve as CCN and INPs (Bond et al. 2013; Liu et al., 2020; von Schneidemesser et al., 2015). Even when mixed with hydrophobic OA, aging can achieve the same goals via oxidizing these OA in the atmosphere. The mixing state will also affect the optical properties of BC, which will be discussed in the following section.

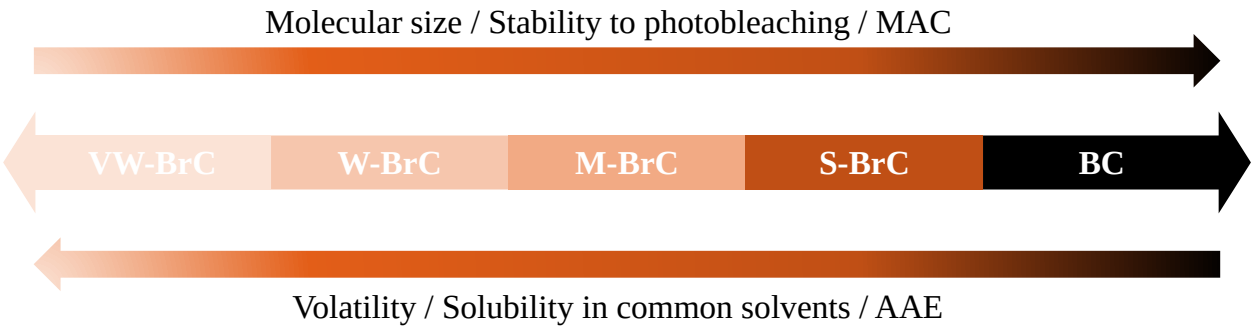

Figure 1.3. Graphic representation of BrC classification based on the absorptivity. Two one-direction arrows indicate the increasing trends of the properties. "VW-BrC" means very weakly absorptive BrC. "W-BrC" means weakly absorptive BrC. "M-BrC" stands for moderately absorptive BrC, and "S-BrC" indicates strongly absorptive BrC. "MAC" is mass absorption cross-section, "AAE" is absorption Ångström exponent.

1.2.3 Optical property of LACs

The optical properties of LACs are of great interest to researchers because these properties strongly affect the climate impacts of LACs. The absorption property of LACs is usually described by a power law (Equation 1):

$$B_{abs}(\lambda) = K \cdot \lambda^{-AAE} \quad (1)$$

where B_{abs} (λ) is the absorption coefficient with the unit of Mm^{-1} (or 1/Mm, where M = 10^6) at the wavelength of λ (nm), and K is a constant related to light absorption. When it comes to

measurement in ambient air, MAC (λ) can be acquired through Equation 2 if the mass concentration of LACs is known (C_{mass}):

$$MAC(\lambda) = \frac{B_{abs}(\lambda)}{C_{mass}} \quad (2)$$

where MAC (λ) is with the unit of m^2/g, and C_{mass} with the unit of g/m^3. MAC (λ) can be used to describe the light absorption ability of LACs at specific wavelengths. For BC, this value at 550 nm is measured as 7.5 m^2/g (Bond et al., 2006), whereas for BrC, this value can vary from larger than 1 (S-BrC) to as low as 10^{-3} m^2/g (VW-BrC) at 550 nm (Saleh, 2020). Thus, Equation 1 can be re-written in the format of MAC, which is used by some researchers:

$$MAC(\lambda) = K' \cdot \lambda^{-AAE} \quad (3)$$

where K' equals to K/C_{mass}.

Both Equation 1 and 3 show the wavelength dependence of light absorption of LACs, and AAE indicates how strong the dependence is. For BC, AAE is considered as 1. Therefore, BC demonstrates less dependence on wavelength, strongly absorbing from UV to near infrared. Yet for BrC, AAE ranges from 2 to as large as 8, indicating that the absorption of BrC drastically decays when λ increases. Furthermore, since K or K' is independent of wavelength, AAE can be determined via Equation 4, so long as B_{abs} or MAC at two different wavelengths (λ_1 and λ_2) are measured:

$$AAE\ (\lambda_1/\lambda_2) = \frac{ln\,[B_{abs}(\lambda_1)/B_{abs}(\lambda_2)]}{ln\,(\lambda_2/\lambda_1)} = \frac{ln[MAC(\lambda_1)/MAC(\lambda_2)]}{ln\,(\lambda_2/\lambda_1)} \quad (4)$$

LACs can not only absorb solar radiation, but also scatter it like other aerosols. The combined effect of absorption and scattering is called extinction, described by extinction coefficient (B_{ext}) (Equation 5):

$$B_{ext}(\lambda) = B_{abs}(\lambda) + B_{scat}(\lambda) \quad (5)$$

where B_{scat} stands for scattering coefficient. The single scattering albedo (SSA) can thus be as the ratio of B_{scat} to B_{ext} ($SSA = B_{scat}/B_{ext}$). If the value of SSA of an aerosol is equal to 1, this aerosol will only scatter light. However, when the value is lower than 0.8, it means the aerosol may lead to a net warming effect.

The above equations and parameters describe the common features of LACs' optical properties. However, BC and BrC have their own unique characteristics when conducting measurement and research in real life.

Absorption enhancement of BC particles ("lensing effect"). As mentioned, BC particles will undergo aging in the atmosphere once emitted, which brings two direct impacts: 1) most measurements based on light absorption are measuring BC-containing particles, instead of bare BC particles; 2) organic carbon (OC), whether transparent OC or light-absorbing OC (i.e., BrC), mixed with BC particles will lead to absorption enhancement of BC. The enhancement can be calculated by $E_{abs} = MAC_{obs}/MAC_{BC}$. MAC_{obs} describes the observed MAC of BC-containing particles, and MAC_{BC} refers to the reference value of bare BC particles. Only thickly-coated BC particles present strong absorption enhancement. Either thinly-coated or overly-coated BC particles exhibit little or no absorption enhancement (Lee et al., 2022). However, current models assume constant MAC_{BC} and enhancement for all coating situations, which can lead to overestimation of BC direct radiative effect (Liu et al., 2020).

Light absorption measurement of BrC in real life. Hecobian et al., (2010) introduced a protocol for processing BrC aerosol samples which has been widely used. BrC samples are collected by depositing them on filters with a high-flowrate impactor. Then the filter will be immersed in water and sonicated for a few hours to extract water-soluble OC (WSOC), followed

by filtration to remove insoluble contents, and concentration if necessary. Thus, it is the water solution of BrC that will be measured. To distinguish from MAC(λ) which is used to describe particles, mass absorption efficiency (MAE(λ)) is used to indicate light absorption of BrC solution. According to Beer-Lambert law, the light attenuation can be calculated based on Equation 6:

$$\frac{I_0}{I} = e^{B_{ext}(\lambda)l} \tag{6}$$

where l is the optical path length, and the logarithm format of I_0/I ($\log(I_0/I)$) can be replaced by absorbance A which can be measured by a UV/vis spectrometer. Since the contribution of light scattering and reflection can be reduced by using a reference solution, $B_{ext}(\lambda)$ can be considered as $B_{abs}(\lambda)$. $B_{abs}(\lambda)$ and MAE(λ) can be acquired by Equation 7 and 8:

$$B_{abs}(\lambda) = (A_\lambda - A_{700}) \times \frac{V_{liq}}{V_{air} \times l} \times \ln 10 \tag{7}$$

$$MAE(\lambda) = \frac{B_{abs}(\lambda)}{C_{WSOC}} \tag{8}$$

where A_λ is the absorbance at λ, V_{liq} is the volume of the solution, V_{air} is the volume of air passing through the filter, C_{WSOC} is the mass concentration of WSOC. The average absorbance between 695 to 705 nm (A_{700}) is utilized as a reference to minimize the impact of baseline drift, and BrC is assumed to have no contribution of light absorption within this wavelength range. The ratio of V_{liq} to V_{air} is to convert the light absorption of BrC in solution into the light absorption in ambient air. C_{WSOC} can be acquired from a total organic carbon (TOC) analyzer and is used as an estimation of BrC mass concentration. In addition, the imaginary part (k) of particle complex refractive index ($m = n + ki$), which is responsible for light absorption can be determined once MAE is known:

$$k_\lambda = \frac{MAE(\lambda) \times \lambda \times \rho}{4\pi} \tag{9}$$

where ρ (the density of BrC) is estimated as $\rho = (12+H/C+16 \times O/C) / (7 + 5 \times H/C + 4.15 \times O/C)$ (Kuwata et al., 2012).

As is shown above, because of the complexity of BrC constitutions, it is temporarily impossible to directly measure light absorption of BrC aerosols. Thus, water extraction of aerosol samples is used instead. However, this prevalent method brings some uncertainties. For example, the optical properties of BrC particles probably differ from that of BrC solutions since dissolving BrC in water may alter the morphology of BrC. Furthermore, not all BrC components are soluble in water, like tar balls mentioned above, which could cause underestimation of BrC mass concentration. On the other hand, not all WSOC species can absorb light. The usage of C_{WOSC} could lead to overestimation of BrC mass concentration. Consequently, the method described above is a compromise under the circumstance that light absorption measurement of BrC aerosols at a single-particle level is currently not available, which no doubt will contribute to the high uncertainty when modeling BrC direct radiative effect in the end.

1.2.4 Reactions of LACs in the atmosphere

BC is mainly composed of elemental carbon (EC), similar to graphite, which makes it chemically inert and stable on geologic time scales. Thus, during aging processes, the main component of BC particles (i.e., EC) will not be changed. It is those components mixed with BC particles that will evolve in the atmosphere, such as sulfate, nitrate, and OC (including BrC). However, BC can take part in atmospheric reactions as catalyst to facilitate the formation of other aerosols. For instance, Zhang F. et al. (2020) reported that BC can efficiently catalyze the oxidation of SO_2, even at low SO_2 level, with the presence of NO_2 and NH_3.

Unlike BC, BrC is chemically active in the atmosphere. Some transparent OA will become colorful through aging processes, serving as secondary sources of BrC. While some BrC species may suffer photobleaching, becoming transparent in the end. The formation of secondary BrC and photobleaching can take place simultaneously during daytime. For example, the light absorption of combustion-generated BrC mixtures tends to increase once BrC is emitted from the source, followed by the decay of absorption, indicating the competition between absorption enhancement and photobleaching (Saleh, 2020). Furthermore, depending on different phases, the formation and degradation of BrC has diverse pathways.

Gas-phase reactions of BrC. Nitroaromatic compounds have been considered as an important source of secondary BrC because higher MAC values of both laboratory research and field campaigns on SOA are always attributed to the formation of nitroaromatic compounds (Hems et al., 2021). For example, catechol is a highly reactive VOC emitted from biomass burning. The reaction between catechol and OH or NO_3 radical can lead to the formation of 4-nitrocatechol which is moderately absorptive (Fig. 1.4). PAHs like pyrene can also react with NO_3 radical to generate nitro-PAHs through gas-phase reactions. More importantly, the formation of nitroaromatic compounds from BrC precursors correlates to the relative concentration of NO_x, whereby higher concentration of NO_x can facilitate the formation of nitroaromatic compounds, and the MAC values tend to be highest when nitroaromatic compounds are formed. Yet SOA formed from biogenic precursors, such as isoprene and monoterpene, exhibit less absorption and weaker dependence on the NO_x concentration than nitroaromatic compounds.

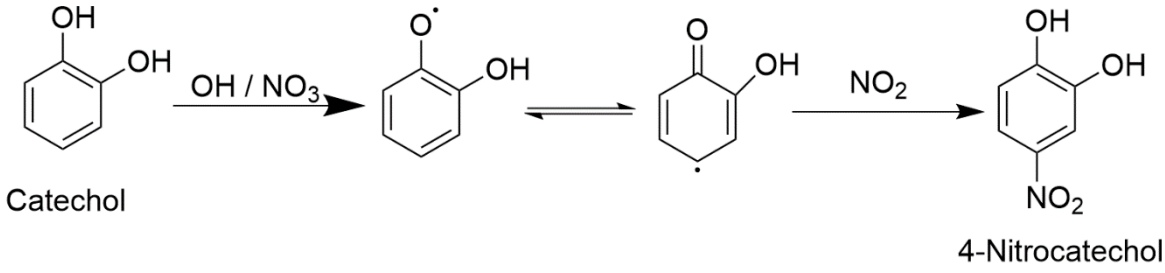

Figure 1.4. The reaction mechanism for the formation of 4-nitrocatechol, proposed by Finewax et al., 2018.

Aqueous reactions of BrC. Liquid water, such as cloud and fog droplets, suspended in the atmosphere, is an important medium where various aqueous reactions can take place, leading to the formation of secondary BrC. Nitroaromatic compounds can be formed not only via gas-phase reactions, but also through aqueous reactions. For example, 3-methylcatechol can react with nitrite in aqueous solution to form 3-methyl-4-nitrocatechol and 3-methyl-5-nitrocatechol with sunlight and without the presence of light, revealing a pathway of BrC formation during nighttime (Vidović et al., 2020). The photooxidation of Vanillin with nitrite in aqueous phase has been reported to be a significant source of atmospheric nitrophenols such as 4-nitroguaiacol and 5-nitrovanillin (Pang et al., 2019). These nitroaromatic compounds demonstrate stronger light absorption at visible wavelengths than their precursors. Besides nitration, it is possible for phenols to form dimers or oligomers through radical coupling reactions, which could contribute more absorption at longer wavelengths due to the extended π-conjugation. The formation of oligomers can also occur with iron as catalyst (Al-Abadleh, 2021), even if light is absent, which could be a source of secondary BrC during nighttime. Apart from nitroaromatic compounds, BrC can also be formed through reactions of α-dicarbonyls with reduced nitrogen compounds such as NH_3, NH_4^+ and amines. For example, glyoxal and methylglyoxal are water-soluble VOCs. They can react with ammonium sulfate or amines to form imidazole-based BrC compounds (Fig.1.5). This type of reactions in

laboratory research usually needs high concentrations and long reaction time. However, the evaporation of cloud and fog droplets can drastically accelerate the formation of BrC in the atmosphere (Hems et al., 2021; Laskin et al., 2015; Moise et al., 2015).

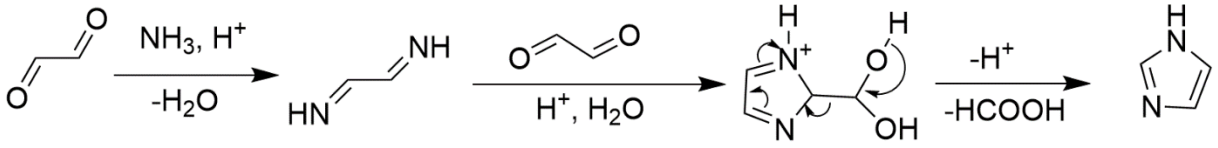

Figure 1.5. Reaction pathways for imidazole formation in the glyoxal and ammonium sulfate system, proposed by Yu et al. (2011). Here shows an example of formation of imidazole.

While many laboratory studies on aqueous reactions of BrC are conducted in bulk solutions, there is also some research on mimicking the reactions in cloud and fog droplets. Cloud and fog droplets suspended in the atmosphere may undergo evaporation which could drastically decrease the volume of water, leading to sharp increment of the concentrations of reactants, accelerating the reactions of forming secondary BrC (De Haan et al., 2017; Hawkins et al., 2018; Stangl and Johnston, 2017). But it is noteworthy that the evaporation of water droplets does not necessarily lead to higher concentrations of solutes. Some solutes such as glycolaldehyde may evaporate before reactions take place (Stangl and Johnston, 2017). In addition, the evaporation of water droplets could also achieve low pH, facilitating acid-catalyzed aldol condensation reaction and organosulfate formation (Fleming et al., 2019).

Reactions of Particulate BrC. Like BC, BrC and its precursors can undergo internal or external mixing with other aerosols once emitted, forming submicron particles. Under such circumstances, reactions between BrC and O_3, OH and NO_3 radicals, or other compounds such as NH_3 and SO_2, usually take place on the surface of the particle. These heterogeneous reactions are constrained by not only reactants but also the viscosity of the particle, whereby the viscosity of a

particle is dependent on relative humidity (RH). For example, Wang Y., et al. (2018) reported BrC formation from the reaction between toluene-derived SOA and NH_3 was slower when RH was less than 30%, whereas BrC generated from the reaction between isoprene-derived SOA and NH_3 was not affected by decreasing RH.

Furthermore, heterogenous NO_3 oxidation is an essential pathway of BrC formation during nighttime, such as nitration of PAHs mentioned above. And BrC light absorption can be enhanced after a few hours of nighttime aging, which is attributed to the formation of secondary chromophores. However, due to this enhancement, BrC would be bleach faster during the daytime by photolysis (Li C., et al., 2020). These results are based on laboratory studies. Direct observation of nighttime aging of biomass burning is still scarce and needed to elucidate the effects of NO_3 nighttime aging.

Degradation of BrC. The active chemical properties make BrC susceptible to photochemistry and oxidation. The formation of new BrC and the degradation of BrC are always competing after BrC and its precursors are emitted, which is demonstrated as absorption enhancement followed by photobleaching. The processes leading to loss of BrC absorption can be summarized as three pathways: photolysis, O_3 oxidation, and OH oxidation. Photolysis usually takes place with the absence of oxidants, and it is the dominant photobleaching mechanism for molecules larger than 400 Da (Saleh, 2020). It can either cause fragmentation of functionalized BrC molecules (Henry and Donahue, 2012) or excite a molecule to its triplet state and then energy transfer to a less absorptive species (Feilberg and Nielsen, 2001).

O_3 is ubiquitous in the atmosphere, and it could react with unsaturated function groups. Compared with photolysis, O_3 oxidation does not necessarily need light, which makes it possible for O_3 to oxidize BrC during both daytime and nighttime. For example, Sareen et al. (2013)

reported SOA formation by the reaction between $(NH_4)_2SO_4$ and methylglyoxal at dark condition followed by photolysis. They found O_3 dark oxidation broke unsaturated carbon-carbon bonds to form carbonyls, which led to the loss of absorption at short wavelengths but an increase in absorption at visible wavelengths. O_3 oxidation also caused fragmentation of SOA, forming small molecules such as formic acid and acetic acid. The importance of O_3 oxidation is probably higher when wildfires happen. Wildfires can increase regional O_3 concentration because of photochemical reactions of VOCs or NO_x emitted from wildfires. Browne et al., (2019) found that O_3 oxidation on primary BrC generated by biomass burning led to weaker light absorption at 405 and 532 nm when increasing the concentration of O_3. But A fraction of BrC components were resistant to O_3 oxidation, which was attributed to the increasing viscosity of the particles which limited the diffusion of reactants from the bulk of the particles to the surface. Thus, more field measurements and laboratory studies are needed to evaluate the effects of O_3 oxidation.

Apart from directly serving as oxidant, O_3 is also used as a source of OH radicals in laboratory studies on OH oxidation with the presence of light. OH oxidation, in contrast to photolysis, is the dominant mechanism for bleaching molecules smaller than 400 Da (Saleh, 2020). It can take place in gas phase, aqueous phase, and on the surface of particles. OH oxidation of BrC has been widely investigated in laboratory studies (). For instance, Sumlin et al. (2017) conducted controlled biomass burning experiments with OH exposure at different concentrations, finding that primary BrC particles underwent functionalization but accompanied by a sharp decrease in light absorption at 375 nm. Hems et al. (2020) found that OH oxidation of BrC in aqueous reactions led to a decrease at short wavelengths but an increase at 400 nm, indicating the fragmentation of unsaturated carbon-carbon bonds and the formation of new chromophores took place simultaneously in cloud. The research by Sareen et al. (2013) mentioned above also demonstrated

fragmentation caused by OH oxidation, but the change of light absorption was not reported. Although OH oxidation is usually considered to occur with the presence of light, it has been recently reported that photoinitiated OH oxidation can persist in the dark environment (Liu-Kang et al., 2022), indicating that OH oxidation may also play a role in degrading BrC during nighttime.

1.2.5 Current measurement techniques of LACs

1.2.5.1 Measurement of optical properties

Since optical properties of LACs are of great interest, most measurement techniques are based on the absorption of LACs. Table 1.1 summarizes some common commercial instruments for LACs, mostly for BC because it is still difficult to measure BrC directly. The BC/BrC measurement methods can generally be divided into two groups: in-situ instruments and filter-based instruments. They share the same underlying assumption that only BC can absorb laser radiation at wavelengths longer than 800 nm.

Table 1.1. Common Commercial instruments used for measuring the optical properties of LACs.

Instrument	Principle	Parameter measured	Bias sources
Photoacoustic Extincometer (PAX)	Photoacoustic in-situ optical absorption	B_{abs} B_{scat}	Could be affected by S-BrC like tar balls
Single Particle Soot Photometer (SP2)	Laser-induced incandescence	Size distribution BC mass concentration BC number concentration B_{abs} B_{scat}	Missing information of BC particles smaller than 60 nm
EC/OC Analyzer	Thermal optical reflectance and transmittance by collection on filters	EC mass concentration OC mass concentration Total carbon concentration	Attributing less volatile OC to EC
Aethalometer	Optical absorption by collection on filters	B_{abs} BC mass concentration AAE	Same as PAX, plus: aerosol scattering

			and filter loading effect
UV/vis spectroscopy	Optical absorption by extraction in solvents	Absorbance of soluble BrC	Only soluble BrC can be measured

In-situ instruments measure LACs as if they are aerosols. The measurement will not change the size and morphology of aerosol particles. In this way, the parameters acquired can be considered to represent the real situations in the atmosphere. Photoacoustic-based instruments such as PAX, photoacoustic soot spectrometer (PASS), and photoacoustic spectrometer (PAS), measure the change of air pressure caused by the heat transferred from LACs which heat up by absorbing laser radiation. Because of the accuracy and in-situ measurement, photoacoustic-based instruments are often used to calibrate filter-based instruments (Bond et al., 2013). PAX and PASS also have short-wavelength modules which can be used to measure and separate the absorption of BrC aerosols by Equation 4 introduced in Section 1.2.3. However, short-wavelength PAX or PASS cannot distinguish BrC from other absorbers such as mineral dust.

SP2 is another in-situ instrument but is based on laser-induced incandescence. Briefly, a 1064 nm laser is utilized to heat BC to the point of incandescence. The instrument measures the light emitted by heated BC particles to determine the mass, regardless of particle mixing state. And the scattering signals can be used to calculate the number and mass concentration of non-BC scattering aerosols. More importantly, SP2 can achieve single particle level detection, thus SP2 can provide BC size distribution and number concentration as well. Although SP2 is a powerful tool and can provide abundant information about BC, it is unable to detect BC particles with a diameter smaller than 60 nm which may account for a large proportion of BC number concentration.

Filter-based instruments measure the change of light transmission caused by collecting LACs on filters. Seven-wavelength aethalometers such as AE33 and AE43 are widely used for long observation because of their stability and simple operation protocol. Aethalometers use seven wavelengths which span from 370 nm to 950 nm, and light absorption of BrC at short wavelengths can be separated from total absorption. Therefore, aethalometers are used to estimate the contribution of BrC by combing Equation 4 and $B_{abs,\ total} = B_{abs,\ BC} + B_{abs,\ BrC}$ (Bai et al., 2023; Q Wang et al., 2019). There are other commercial instruments working in a similar way as aethalometer, such as particle soot absorption photometer (PSAP) and multi-angle absorption photometer (MAAP). These filter-based absorption instruments are suffering the same problem: aerosol scattering effect and filter loading effect, which may lead to overestimation of BC mass concentration. Although AE43 incorporates the "DualSpot" measurement method to eliminate the filter loading effect (Drinovec et al., 2015), the aerosol scattering effect remains a source of uncertainty.

EC/OC analyzer is also a filter-based instrument but mainly based on thermal-optical method. Basically, the samples collected on the filters will be heated in programmed temperature steps so that volatile OC can be separated from EC. Both OC and EC will then be combusted to generate CO_2. Thus, the concentration of OC and EC can be determined respectively. But EC/OC analyzer may attribute low volatile OC to EC, leading to overestimation of EC. In addition, some OC may undergo pyrolysis when heating up, which could again cause overestimation of EC (Zhang Z. et al., 2023c).

UV/vis spectroscopy is different from the measurements mentioned above. Aerosol samples need to be collected on filters first and extracted in solvents, as described in Section 1.2.3. Therefore, only soluble BrC components can be measured, which excludes BC and insoluble BrC.

Using soluble BrC as proxy of BrC will lead to underestimation of BrC mass concentration and absorbance. Furthermore, this measurement is conducted in bulk solutions where size and morphology of BrC may be altered, contributing another source of measurement bias. Thus, this method can only provide an estimation of BrC concentration.

1.2.5.2 Measurement of chemical properties

Due to the chemical and functional complexity of BrC, it is impossible to identify every species of BrC and predict light absorption from molecular levels. However, efforts have been made to characterize BrC components with mass spectroscopy (MS) in the past decades. High performance liquid chromatography-mass spectrometry (HPLC-MS) is one of the most popular techniques (Laskin et al., 2015), because water is widely used to extract BrC, especially to extract HULIS which is known to be water soluble. To acquire molecular ion peaks in HPLC-MS, soft ionization techniques such as electrospray ionization (ESI) are usually coupled with HPLC-MS. In addition, some BrC components such as imidazole are polar, which also makes ESI suitable for them, while less polar molecules like nitro-PAHs, atmospheric pressure chemical ionization (APCI) could be a readily available alternative. Besides HPLC-MS, gas chromatography-mass spectrometry (GC-MS) is also utilized by some researchers (Kuang et al., 2023; Soleimanian et al., 2020; Wu C. et al., 2023). GC-MS is very suitable for volatile and semi-volatile BrC components such as PAHs and nitro-PAHs due to its high sensitivity and resolution. The choice of HPLC-MS or GC-MS depends on what types of molecules are of interest. But as discussed in section 1.2.2, the absorption of BrC gets stronger with volatility decreasing, which makes HPLC-MS preferable.

Both HPLC-MS and GC-MS are traditional MS for offline analysis, which means aerosol samples must be collected and processed for analysis. To achieve real-time continuous

measurement, aerosol mass spectrometry (AMS) has been developed and extensively used. In addition to in-situ measurement, AMS can measure chemical composition of BrC at single particle level, and it can detect BC if coupled with the soot particle module (Shu et al., 2023).

Apart from MS, TEM and SEM coupled with energy-dispersive X-ray spectroscopy (EDS) can be applied to characterize size, morphology, and chemical constitutions of BC and some BrC particles. As mentioned above, most BrC species are unstable under high vacuum environment and high energy electron beam, which limits the application of electron microscopy on BrC detection.

1.3 Effects of LACs on Health and Climate

1.3.1 LACs as Air Pollutants in Cold-climate Urban Regions

Anthropogenic emission is the dominant source of LACs in urban regions, whereby industrial production, domestic fuel combustion, and transportation are major sources of LACs and $PM_{2.5}$. Continuous measurement of BC and BrC specifically at urban air quality monitoring stations is not prevalent yet. Instead, BC and BrC are considered subsets of $PM_{2.5}$. Therefore, most studies on health impacts are focused on $PM_{2.5}$ as ensemble. But there are increasing number of studies on health concern of BC recently. For example, Zhang et al. (2023) reported that long-term exposure to BC could lead to chronic kidney disease. Rasking et al. (2023) pointed out that BC reached the kidney through inhalation and circulation in the body. Liu et al. (2023) detected BC in eye-washing fluid, indicating the ocular exposure risk. Additionally, long-term exposure to BC could also cause obesity (Yang et al., 2023), cardiovascular diseases (Wen et al. 2023) and large-artery atherosclerotic stroke (Vivanco-Hidalgo et al., 2018). As for BrC, PAHs and its derivatives, and nitroaromatic compounds such as nitrophenols, have been widely investigated and identified

as carcinogens and damaging organs (Kitanovski et al., 2021; Samburova et al., 2016). The WHO has proposed to make systematic long-term measurements of BC as a complement to current routine $PM_{2.5}$ measurements in the new guideline for air quality (WHO 2021a). However, it is difficult to continuously monitor BrC emissions due to instrumentation. Although AMS has been utilized by researchers in universities and research institutions, the high cost makes it hardly accessible for governments. Developing a stable and low-cost commercial instrument for BrC is still challenging but necessary.

Furthermore, BC can lead to a "dome effect", suppressing the development of the planetary boundary layer (PBL) (Ding et al., 2016). The development of PBL during daytime is due to rising temperature and can decrease the concentration of air pollutants. BC that is transported beyond the PBL can absorb solar radiation, heating up surrounding air which inhibits the height of PBL. The "dome effect" of BC has been proved to be associated with haze formation during winter (Li Z. et al., 2017; Zhang Y. et al., 2023b). This effect could even worsen the situation of air pollution during winter in cold-climate cities. Compared with warm-climate regions, winter spans longer in cold-climate cities. For example, Canada is known to be a cold-climate country. According to Environment and Climate Change Canada (ECCC), winter in Canada usually starts on December 1st, and lasts until April 20th. But the actual meteorological winter could even start earlier and end later. The long winter also brings extra sources of LACs such as wood or oil burning for heating. The concentration of BC and other air pollutants can maintain high values during the long winter months. Meanwhile the "dome effect" caused by BC can further deteriorate air quality in urban areas, demonstrating the necessity of measuring and regulating the emission of BC (and BrC).

1.3.2 Climate Effects of LACs

Direct effects. As mentioned in section 1.1, atmospheric aerosols can affect the climate directly and indirectly. LACs, as a unique group of aerosols, are of great importance and interest for scientists because they can absorb solar radiation directly, warming the atmosphere. However, numerous studies have suggested various direct radiative forcing values of LACs, demonstrating the large uncertainty of evaluating the direct impacts of LACs. For instance, Bond et al. (2013) reported that global mean direct radiative forcing of BC is +0.88 W/m^2 with an uncertainty of +0.17 to +1.48 W/m^2, while the IPCC suggested effective radiative forcing of BC to be +0.11 W/m^2 with an uncertainty of -0.20 to +0.42 W/m^2 in the AR6 report (IPCC 2021). Other researchers also reported different values such as +0.23 (+0.06 to +0.48) W/m^2 (Myhre et al., 2013) and +0.15 ± 0.17 W/m^2 (Thornhill et al., 2021). The physicochemical properties of BC discussed in section 1.2 such as size, morphology, mixing state, and MAC, as well as factors like lifetime and emission amount, all contribute to the high uncertainty when estimating direct radiative forcing of BC. As for BrC, to quantify its radiative forcing is even harder because of the complex composition of BrC components. Some efforts have been made to estimate the direct radiative forcing of BrC which ranges from +0.03 to +0.6 W/m^2 (Feng et al., 2013; Jo et al., 2016; Saleh et al., 2015) although these simulation works are inevitably suffering the problem of oversimplification.

In addition to absorbing radiation in the atmosphere, LACs deposited in the cryosphere could also exert positive radiative forcing, warming the climate. Snow and ice in cryosphere such as Arctic and Tibetan Plateau play essential roles in reflecting the solar radiation to cool the climate. Although there are very limited local emission sources of LACs in the cryosphere, anthropogenic LACs can undergo LRAT to reach these remote regions. Fossil fuel combustion in winter and

biomass burning in summer are the major sources of LACs deposited in the cryosphere (Liu et al., 2020). LACs deposited on snow/ice can accelerate the melting by darkening the surface of snow/ice. As snow/ice ages, radiative forcing induced by LACs can boost from a few watts per square meter in fresh snow to hundreds of watts per square meter in aged snow, which strongly contributes to the acceleration of glacier melt (DeMott et al., 2010).

Indirect effects. LACs can serve as CCN and INPs as other aerosols to affect the climate indirectly by forming cloud and ice. Pure BC particles are not good CCN because they are insoluble and hydrophobic. But while BC particles age in the atmosphere, they can mix with other aerosols internally or externally, which allows them to become more hygroscopic and activated as CCN. While for BrC, it depends on specific components. Those hydrophobic BrC components may experience oxidation to become hydrophilic which allows for activation as CCN (Liu et al., 2020).

Besides forming clouds, the ice nucleation of LACs is also under debate due to their complexity. The heterogeneous ice nucleation of BC has been widely investigated in the past decades, and results from different studies often contradict each other. For example, researchers reported contradictory results during two field campaigns on mixed-phase clouds at the same observation site, indicating BC particles are either efficient INPs or unimportant for ice nucleation in mix-phase clouds (Cozic et al., 2008; Kamphus et al., 2010; Kupiszewski et al., 2016). While for laboratory experiments, the ice nucleation temperature of BC ranges from 213 to 258 K, demonstrating a large discrepancy (DeMott et al., 1999; Ikhenazene et al., 2019; Mahrt et al., 2020). One reason for this discrepancy is that researchers conducted experiments with different materials under different conditions. The diversities of size, morphology, and mixing state could contribute a large uncertainty when comparing results from different articles. As for the ice nucleation of BrC,

there are very limited studies. Knopf et al. (2018) summarized research on ice nucleation of various OC, which covered the components of BrC such as HULIS and PAHs. Chen et al. (2021) reported that HULIS entities were efficient ice nuclei under mixed-phase cloud conditions, which could demonstrate the potential of BrC particles in ice nucleation. There is no doubt that the complexity of BrC composition strongly inhibits research on BrC particles as INPs, and thus the estimation of the indirect climate effect of BrC.

1.3.3 Looming Threat Due to Increasing Occurrence of Wildfires

The occurrence of wildfires has been investigated in the past few years. Wildfires are thought to be more frequent and more severe due to climate change (Eck et al., 2023; Morawska et al., 2021; R Xu et al., 2023). As mentioned before, wildfires are important sources of LACs, which can emit a large number of LACs and their precursors. Wildfires which take place in high-latitude regions such as northern Canada and Alaska would make it easier for LACs to deposit in cryosphere via LRAT, darkening the surface of snow/ice, accelerating the melting of glaciers due to the reduced snow albedo, further exacerbating global warming. Apart from climate effects, the increasing number of wildfires will also strongly deteriorate air quality in urban regions even a few hundred kilometers away through LRAT, which poses serious threats to human health. The challenges caused by surging wildfires would require governments to pay more attention to control the occurrence and spreading of intense wildfires in large areas.

1.4 Machine Learning in Environmental Pollution Research

With the rapid advancement of modern science and technology, the quantity and the complexity of research data has been widely extended. Traditional data analytical tools may be insufficient to discover the potential relationships behind research data, calling for new powerful approaches to unveil the patterns or trends in data. As a result, machine learning (ML) is increasingly applied in environmental research.

ML is the science of programming computers so that they can learn from data (Géron 2019). ML models rely on specific algorithms to learn from training instances or samples to make predictions or decisions although they are not programmed to do so, coupled with a corresponding performance measure to evaluate the outcomes. A significant difference between ML models and other physical or chemical models is that ML models do not rely on physical processes or chemical reactions behind the data to make predictions or decisions. Instead, ML models learn directly from data and results to establish the relationship between them, which may be able to reveal the significance of factors or processes, and give insight into physical or chemical processes.

ML can be categorized into supervised learning, unsupervised learning, semisupervised learning, and reinforcement learning (Géron 2019). Supervised learning is the most prevalent ML used for training models (Zhu et al., 2023). In supervised learning, data are fed to the algorithm and are associated with true values, so that the performance of the model can be evaluated by comparing outcomes with true values. One typical task of supervised learning is regression (predicting values). This type of task is to predict target values (outcomes) by giving a set of features (variables, or inputs). Linear regression like $y = ax + b$ is the simplest format of regression jobs. In environmental science, regression usually involve multiple features (x_1, x_2, x_3, ...), and the relationship between y and x may be something other than linear, such as polynomial. Another

supervised learning task is classification (predicting classes). As indicated by the name, classification is about assigning the data into distinct groups. For example, showing a picture of an animal to a computer vision model to see if it can place the animal in the correct classification. Unsupervised learning works with data without labels. Therefore, unsupervised learning is used to discover the potential pattern of data, such as clustering data or reducing dimensions of data to simplify the calculation process. Whereas semisupervised learning deals with data partially labeled, and reinforcement learning is less relevant to environmental research.

Table 1.2. Examples of applying ML models in environmental studies.

Task	Algorithms	Inputs	Outputs	Ref
Identifying feature importance	Random forest (RF)	Mass concentrations from different sources	B_{abs} (355), MAE (355), B_{abs} (365), MAE (365)	Hong et al., 2022
Identifying feature importance	RF, Aggregated boosted tree	Concentrations of 13 chemical species, 4 trace gases, and 4 meteorological variables	The importance and relative influence of input parameters	Jiang et al., 2021
Prediction	RF	8 fractions of PM2.5, 7 gaseous species, and 4 meteorological variables	Number concentration of CCN	Nair and Yu, 2020
Prediction	RF	5 time variables, 4 meteorological variables, 6 geographical variables, and 12 HYSPLIT trajectories	Mass concentrations of OC, sulfate, nitrate, ammonium, chloride, and BC	Zhou et al., 2022
Prediction	Support vector regression (SVR)	Distance to traffic routes, distance to coasts, percentage of land use, population, 6 meteorological variables	BC mass concentration	Abu Awad et al., 2017

Prediction & Classification	RF, XGBoost, CatBoost	PM2.5, PM10, CO, NO2, SO2, and O3, 8 meteorological variables	Concentrations of PM2.5 and O3,	Wang S. et al., 2023
Discovering new materials	RF	Polymer property data from literature and experiments, polymer features based on composition, configuration, topology, and polarity	Target properties from candidate polymers	Pilania et al., 2019

Table 1.2 listed some examples of the application of ML models in environmental studies. In the past decades, publications concerning ML methods have been exponentially increasing (Liu et al., 2022; Zhong et al., 2021), revealing the great potential of introducing ML methods to traditional environmental research. Compared with traditional statistical methods, ML methods are good at dealing with large datasets, features, and various data formats, discovering their correlations and patterns, especially for nonlinear relationships which are difficult for statistical methods to detect. Furthermore, ML models can be roughly divided into linear models, such as linear regression, principal component analysis, and positive matrix factorization, and nonlinear models, such as models based on artificial neural network (ANN) like recurrent neural network (RNN) and long short-term memory (LSTM), and random forest (RF). Some models can handle both linear and nonlinear relationships, such as support vector machine (SVM) and extreme gradient boosting (XGBoost). There is no single model which can solve all kinds of problems. One model can work better than other models for one type of task but perform poorly for another type of task. The choice of models should be determined based on specific questions to be investigated.

Although ML demonstrates great potential to solve research problems, there are still some challenges which may lead to bad performance or inappropriate applications of ML models. First,

ML models rely on data for training. As such, the training dataset should be representative and big enough to demonstrate every aspect of the feature. Furthermore, the quality of the dataset should be high, with excellent coverage, precision, and accuracy. Obviously, the model trained by data filled with errors or outliers is impossible to perform well. After choosing good data, data preprocessing and splitting must be done before training. Real-world data are from diverse sources. Therefore, the range of data values sometimes spans a few orders. Data preprocessing like scaling data values into a smaller range (e.g., between 0 to 1) can facilitate the training process. Then the data should be split into a training set and a test set which are independent of each other so that data leakage can be avoided during the training. During the model training process, proper evaluation metrics shall be determined based on the type of task. For example, accuracy should be a good metric for classification tasks, while for prediction tasks, root mean square error (RMSE) and mean absolute error (MAE) are better metrics. Yet if the model achieves a perfect score on training set, it likely means the model has been "overfitted". Overfitting indicates that the model learns so good on the training set that it cannot generalize well because it is impossible for the training set to cover all the situations in the real world. New instances outside of the training set are very likely to fail an overfitted model. Overfitting is a widely recognized problem in ML, and it can be lessened by measures such as cross-validation. Of course, there are more problems which are not mentioned in the application of ML models. Zhu et al. (2023) contributed an excellent review on common pitfalls appearing in current research articles and provided a comprehensive guideline for application of ML models.

Apart from traditional problems mentioned above, model interpretability is an emerging problem as many ML systems are black boxes. Deep neural network models (or deep learning models) such as convolutional neural network (CNN) and RNN are especially suffering from the

problem of interpretability. For example, to predict concentrations of air pollutants is a complex task because of the physicochemical properties, the temporal and spatial distribution, and the diverse sources of air pollutants, and various atmospheric processes they undergo. Deep neural network models are quite suitable for this type of task, and they can achieve good results. However, it is difficult to understand what happens inside the model. Therefore, these models are regarded as “black box”. Simpler models such as RF, SVM, and XGBoost are easier to interpret, and thus they are preferred when complex deep learning models cannot outperform them (Liu et al., 2022).

1.5 Outstanding Questions

Despite the decades of research on emissions, optical properties, and chemical properties of LACs, and their lifecycle in the atmosphere, it is still difficult to clarify the climate effects and health impacts of LACs. Current satellite and remote sensing technologies are advanced, but they cannot sufficiently reflect emissions, physicochemical properties, and atmospheric processes of LACs. Thus, ground-based in-situ observations are essential and necessary to advance our knowledge of LACs and their effects in the real world and climate models. Therefore, this section summarizes the primary and long-term questions which this thesis works to explore:

1. How big can anthropogenic sources contribute to the emission of LACs in cold-climate urban regions? And how human activities would affect the emission of LACs?
2. The threat of wildfires is increasing. How would wildfires alter the physicochemical properties of LACs? What is the impact of wildfires on urban areas which are far away from the sources of wildfires?

3. The necessity of monitoring LACs emission is increasing, but the instruments are not prevalent. Is it feasible to develop a model to estimate the concentrations of LACs with other air pollutants?

1.6 Structure of the Thesis

This thesis is composed of three manuscripts each corresponding to a chapter of the thesis, except for Chapter 1 (Introduction) and Chapter 5 (Conclusion and Future Work).

Chapter 2 was published as "Li, H., and Ariya, P. A. (2021). Black carbon particles physicochemical real-time data set in a cold city: Trends of fall-winter BC accumulation and COVID-19. Journal of Geophysical Research: Atmospheres, 126, e2021JD035265." This manuscript focuses on one-year variation of concentrations of BC and other air pollutants, which covers the period of COVID-19 Pandemic. The lockdown due to COVID-19 provided an unexpected chance to directly observe the impacts of human activities and anthropogenic emissions of air pollutants in urban regions. This work presents Montreal BC mass concentration had a bi-modal distribution (summer and winter). Airport BC concentration was >400% higher than downtown. The concentrations of BC and co-pollutants decreased to 72% in the COVID-19 period, pointing to significant anthropogenic emissions of BC and other air pollutants.

Chapter 3 is a manuscript submitted to Atmospheric Chemistry and Physics as "Li, H., Pal, D., and Ariya, P. A. (2024). Seasonal Trend of Black Carbon and Brown Carbon in Montreal: Impacts of Canada Record-Breaking Wildfires in Summer 2023." This manuscript first demonstrates the variations of BC and BrC for one year, confirming the dominant impacts of anthropogenic sources in urban regions discovered in Chapter 2. But the record-breaking wildfires

during the summer of 2023 strongly affected Montreal. This manuscript focuses more on the impacts of wildfires, showing that BC mass concentration increased more than 26% due to the wildfires. Additionally, secondary BrC light absorption accounts for 20 to 30% of BrC light absorption, whereby BrC light absorption at 370 nm accounting for more than 50% of total light absorption, indicating the enormous potential of BrC emitted from wildfires.

Chapter 4 is in preparation for submission as "Li, H., and Ariya, P.A. (2024). Using Machine Learning Model to Derive BC Mass Concentration Based on Common Air Pollutants." This manuscript describes a data-driven ML model used to estimate BC mass concentration. The model was trained with common air pollutants such as CO, O_3, NO_x, and $PM_{2.5}$. The predicted BC mass concentrations were then compared with the measured ones to evaluate the performance of the ML model. This manuscript demonstrates a feasible and promising model for simulating BC mass concentration as a complement to current air pollution monitoring protocol.

Chapter 2 Black Carbon Particles Physicochemical real-time dataset in a Cold City: Trends of Fall-Winter BC Accumulation and COVID-19

The importance of LACs has been discussed in Chapter 1. However, there is very limited observation coming from cold-climate regions where winter seasons usually last longer than those warm-climate regions. Since BC can accelerate snow melt by darkening the snow surface, BC might be able to affect cold-climate regions more than warm-climate regions. Furthermore, anthropogenic emissions of BC in cold-climate urban regions shall be evaluated, which was achieved straightforward in this manuscript due to the COVID-19 Pandemic. Here we present a valuable dataset of BC and other air pollutants in a cold-climate city, revealing the profound impacts from anthropogenic emissions in urban areas.

Contribution of Authors

I conducted the sampling and the experiments, analyzed the data, interpreted the results, prepared the figures, and wrote the original manuscript. I am the first author of this original article.

Professor Parisa A. Ariya (supervisor) co-authored this paper and is the corresponding author. She provided continuous guidance and support, designed the studies, participated in interpreting results and discussions, provided insights into experiments, and edited the article.

This Chapter consists of the following published article in peer-reviewed journals:

Li, H., & Ariya, P. A. (2021). Black carbon particles physicochemical real-time data set in a cold city: Trends of fall-winter BC accumulation and COVID-19. *Journal of Geophysical Research: Atmospheres*, *126*, e2021JD035265. https://doi. org/10.1029/2021JD035265.

Black Carbon Particles Physicochemical real-time dataset in a Cold City: Trends of Fall-Winter BC Accumulation and COVID-19

Houjie Li[1], Parisa A. Ariya[1,2,*]

[1] Department of Chemistry, McGill University, Montreal, Quebec, CANADA

[2] Department of Atmospheric and Oceanic Sciences, McGill University, Montreal, Quebec, CANADA

*Corresponding author: Parisa A. Ariya (parisa.ariya@mcgill.ca)

Abstract

Black carbon (BC) plays an important role in climate and health sciences. Using the combination of a year real-time BC observation (photoacoustic extinctiometer) and data for $PM_{2.5}$ and selected co-pollutants, we herein show that annual BC mass concentration has a bi-modal distribution, in the cold-climate city of Montreal. In addition to the summer peak, a winter BC peak was observed (up to 0.433 μg/m^3), lasting over 3 months. A comparative study between two air pollution hotspots, downtown and Montreal international airport indicated that airborne average BC mass concentration in downtown was 0.344 μg/m^3, whereas in the residential areas around Montreal airport BC mass values were over 400% higher (1.487 μg/m^3). During the numerous snowfall events, airborne BC mass concentration decreased. HR-S/TEM-EDS analysis of the snow samples provided evidence that airborne black carbon particles or carbon nanomaterials were indeed transferred from polluted air to snow. During the COVID-19 lockdown, the BC concentration and selected co-pollutants, decreased up to 72%, confirming the predominance of

anthropogenic activities in BC emission. This first cold-climate BC dataset can be essential for more accurate air quality and climate modelling. As about the third of Earth's land surface receive snow annually, the impact of this study on air quality, health and climate change is discussed.

2.1 Introduction

Aerosols or airborne particles have drawn great scientific interests in the past decades due to their essential roles in the nucleation of ice, clouds, formation, type and intensity of precipitation, radiation budget and climate change (Bond et al., 2013; de Oliveira Alves et al., 2015; Fuzzi et al., 2015; IPCC, 2013; Knopf et al., 2018; McCluskey et al., 2014; Munoz-Alpizar et al., 2017; Murray et al., 2012; Nazarenko et al., 2017; Petters et al., 2009; Qian et al., 2014; Rangel-Alvarado et al., 2019; Washenfelder et al., 2015). The Intergovernmental Panel for the Climate Change (IPCC) has thereby identified aerosols and aerosol-climate interactions as the major uncertainty in climate change (IPCC, 2013). The World Health Organization (WHO) has shown that aerosols have critical impacts on human health, contributing to over 8 million premature deaths per year, including 4.2 million deaths attributed to ambient air pollution and 3.8 million deaths caused by indoor air pollution (WHO 2021b).

Aerosol composition is diverse, originating from natural and anthropogenic sources such as organic, inorganic (including metallic) and biological particles (Bond et al., 2013; Hall et al., 2020; IPCC, 2013; Rahim et al. 2019; Rangel-Alvarado et al. 2015; Rivas et al. 2020). Airborne black carbon (BC) is a type of aerosol that is formed as by-product of incomplete combustion of fossil fuel, accounting for 5% to 15% of the annual urban particulate matter concentration (Xu et al., 2020; Yang et al., 2011).

Like other aerosols, BC can impact climate directly by absorbing and scattering solar radiation (Bahadur et al., 2012; Bond & Bergstrom, 2007; Bond et al., 2013; Qian et al., 2014; Xu et al., 2019), and indirectly by serving as cloud condensation nuclei and ice nuclei (Brooks et al., 2014; Fan et al., 2016; Kulkarni et al., 2016; McCluskey et al., 2014; Parent et al., 2016; Qian et al., 2014; Vergara-Temprado et al., 2018). BC is a significant component in climate change (Bond et al., 2013) and is estimated to be +1.1 W/m^2 with 90% uncertainty bounds from +0.17 to +2.1 W/m^2, only second to CO_2 (Bond et al., 2013). Yet the question of how BC affects climate change is still debated (Dou & Xiao, 2016; Grandey et al., 2018; IPCC, 2014; Malavelle et al., 2019) due to lack of knowledge of the physicochemical properties of BC.

The lack of understanding of the BC's physicochemical characteristics such as morphology, size and mixing state is the cause of the existing large uncertainty for an accurate evaluation of its radiative forcing (Bond & Bergstrom, 2007; Chakrabarty et al., 2014; Lack et al., 2014; Long et al., 2013). For instance, organic aerosols (OA) are commonly co-emitted with BC from biomass burning. The internal and external mixing of OA and BC have been suggested to strongly alter the optical properties of BC, increasing the absorption ability in a specific wavelength, causing a stronger climate warming effect (Cappa et al., 2012; Nakayama et al., 2014). Whereas the heterogeneous ice nucleation of BC under diverse environmental conditions shows contrasting results (Brooks et al., 2014; Fan et al., 2016; Kulkarni et al., 2016; McCluskey et al., 2014; Petters et al., 2009; Qian et al., 2014; Vergara-Temprado et al., 2018).

BC is indeed linked to adverse health effects (Bove et al., 2019; Brown, 2013; Jia et al., 2020). For instance, toxic compounds such as polycyclic aromatic compounds (PAHs) have been shown to be bound with black carbon. A large proportion of anthropogenic BC emissions occur in urban regions, home to most of the human population. The urban BC sources include industrial

production, transportation, electrical production, and heating systems (IPCC, 2013). Air traffic is a major transportation venue in the world (ICAO, 2016). The contribution of BC emission from airplanes has been rising because of the expansion of aviation in the last decades (ICAO, 2016). There are several studies on the air pollution characterizations at airports (Rahim et al., 2019; Rivas et al., 2020) and experimental research of BC emission from airplane engines (Abegglen et al., 2016; Chen et al., 2019; Elser et al., 2019; Parent et al., 2016), revealing BC emission is even larger when airplanes are near or on the ground, in comparison with climbing and flying in the sky (ICAO, 2016). To our knowledge, there have been limited studies on in-situ real-time BC emission at the airport that are needed for a comprehensive assessment of the link between airplanes emitted BC and the health hazards of people living close to the airports.

The importance of snow on atmospheric chemistry and physics of the urban regions has been reported (Ariya et al., 2018). Aerosols are known to promote the formation of ice nuclei that can ultimately lead to the precipitation of snow in the atmosphere (Rangel-Alvarado et al., 2015). During the snowfall, aerosols like BC can be scavenged by snowflakes (Ariya et al., 2018; Pal et al., 2020; Rangel-Alvarado et al., 2019; Wang et al., 2021). Furthermore, as snowpack is porous, it can adsorb combustion emitted gas and particles like BC and PAHs (Nazarenko et al., 2016, 2017). BC has been suggested to change snow albedo, and affect the snow melting process (Bond et al., 2013). Snow organic compounds have been shown to undergo physicochemical processes including re-emission to air, upon melting (Nazarenko et al., 2016, 2017). Halogenated salts are commonly added as a de-icing agent in snowy cities, affecting the oxidation potential of the lower atmosphere (Hall et al., 2020; Pal et al., 2020; Rahim et al., 2019; Rangel-Alvarado et al., 2019).

In this study, we aimed to develop real-time dataset on selected physicochemical characteristics of BC, in a model cold-climate city of Montreal, Canada (Nazarenko et al., 2017;

Pal et al., 2020; Rangel-Alvarado et al., 2015). Concurrently, selected air co-pollutants (such as particulate matters, CO, NO_x) were analyzed. We herein evaluated BC's distributions and accumulation in the boundary layer. We also explored whether the BC concentration close to urban hotspots in residential areas is drastically elevated in the cold climate to cause potential adverse health. Lastly, as there are limited data on the impact of COVID-19 pandemic lockdowns on pollutant emissions in cold-climate cities, we explored a suite of air pollutants prior to, during the lockdown and after partial re-openings, pointing to the significance of anthropogenic activities in air quality.

2.2 Methodology

2.2.1 Black carbon analysis

A photoacoustic extinctiometer (PAX, Droplet Measurement Technologies, Inc.) with 870 nm laser module is used to in-situ measure absorption coefficient (B_{abs}) of BC from ambient air. PAX samples air with a 1 L/min flow rate. When air is drawn into the sampling chamber of PAX, the 870 nm laser will heat up BC particles in the air since few aerosols, except BC, can absorb light at 870 nm wavelength. Subsequently, the heated BC particles transfer heat to the surrounding air, generating pressure waves which can be detected by a sensitive microphone inside the chamber to get B_{abs} (Mm^{-1}) of the sample in one-second resolution:

$$BC\ Mass\ (\mu g/m^3) = B_{abs}\ (Mm^{-1})/BC\ MAC\ (m^2/g) \quad (1)$$

The calibration of PAX was performed by using manufacturer-recommended material, glassy carbon spheres (GCS). GCS were nebulized by an aerosol generator and then passed through PAX to generate B_{abs} values which were greater than 5000 Mm^{-1} for 30 to 60 seconds. BC

mass concentration was calculated directly by using B_{abs} and literature and manufacturer's recommended mass absorption cross-section (MAC) (4.74 m^2/g at 870 nm) at ambient temperature and pressure (Bond & Bergstrom, 2007; Selimovic et al., 2019), as is shown in equation (1). It should be noted that BC MAC can increase depending on the BC mixing state.

PAX also provides a scattering coefficient (B_{scat}). B_{scat} is measured by a nephelometer inside the chamber, and respond to all kind of particles regardless the size, morphology, and chemical compositions. $(NH_4)_2SO_4$ was used to calibrate B_{scat} as it can scatter light, yet it can hardly absorb it. $(NH_4)_2SO_4$ solution was aerosolized to pass through PAX to generate B_{scat} values which were greater than 5000 Mm^{-1} for 30 to 60 seconds.

$$B_{ext} = -\frac{1}{0.354}\ln\frac{I}{I_0}\cdot 10^6\ [Mm^{-1}] \quad (2)$$

The calculation of the calibration process is shown in equation (2), where B_{ext} is the extinction coefficient which can also be calculated by summing up B_{abs} and B_{scat} ($B_{ext} = B_{scat} + B_{abs}$). I_0 is the average laser power before and after calibration, and I is the laser power during calibration. To calibrate B_{scat}, B_{ext} must be calculated based on Equation (2), then plot calculated B_{ext} with measured B_{scat} to gain the correction factor (the slope of the linear regression) since B_{abs} of $(NH_4)_2SO_4$ can be negligible. Yet to calibrate B_{abs}, ($B_{ext} - B_{scat}$) should be plotted against B_{abs} because the scattering of GSC cannot be neglected. It should be noted that the calibration process assumes a linear response of the instrument up to the calibration absorption values.

The systematic error of PAX on BC Mass mainly comes from the value of BC MAC (mass absorption cross-section). The value of BC MAC used in this study is 4.74 m^2/g. This value is calculated based on two reasons: (1) Bond and Bergstrom (2007) recommended the value of BC MAC at 550 nm is 7.5 ± 1.2 m^2/g; (2) BC MAC is inversely related to wavelength. Yet, Bond and

Bergstrom (2007) noted that BC MAC can increase with the mixing state. For thickly coated particles, the absorption enhancement can be up to 50% for BC aggregates (Bond & Bergstrom, 2007). BC MAC varies from 4.74 m^2/g to 7.11 m^2/g. Thus, BC Mass reported in this work can be overestimated if BC particles are more coated than the value of 4.74 m^2/g.

Both BC Mass and B_{scat} are reported in the format of average values adding or subtracting standard errors.

2.2.2 High-resolution electron microscopy

The details of HR-S/TEM-EDS were described elsewhere (Pal et al., 2020; Rahim et al., 2019; Rangel-Alvarado et al., 2015). The TEM SiO_2-membrane grids were analyzed using a high-resolution FEI. Tecnai G^2F20 S/TEM microscope with a field emission gun. Images were acquired using an Advanced Microscopy Technique, Corp. (AMT) XR80C CCD Camera System, which was previously used for snow samples (Rangel-Alvarado et al., 2015). The AMT was adapted for collecting aerosols directly on the grid to further analyze the size, morphology, and chemical compositions of aerosol samples with high resolution.

2.2.3 Sampling Sites, observation, and snow collection

Air sampling is continuously conducted in downtown Montreal. The instruments are placed inside the laboratory of Otto Maass Building (45°30'N 73°34'W), with direct ambient air inlets, in the heart of downtown Montreal at McGill University (Pal et al., 2020; Rahim et al., 2019). The laboratory maintains a constant temperature, pressure, and relative humidity to ensure the instruments work optimally. Whereas particle observations near the Montreal-Pierre-Elliott-

Trudeau International Airport (Quebec, Canada) were performed at a public part (Westwood Park; 45°27'N 73°45'W) which is only 200 meters away from the airport runway and in the residential areas. The BC observations were conducted on the weekends prior to the COVID-19 shutdowns, during the total closure and after partial reopening in Montreal.

2.2.4 Aerosol and snow collection

A Micro Orifice Uniform Deposit Impactor (MOUDI, model 100-R, MSP Corp., Shoreview, MN, USA) was used to collect size-fractionated aerosol samples. MOUDI was operated on the roof with an inlet flow rate of 30 L/min and set up for 12-hour runs starting from 8 am. Teflon quartz substrate with TEM grids attached was used to make sure the samples can be used in TEM based on the method our group developed (Hudson & Ariya, 2007).

Snow samples were collected at Westwood Park by following the procedures described in detail elsewhere (Rangel-Alvarado et al., 2015). Generally, snow samples were collected during the snow precipitation events from the top 2 cm of the surface, and the aged snow taken at least 5 cm beneath the snowpack surface with sterile equipment and clean suits. All samples were kept in pre-sterilized amber chambers, frozen immediately after collection at -10 ± 2 °C, like ambient temperature during sampling. Small amounts of collected samples were transferred to a centrifuge tube with sterilized spoon under clean conditions. The centrifuge tube was kept frozen for high-resolution scanning/transmission electron microscopy (S/TEM) with energy dispersive X-ray spectroscopy (HR-S/TEM-EDS) analysis.

2.2.5 Other air co-pollutant data analysis

The hourly-averaged concentrations of fine particulate matter ($PM_{2.5}$), carbon monoxide (CO), nitrogen dioxide and monoxide (NO_x) and ozone (O_3) are obtained from The Air Quality Monitoring Network (RSQA), conducted by Environmental and Climate Change Canada (ECCC) and City of Montreal, which provides data from the monitoring stations on the Island of Montreal including stations both in downtown and near the Montréal-Pierre-Elliott-Trudeau International Airport (YUL Airport) (NAPS, 2021). The $PM_{2.5}$ continuous measurements are done by a synchronized hybrid ambient real-time particulate monitor (SHARP 5030). A CO Analyzer (Thermo 48i) is used, which utilizes the gas filtration correlation technology. A chemiluminescence NO-NO_2-NO_x Analyzer (Thermo 42i) is used for the quantification of NO_x. O_3 is measured by a UV-photometric Ozone Analyzer (Thermo 49i) (Hall et al., 2020). All the data are provided in hourly averages with 24 data points per day. The unit of CO, O_3 and NO_x is ppb, while the unit of $PM_{2.5}$ is $\mu g/m^3$, as is shown in Table 2 to Table 5. All the concentrations are reported in the format of average values adding or subtracting standard errors.

The back trajectory analysis was performed on internet based HYSPLIT model provided by Air Resources Laboratory (Rolph et al., 2017; Stein et al., 2015).

2.3 Results and Discussions

2.3.1 BC and selected co-pollutants emission in a cold-climate city

Montreal is a typical cold-climate city (Järvi et al., 2014) where winter lasts for 5 months (spanning from December 1st to April 20th, according to ECCC), receiving about 209 cm of snow per year. The long winter and low temperature lead to the need for additional heating, such as the

heating system of buildings in the whole city and car idling, increasing the usage of fuels and, thereby, emission of BC (Bond et al., 2013).

Previous observations have shown that the highest number density of airborne nanoparticles in City of Montreal occurs during the winter (Pal et al., 2020). Hall et al. (2020) have shown the high oxidation potential from anthropogenic photolabile chlorine in the photochemical process is due to de-icing salts during winter. In this study, we explored whether the mass concentration of BC showed a similar trend to what was previously observed for nanoparticles (Pal et al., 2020) and chlorine (Hall et al., 2020), *i.e.,* a maximum peak for BC Mass during the long winter in this cold-climate city and whether the existence of the snow affects the black carbon distribution and snow physicochemical properties.

To test this hypothesis, BC Mass from July 2019 to June 2020 (except October 2019) is shown in Figure 2.1A. The real-time B_{abs} data is also presented in the supplementary information (Figure A5). Although data of October were absent because of repairing the instrument, BC Mass in downtown Montreal showed a bimodal variation. BC emissions reached a peak before or in July (0.365 ± 0.007 μg/m^3), yet decreased through summer and autumn, and showed another peak during the winter (0.433 ± 0.013 μg/m^3), then decrease again until next spring. The long duration of sunshine in summer has been suggested to promote the photochemical reactions of organic carbon internally or externally mixed with BC, increasing the hygroscopicity of BC, and accelerating the wet deposition of BC in the atmosphere (Bond et al., 2013; Brooks et al., 2014; Zhang et al., 2019). Summer rainfalls may facilitate frequent wet deposition of BC. However, the BC fate in winter in the cold climate is indeed complex. More snowfalls in long winter can decrease BC Mass by ice nucleation and wet deposition (Hadley et al., 2010; Liu et al., 2020), yet the

application of the heating system and increasing consumption of fuels because of low temperature contribute to an extra BC emission.

Cold air has a higher density than warm air, the height of the boundary layer is thereby lower and thus more compact in the winter in contrast to the summer. Figure S6 shows HYSPLIT modeling results on two typical days in summer and winter, Jan. 20th, 2020 (winter) and Jun. 28th, 2020 (summer). It has already been shown that the height of the atmospheric boundary layer is higher in summer than in winter (Chan et al., 2013). Figure S6 demonstrates that BC entrapment is more important, and air dilution is less pronounced in cold seasons in comparison with warmer seasons, which can also partly explain the decreasing tendency from July 2019 to September 2019. Since snow is a ubiquitous feature of cold-climate, airborne BC particles can also be deposited on snowpack, following multiple cycles of melt and precipitations and release to the atmosphere, hydrosphere, and lithosphere (Ariya et al., 2018; Nazarenko et al., 2016, 2017). Such processes may explain the peaks observed between December 2019 to February 2020.

Due to the COVID-19 Pandemic in winter 2020, a lockdown was implemented from March 16th to May 25th in Montreal, which restricted most the non-essential human activities, and led to a significant reduction of BC emission from March to May (Figures 2.1 and A1). The sharp increase in June 2020 can be attributed to the partial reopening of the city. After a long term of lockdown, human activities gradually increased, which led to the increment of BC emission in the end.

The impact of photochemistry can be reflected in Figure 2.1B and Figure A1. Daytime is set from 9 am to 6 pm, whereas Nighttime is from 10 pm to 5 am. In this way, the variation of sunlight hours induced by seasons can be excluded. BC Mass at night is more than, or close to BC

Mass during daytime. BC Mass during daytime decrease is due to photochemistry. Nighttime BC emission in the atmosphere sustained for a relatively long time due to the lack of sunlight.

Figure A1 shows the diurnal variation of BC Mass based on all-year data, indicating the net effects of emissions due to anthropogenic activities. Like other aerosols (Pal et al., 2020; Rahim et al., 2019), BC has two peaks during the traffic rush hours. BC emission reached the maximum at 7 am to 8 am when citizens begin to commute to their workplaces on workdays. Around noon, it has been shown that BC Mass gradually decreases likely due to the variation of the atmospheric boundary layer (Begam et al., 2016). The height of the atmospheric boundary layer gradually increases and then peaks value at noon, causing the dilution of BC in the atmosphere (Begam et al., 2016). Later in the afternoon, BC emission increases again due to vehicle traffics and a decrease in the height of the boundary layer. Whereas at night, with less traffic and industrial production, the BC concentration variation remains steady unless strong wind or precipitation takes place. In brief, the diurnal variation, besides natural processes, also reveals the important role of human activities such as commute and transportation in BC emissions in urban areas (Bond et al., 2013; Jia et al., 2020; Liakakou et al. 2020).

The comparisons of BC Mass with concentrations of O_3, $PM_{2.5}$, CO, NO_2 are shown in Figure 2.1C, D, E and F. BC is one of the anthropogenic pollutants in this urban area. $PM_{2.5}$, CO and NO_2 in city are also mainly originated from human activities. Pearson correlation analysis was performed between BC Mass and concentrations of O_3, $PM_{2.5}$, CO, NO_2, NO and SO_2 respectively for each month (Table S5).

The results indicate a positive correlation between BC Mass with $PM_{2.5}$, CO, NO_2 and a negative correlation between BC Mass with O_3. BC consists of particles of various sizes. BC particles whose sizes are smaller than 2.5μm accounts for part of $PM_{2.5}$, which can confirm the

positive correlation between BC Mass and concentrations of $PM_{2.5}$. The positive correlation between BC with CO and NO_2 can be explained by anthropogenic activities including transport sector emissions. $PM_{2.5}$, CO and NO_2 are common anthropogenic pollutants. The positive correlation coefficients with these air pollutants confirms that BC emission in an urban area is mainly from anthropogenic sources. Whereas O_3 plays an essential role in photochemical processes, which oxidize organic carbon internally or externally mixed with BC in the atmosphere, facilitating the wet deposition of BC (Bond et al., 2013; Brooks et al., 2014; Zhang et al., 2019), and decreasing the atmospheric BC Mass, likely indicating a negative correlation between O_3 and BC.

2.3.1.1 Meteorological winter in a cold climate: Up to 5 months

Although the variation of BC Mass shows a peak during winter, it should be noticed that BC Mass in warm-climate cities, like Nanjing (Tan et al., 2020), Athens (Liakakou et al. 2020) and Czech (Mbengue et al., 2020), is greatest during winter as well, which indicates large BC Mass during winter is prevalent. Yet winter in the cold-climate sites lasts longer, comparing with warm-climate sites where winter usually ends in February. The 5-month winter in Montreal, a cold-climate city, makes it possible that the duration of large BC Mass is longer than warm-climate sites. Although this speculation cannot be fully examined directly because of the lack of BC Mass data from January 2019 to May 2019, the increase of CO in fall and winter can be used as BC proxy, indirectly (Rahim et al., 2019). Furthermore, according to the results illustrated above, CO shows a positive correlation with BC, with Pearson correlation coefficients varying from 0.2909 to 0.9194 (Table A5). Consequently, CO can be used to estimate the variation of other anthropogenic pollutants like BC.

Table A2 shows the variations of CO from January to June in the last four years. Table A3 illustrates the results of t-test between January with the other five months respectively. The values in the bracket of March 2020 are obtained by using data of the first 15 days of March 2020 (before lockdown). There is no significant difference between January with February and March (except for March 2018) in the past four years. It accounted for high concentration of CO maintaining until April, that is still meteorological winter in Montreal. As such, it is logical to speculate that the duration of large BC Mass can also maintain from December to the end of March, showing the uniqueness of cold-climate sites. The longer duration of large BC Mass in cold-climate sites may cause more health hazards to human health.

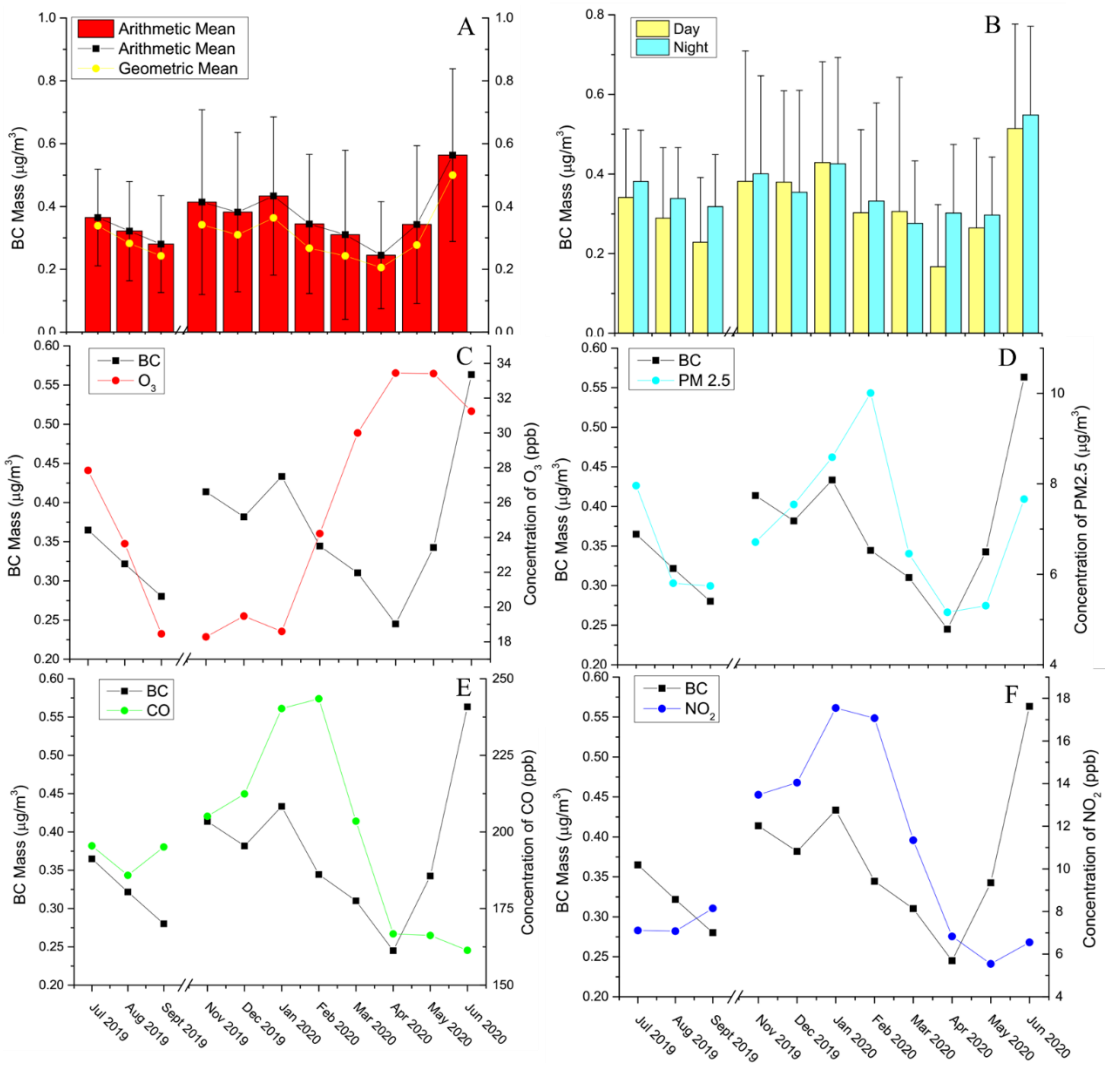

Figure 2.1. Monthly mean values of BC Mass (**A**), Day-Night comparison of BC Mass in each month (**B**), comparison of BC with O_3 (**C**), $PM_{2.5}$ (**D**), CO (**E**) and NO_2 (**F**). The error bars in **A** and **B** indicates the standard deviations.

2.3.2 COVID-19 Pandemic and impacts on the urban environment

SARS-CoV-2 causing COVID-19 disease was first reported in Wuhan, China in December 2019. Since then, the World Health Organization (WHO) declared it to be a worldwide pandemic, infecting about 150 million people around the world, causing over 3 million deaths all around the world, and it is still counting (WHO, 2021c). During the COVID-19 lockdowns, several

researchers have shown a decrease of air pollution around the city worldwide (Bao & Zhang, 2020; Gautam, 2020; Kanniah et al., 2020; Lee et al., 2020; Lian et al., 2020; Liu et al., 2020; Mahato et al., 2020; Mandal & Pal, 2020; Nakada & Urban, 2020; Zhang et al., 2020; Briz-Redón et al., 2021; Liu et al., 2021; Park et al., 2021; Putaud et al., 2021).

As the lockdown policy obviously constrain the spread of COVID-19 among citizens, many countries complied with it. to protect their people. COVID-19 not only changes the world profoundly but also provides an opportunity for scientists to observe and evaluate anthropogenic impacts on the environment during the lockdown period when almost all unnecessary economical activities are stagnant. Earlier in China and Italy, the sharp decreases in CO_2, NO_x and particulate matter ($PM_{2.5}$, PM_{10}) emissions were immediately reported (Bao & Zhang, 2020; Gautam, 2020; Liu et al., 2020; Zhang et al., 2020; Putaud et al., 2021). Similar phenomena were found in India, Brazil, and Southeast Asia (Kanniah et al., 2020; Mandal & Pal, 2020; Nakada & Urban, 2020). The decrease of air pollutants including CO, NO_x, $PM_{2.5}$, and the increase of O_3 has been widely reported (Table 2.1).

It is noteworthy that in urban air quality both meteorological variability and anthropogenic emission change impact urban air pollutant concentrations and should be thus considered together. In this study, we consider bi-modal distribution of BC Mass based on two points: (1) decreasing trend from July 2019 to Sept 2019; (2) peaking trend during wintertime (January 2020). BC emission during these two periods was not impacted by the COVID-19 Pandemic. Furthermore, BC Mass peaking in January has been widely reported in cities around the world (Liakakou et al. 2020; Mbengue et al., 2020; Tan et al., 2020). Accordingly, we believe the conclusion on bi-modal distribution is likely reliable in this study.

Table 2.1. Selected variations of air pollutants during lockdown all over the world.

Location	Pollutant	Variation	Comments	Reference
California, US	NO_2	-38%	Mar 19th ~ May 7th, 2020, compared with Jan 26th ~ Mar 18th 2020	Liu et al., 2020
	CO	-49%		
	$PM_{2.5}$	-31%		
	O_3	+14%		
	PM_{10}	+10%		
Seoul, Korea	NO2	-39.91%	March 2020 compared with March 2019	Park et al., 2021
	CO	-15.25%		
Barcelona, Spain	CO	< -35%	April 2020, compared with April 2019	Briz-Redón et al., 2021
	NO2	< -35%		
	O3	+15% ~ 25%		
	PM10	-35% ~ -25%		
	SO2	< -35%		
UK	NO2	-42%	Mar 23rd ~ May 31st, 2020, compared with the same period 2015-2019	Lee et al., 2020
	O3	+11%		
Wuhan, China	PM2.5	-36.9%	Jan 24th ~ Feb 23rd, 2020, compared with Dec 24th, 2019 ~ Jan 23rd 2020	Lian et al., 2020
	NO2	-53.3%		
	O3	+116.6%		
	PM10	-40.2%		
	CO	-22.7%		
	SO2	-3.9%		
NCT Delhi, India	PM10	-51.58%	Mar 25th ~ Apr 14th, 2020, compared with Mar 2nd ~ Mar 21st 2020	Mahato et al., 2020
	PM2.5	-53.11%		
	SO2	-17.97%		
	NO2	-52.68%		
	CO	-30.35%		
	O3	+0.78%		

	NH3	-12.33%		
São Paulo, Brazil	CO	-29.8%	Mar 24th ~ Apr 20th, 2020, compared with Feb 25th ~ Mar 23rd 2020	Nakada & Urban, 2020
	PM10	+7.7%		
	PM2.5	-0.3%		
	NO	-40.4%		
	NO2	-21.5%		
	O3	+10.8%		
Northern China	SO2	-6.76%	Jan 28th ~ Mar 21st, 2020, compared with Jan 1st ~ Jan 27th 2020	Bao & Zhang, 2020
	PM2.5	-5.93%		
	PM10	-13.66%		
	NO2	-24.67%		
	CO	-4.58%		
Malaysia	PM10	-26% ~ -31%	Mar 18th ~ Apr 30th, 2020, compared with the same period in 2018 and 2019	Kanniah et al., 2020
	PM2.5	-23% ~ -32%		
	NO2	-63% ~ -64%		
	SO2	-9% ~ -20%		
	CO	-25% ~ -31%		
Ispra, Italy	SO2	-29%	Mar 9th ~ May 4th , 2020, compared with Feb 17th ~ Mar 8th 2020	Putaud et al., 2021
	O3	+21%		
	NO	-44%		
	NO2	-49%		

The first lockdown in Montreal started on March 16, 2020 and lasted for more than two months. The city partially reopened starting from May 25, 2020. During the lockdown, most the unnecessary activities were restricted. Transportation and industrial production decreased dramatically. With restricted human activities, emissions of BC and other air pollutants from anthropogenic sources thereby decreased.

BC Mass variation before the lockdown, during the lockdown and partial reopening in downtown Montreal, is shown in Figure 2.2A and Figure A4A. The average BC Mass were 0.340 $\pm$ 0.014 $\mu g/m^3$, 0.268 $\pm$ 0.004 $\mu g/m^3$ and 0.551 $\pm$ 0.012 $\mu g/m^3$ respectively. The statistical analysis showed that there was a significant difference when comparing BC Mass during the lockdown with BC Mass before the lockdown or partial Reopen (Table 2.3). Since the lockdown spanned from mid-March to the end of May, the seasonal change effect on BC Mass distribution was considered. To exclude the impacts from seasonal changes, the statistical analysis was conducted for BC Mass from Mar 1st to Mar 15th (before lockdown) with BC Mass from Mar 16th to Mar 31st (during lockdown) and BC Mass from May 1st to May 24th (during lockdown) with BC Mass during May 25th to Mar 30th (partial reopening). As shown in Table A1, significant differences between these time periods were observed. The results were not surprising as BC is generated by anthropogenic sources in urban areas. When the lockdown policy restrained the BC emissions, BC Mass certainly decreased too.

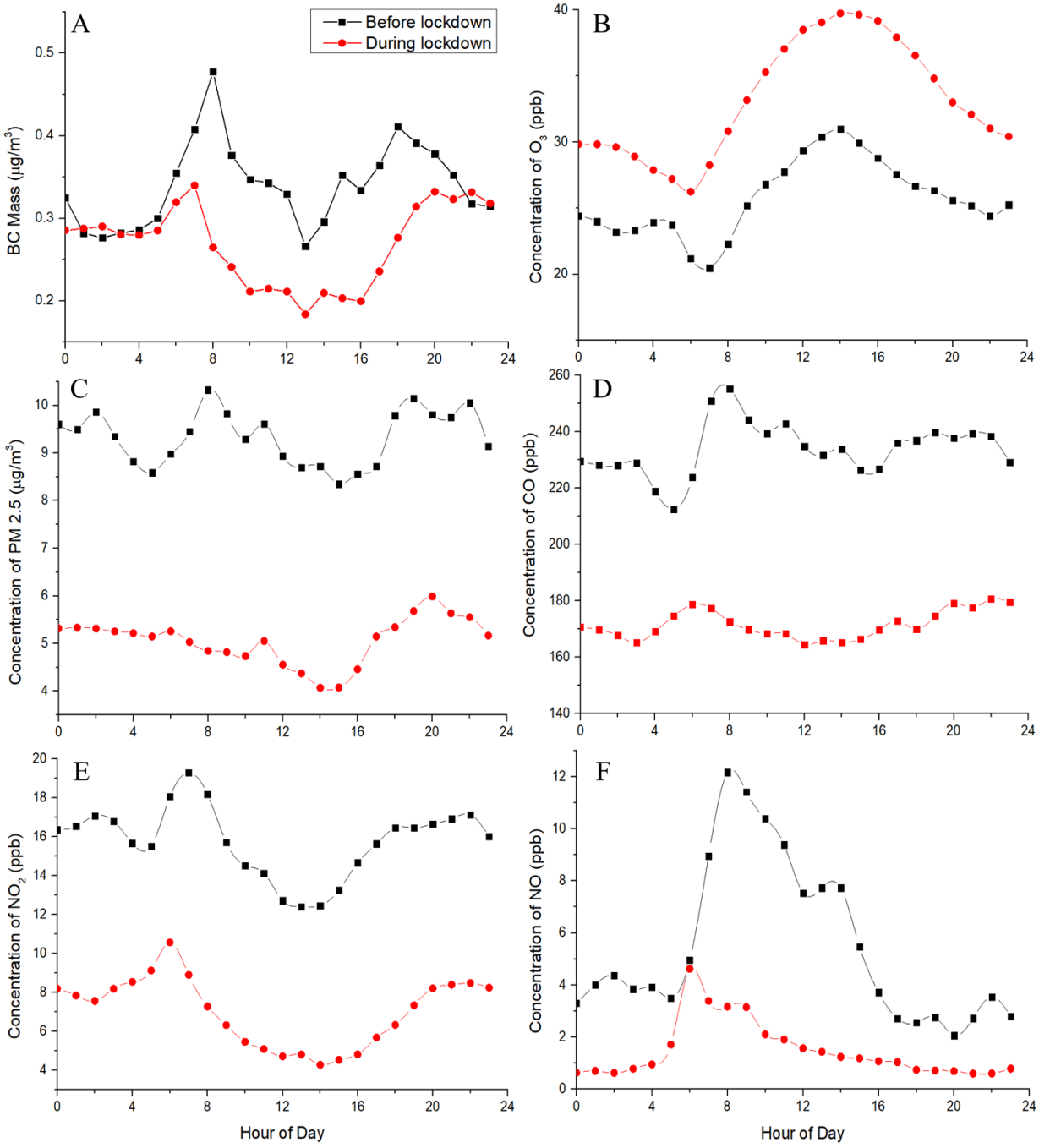

Figure 2.2. Diurnal variation of the concentrations of BC (**A**), O_3 (**B**), $PM_{2.5}$ (**C**), CO (**D**), NO_2 (**E**) and NO (**F**) in downtown Montreal before lockdown (black line) and during lockdown (red line). The period of "Before lockdown" is set from Feb. 1st to Mar. 15th, and the period of "During lockdown" spans from Mar. 16th to May 24th.

The impact of COVID-19 on other air pollutants, rather than only BC were illustrated in Table 2.3 and Figure 2.2. The concentrations of $PM_{2.5}$, CO, NO and NO_2 decreased from ~ 26% and up to 72%. Yet, the concentration of O_3 increased by about 30% likely due to the declining emission of other photochemical-related pollutants including CO and NO_x. Fan et al. (2021), Huang et al. (2021) and Putaud et al. (2021) attributed the increment of O_3 to the decline of NO_x emission during the lockdown. As NO emission decreased, the number of NO_2 converted by NO decreased. Additionally, since there was less NO titrating O_3, the concentration of O_3 increased correspondingly. Yet, Fan et al. (2021) and Huang et al. (2021) observed enhanced secondary pollution in China, which was not observed by Putaud et al. (2021) in northern Italy and this work in Montreal, Canada, which may be due to a lack of data on volatile organic aerosols and PM_{10} in Montreal, or because of regional disparity. Although BC itself is photochemical inert, organic carbon internal or external mixed with BC can be oxidized by O_3. Thus, the decreasing emission of BC also contributes a part to the increment of O_3. However, the situations in the period of partial Reopen are more complex. The partial reopening was a gradual process during which the restrictions were gradually and selectively lifted. Not all urban activities were fully recovered. Consequently, the recovery of O_3, CO, NO and NO_2 emissions was not as clear as during the complete lockdown (Figure A4). The recovery of BC and $PM_{2.5}$ emissions was statistically clearer, as shown in Figure A4. With the restrictions removed gradually, a sharp increase of mass concentrations of BC and $PM_{2.5}$, notwithstanding the impact of seasonal changes should be also considered.

As depicted in Figure 2.1A, BC Mass decreased since July 2019, indicating the existence of another peak around July 2019. During the partial reopening period from May 25th to June 30th, 2020, the BC trend was in accordance with BC values in 2019. The recovery of $PM_{2.5}$ was less

pronounced than BC. It can be explained partly by the fact that $PM_{2.5}$ contains not only part of BC but also other non-BC particulate matter emitted by anthropogenic sources (Rahim et al., 2019). The observation of low concentrations of CO, NO and NO_2 are in accordance with transportation and industries which gradually recovered since June 2020.

The size of BC particles spans from nano-size to micro-size (Chakrabarty et al., 2014; Long et al., 2013). As such, BC particles greater than 2.5 μm are not included in $PM_{2.5}$ values. The variations of BC and $PM_{2.5}$ are not expected to be identical, as herein confirmed. It is to note that B_{scat} values may reflect the variation of particulate matters in wider size distribution, as the scattering chamber used in this study, responds to all particles, regardless of their size, morphology, and chemical composition.

As is shown in Table 2.3 and Figure A2A, B_{scat} decreased from 11.30 ± 0.39 Mm^{-1} to 5.60 ± 0.08 Mm^{-1} because of COVID-19 but increased back to 12.12 ± 0.52 Mm^{-1} during the partial Reopen period, almost at the same levels to B_{scat} before lockdown. Yet, seasonal changes are likely play a role. As shown in Figure A3, an increase of B_{scat} in June 2019 was observed, coinciding with solar radiation hinting to the importance of seasonal changes. Yet, in addition to photochemistry, the recovery of B_{scat} can also be in part, due to the reopening period in June 2020.

Table 2.2, and Table A4 provide detailed information for a suite of air pollutants. The impact of COVID-19 lockdown is statistically clear. Moreover, the variations of BC Mass, $PM_{2.5}$, CO, NO_2 and B_{scat} showed the lockdown not only decreased average concentrations of certain pollutants but also median values, 99th percentile values and 75th percentile values.

Table 2.2. The averages, standard deviations, median values, 99th percentile values, 1st percentile values, 25th percentile values and 75th percentile values for BC Mass, O_3, $PM_{2.5}$, CO, NO, NO_2 and B_{scat} from January 2020 to June 2020.

	Average	**Std**	**Median**	**99%**	**1%**	**25%**	**75%**
				BC Mass (μg/m^3)			
Jan-20	0.433	0.252	0.418	1.09	0.060	0.248	0.569
Feb-20	0.336	0.226	0.320	0.991	0	0.173	0.447
Mar-20	0.310	0.269	0.280	1.18	0	0.152	0.401
Apr-20	0.245	0.170	0.244	0.743	0	0.127	0.334
May-20	0.343	0.251	0.301	1.12	0	0.186	0.466
Jun-20	0.563	0.275	0.525	1.42	0.102	0.367	0.714

	Average	**Std**	**Median**	**99%**	**1%**	**25%**	**75%**
				O_3 (ppb)			
Jan-20	18.6	8.6	19.3	34.4	1.1	12.4	25.4
Feb-20	24.2	9.4	26.5	42.5	0.8	19.2	30.1
Mar-20	30.0	7.9	31.3	43.3	3.7	25.8	35.4
Apr-20	33.4	7.4	33.9	48.6	10.8	29.3	38.7
May-20	33.4	9.8	32.5	59.8	10.7	26.9	39.3
Jun-20	31.3	12.4	30.6	59.7	6.8	21.4	39.4

	Average	**Std**	**Median**	**99%**	**1%**	**25%**	**75%**
				$PM_{2.5}$ (μg/m^3)			
Jan-20	8.6	7.2	7.3	37.2	0.7	3.8	10.5
Feb-20	10.0	8.8	7.1	41.9	1.1	4.4	12.7
Mar-20	6.5	5.0	5.2	25.3	0.7	3.3	8.0
Apr-20	5.2	2.7	4.5	13.5	0.8	3.2	6.7
May-20	5.3	3.0	4.7	13.9	0.4	3.2	6.8
Jun-20	7.7	7.5	6.4	31.9	1.1	4.2	9.2

	Average	Std	Median	99%	1%	25%	75%
				CO (ppb)			
Jan-20	240.3	75.1	225.8	545.6	134.5	191.8	262.5
Feb-20	243.5	91.2	215.4	583.5	139.2	188.1	258.2
Mar-20	203.5	54.2	193.8	397.1	146.2	172.6	219.2
Apr-20	166.8	23.1	163.6	239.6	130.9	150.4	180.3
May-20	166.2	34.2	161.9	274.5	107.2	141.9	183.0
Jun-20	161.4	39.7	158.3	276.5	96.4	134.5	179.4
	Average	**Std**	**Median**	**99%**	**1%**	**25%**	**75%**
				NO (ppb)			
Jan-20	6.0	7.5	3.9	42.9	0.7	2.4	6.5
Feb-20	6.1	11.4	3.2	54.5	0.6	1.8	5.7
Mar-20	3.0	6.2	1.8	36.4	0.1	0.9	3.2
Apr-20	1.4	2.0	0.8	9.8	0.0	0.4	1.5
May-20	1.2	2.0	0.6	10.5	0.0	0.3	1.2
Jun-20	1.4	3.1	0.5	15.4	0.0	0.2	1.3
	Average	**Std**	**Median**	**99%**	**1%**	**25%**	**75%**
				NO2 (ppb)			
Jan-20	17.5	8.7	16.0	43.1	4.9	11.3	22.1
Feb-20	17.1	9.9	13.9	45.5	4.9	9.8	21.0
Mar-20	11.3	6.9	9.8	36.9	3.0	6.4	14.5
Apr-20	6.8	4.8	5.8	27.1	1.8	3.6	8.3
May-20	5.5	3.9	4.6	19.6	0.9	2.8	7.0
Jun-20	6.6	4.0	5.5	21.9	1.6	3.9	8.0
	Average	**Std**	**Median**	**99%**	**1%**	**25%**	**75%**
				Bscat (Mm^{-1})			

Jan-20	10.84	8.68	9.15	46.91	1.47	4.28	14.39
Feb-20	12.50	7.82	11.15	33.51	1.70	6.48	18.11
Mar-20	8.45	6.82	6.74	37.60	0.99	4.23	10.47
Apr-20	5.31	2.87	4.86	13.45	1.17	3.16	7.05
May-20	6.90	5.84	5.11	24.73	0.81	3.08	8.25
Jun-20	12.13	14.26	9.17	74.93	1.87	5.82	13.51

2.3.3 Case study: YUL Airport BC in comparison to Montreal downtown

Aviation is one of the domains that suffered a lot because of the COVID-19 Pandemic (ICAO, 2021). The worldwide lockdown, restrictions on international travel and high risk of infection in airplanes drastically reduced the number of travelers and flights, which in the end caused the big decline of aviation in the world (ICAO, 2021). Moreover, previous studies have shown that up to 97% of airborne particles, including PM2.5 which includes significant black carbon particles, are being released within airport regions (Camero, 2019; Mazaheri et al., 2011). YUL Airport is one of the third busiest airports in Canada with more than 236 thousand flights in 2019. It is a good place to show the impact of COVID-19 on aviation and the difference between urban areas (downtown Montreal) with the airport.

Table 2.3. Air pollutants concentrations with standard deviations in downtown Montreal during COVID19 Pandemic. The first column of P value shows the p values between the concentrations before lockdown and the concentrations during lockdown. And second column of P value shows the p values between the concentrations during lockdown and the concentrations after partial Reopen. The period of "Before lockdown" is set from Feb. 1st to Mar. 15th. The period of "During lockdown" is set from Mar. 16th to May 24th, and the period of "Partial Reopen" spans from May 25th to Jun. 30th.

	Downtown Montreal			
	Before lockdown	**During lockdown**	**Partial Reopen**	**P value**

BC Mass ($\mu g/m^3$)	0.340 ± 0.014	0.268 ± 0.004	0.551 ± 0.012	$P < 0.001$	$P < 0.001$
PM2.5 ($\mu g/m^3$)	9.19 ± 0.25	5.12 ± 0.06	7.50 ± 0.24	$P < 0.001$	$P < 0.001$
CO (ppb)	232.8 ± 2.6	171.6 ± 0.7	165.0 ± 1.4	$P < 0.001$	$P = 0.003$
O_3 (ppb)	25.8 ± 0.3	33.2 ± 0.2	31.2 ± 0.4	$P < 0.001$	$P = 0.226$
NO (ppb)	5.4 ± 0.3	1.5 ± 0.05	1.4 ± 0.1	$P < 0.001$	$P = 0.755$
NO_2 (ppb)	15.6 ± 0.3	7.0 ± 0.1	6.4 ± 0.1	$P < 0.001$	$P = 0.192$
B_{scat} (Mm^{-1})	11.30 ± 0.39	5.60 ± 0.08	12.12 ± 0.52	$P < 0.001$	$P < 0.001$

Table 2.4. Air pollutants concentrations with standard deviations near the YUL Airport during COVID-19 Pandemic. The period of "Before lockdown" is set from Feb. 1st to Feb. 29th. The period of "During lockdown" is set from May 1st to May 24th.

	YUL Airport		
	Before lockdown	**During lockdown**	**P value**
BC Mass ($\mu g/m^3$)	1.487 ± 0.148	0.347 ± 0.045	$P = 0.007$
PM2.5 ($\mu g/m^3$)	9.42 ± 0.30	4.80 ± 0.08	$P < 0.001$
CO (ppb)	238.7 ± 3.6	160.9 ± 0.9	$P < 0.001$
O_3 (ppb)	26.3 ± 0.3	34.4 ± 0.2	$P < 0.001$
NO	6.0 ± 0.5	0.9 ± 0.1	$P < 0.001$

(ppb)			
NO_2 (ppb)	13.7 ± 0.4	5.0 ± 0.2	P < 0.001
B_{scat} (Mm^{-1})	7.68 ± 0.96	3.64 ± 0.15	P = 0.003

Table 2.5. Comparisons of concentrations of air pollutants in downtown Montreal with near YUL Airport during COVID-19 Pandemic. The period of "Before lockdown" is set from Feb. 1st to Feb. 29th. The period of "During lockdown" is set from May 1st to May 24th.

	Before lockdown (February)		
	Downtown	**Airport**	**P value**
BC Mass ($\mu g/m^3$)	0.344 ± 0.016	1.487 ± 0.148	P = 0.005
PM2.5 ($\mu g/m^3$)	10.0 ± 0.3	10.5 ± 0.4	P = 0.188
CO (ppb)	243.5 ± 3.4	250.8 ± 4.7	P = 0.212
O_3 (ppb)	24.2 ± 0.4	23.7 ± 0.4	P = 0.622
NO (ppb)	6.1 ± 0.4	6.9 ± 0.7	P = 0.466
NO_2 (ppb)	17.1 ± 0.4	15.3 ± 0.5	P = 0.090
B_{scat} (Mm^{-1})	12.50 ± 0.58	7.68 ± 0.96	P < 0.001
	During lockdown (May)		
	Downtown	**Airport**	**P value**
BC Mass	0.290 ± 0.008	0.347 ± 0.045	P = 0.079

(µg/m^3)			
PM2.5 (µg/m^3)	4.9 ± 0.1	4.5 ± 0.1	P = 0.054
CO (ppb)	162.0 ± 1.1	146.5 ± 1.1	P < 0.001
O_3 (ppb)	34.1 ± 0.4	34.9 ± 0.3	P = 0.583
NO (ppb)	1.2 ± 0.1	0.5 ± 0.03	P = 0.006
NO_2 (ppb)	5.5 ± 0.2	3.3 ± 0.2	P < 0.001
B_{scat} (Mm^{-1})	5.17 ± 0.15	3.64 ± 0.15	P < 0.001

The atmospheric impacts of COVID-19 lockdown are shown in Table 2.4, Table 2.5, Figure 2.3, and Figure A2B. Similar to downtown Montreal, BC Mass, B_{scat} and concentrations of $PM_{2.5}$, CO, NO and NO_2 significantly decreased when lockdown started, in contrast to the concentration of O_3 significantly which was increased. It should be noticed that before lockdown, the concentrations of all these pollutants, except BC, are not distinct between downtown and the airport (Table 2.5). Notwithstanding than in previous studies, where the nanoparticles were measured, there was a clear increase close to the airport in comparison to the downtown (Rahim et al. 2019).

The trend for BC is different from other measured pollutants as shown in Table 2.5. BC Mass at the airport is significantly greater than that in downtown Montreal before lockdown. The relatively smaller B_{scat} at the airport indicates the particles at the airport intend more to absorb light,

instead of scattering light, revealing the higher proportion of BC in the air at the airport, compared with downtown Montreal.

Yet during the lockdown, there is no significant difference between these two regions in BC Mass, as most flights were stopped, and other anthropogenic activities were decreased concurrently. Furthermore, the change of B_{scat} also gives clues to the BC trends at the airport.

The comparison of BC Mass between downtown and the airport not only reflects the great impact of COVID-19 on aviation but also reveals the high concentrations of BC in the ambient air at the airport during the normal operation, which may pose a potential threat to the health of workers and nearby residents, living a few meters away from the airport.

2.3.4 Evidence for airborne black carbon deposition in snow

The HR-S/TEM-EDS results (Figure 2.4) on the snow samples, both freshly falling and aged snow, collected from the airport illustrate several black carbon-types particles and carbon nanostructures in snow. There are several processes that can explain the existence of these black carbon type and carbon nanostructures, which have been observed previously in the air (Rahim et al. 2019), and herein observed, in freshly falling and aged snow. It is noteworthy that previous studies have demonstrated that common BC structure, like those in Figure 2.4, can integrate and form aggregates of carbon spheres (e.g., Bond et al., 2013). These combustion-related particles are likely scavenged by snow crystals as it falls. The large surface areas of snowflakes may facilitate the partitioning between snow and particles or chemicals in the atmosphere, making snow an excellent scavenger when it falls (Lei & Wania, 2004). Furthermore, both wet and dry deposition processes of anthropogenic particles on snow have been previously observed (Hadley et al., 2010;

Liu et al., 2020). Upon the multiple precipitations and melt- processes, several black carbon particles or aggregates were observed in the snowpack, confirmed by HR-S/TEM analysis (Figure 2.4).

Several researchers have indicated that black carbon can serve as effective ice nuclei (Brooks et al., 2014; DeMott et al., 1990; McCluskey et al., 2014; Murray et al., 2012). The importance of BC on atmospheric ice nucleation processes and the magnitude of the radiative forcing due to BC on snow, are still being debated (Brooks et al., 2014; Fan et al., 2016; Kulkarni et al., 2016; McCluskey et al., 2014; Petters et al., 2009; Qian et al. 2014; Vergara-Temprado et al., 2018). BC particles in the snow might likely have different origins, configuration, composition, and other physicochemical properties (Bond et al. 2013; Brooks et al., 2014; Dou & Xiao, 2016; Lack et al., 2014; Liu et al., 2020; McCluskey et al., 2014; Qian et al., 2014). As such, air-snow partitioning is expected to occur both on the surface of snow and on particle interfaces (Lei & Wania, 2004). Recently, there are increasing evidence that several types of anthropogenic particles that are found in snow can alter the ice nucleation of BC and its radiative forcing (Ganguly & Ariya, 2019; Ming & Wang, 2021).

Externally or internally mixed organic pollutant particles like PAHs, a known health hazard associated with the BC-type particles, also undergo physicochemical processes (Nazarenko et al., 2016, 2017). For instance, after snow melts, the aggregated BC particles may be dissolved in meltwater or released into the air. As snow ages, the partitioning coefficient of particles and compounds in snow is expected to vary, leading to the re-emission (Hansen et al., 2006). Furthermore, as the wind blows across the surface of the snowpack, the decreased pressure on the surface can induce the re-emission of particles from snow surfaces too (Hansen et al., 2006). Due

to the high importance of BC in ice nucleation, radiation as well as human and ecosystem health, further targeted physicochemical research is recommended.

2.3.5 Airborne black carbon decrease during the snowfall

Table A6 shows the impacts of snow on airborne BC Mass values, using one snowfall event. Snow precipitation reported values are averaged over 24 hours. This snowfall event occurred in part of the December 31, 2019 with less intensity and continued to much higher precipitation intensity on January 1, 2020, whereas January 2, 2020 received no precipitation. The average daily temperatures over 3 days are nearly constant around the freezing point. During the snow fall events, BC values decreased, particularly when snow fall intensified, whereas during the snow free day of January 2, 2020, BC Mass values recovered to the highest levels on three days. Thereby snowfall scavenged BC particles bringing it to the surface. This observation is in accordance with the results from Hadley et al. (2010) who also found the evidence that snow could scavenge BC and decrease BC Mass in ambient air. Hadley et al. (2010) have performed their statistical analysis and drew conclusions based on the data of several snow events at three different sites. In this study, we lacked enough data for snow events during the winter of 2019-2020 to draw a statistically valid estimation of scavenging processes, yet it should be considered in future studies.

Beside BC, other emerging contaminants are found in snow, including carbon nanostructure (Rangel-Alvarado et al., 2019), microplastics (Wang et al., 2020), nanoparticles (Pal et al., 2020; Rahim et al., 2019; Rangel-Alvarado et al., 2015) and halogen compounds (Hall et al., 2020). More importantly, recent research reveals that microplastics in snow may cause an overestimation of BC and its effects on the climate since several analytical equipment for BC

detection are unable to distinguish microplastics from BC (Ming & Wang, 2021). This finding indicates the questions of whether and how BC will interact with other emerging contaminants, for instance, toxic nano-metals such as Ni and Cr, as observed in this study (Figure A7). Since BC has been shown to contain both organic and inorganic compounds, and various organic compounds are known to interact on particles (Eltouny & Ariya, 2012; Canagaratna et al., 2015). Potential effects upon the photochemical or heterogeneous chemical transformation of a wide range of particles should be understood. Future research on these topics is thus recommended.

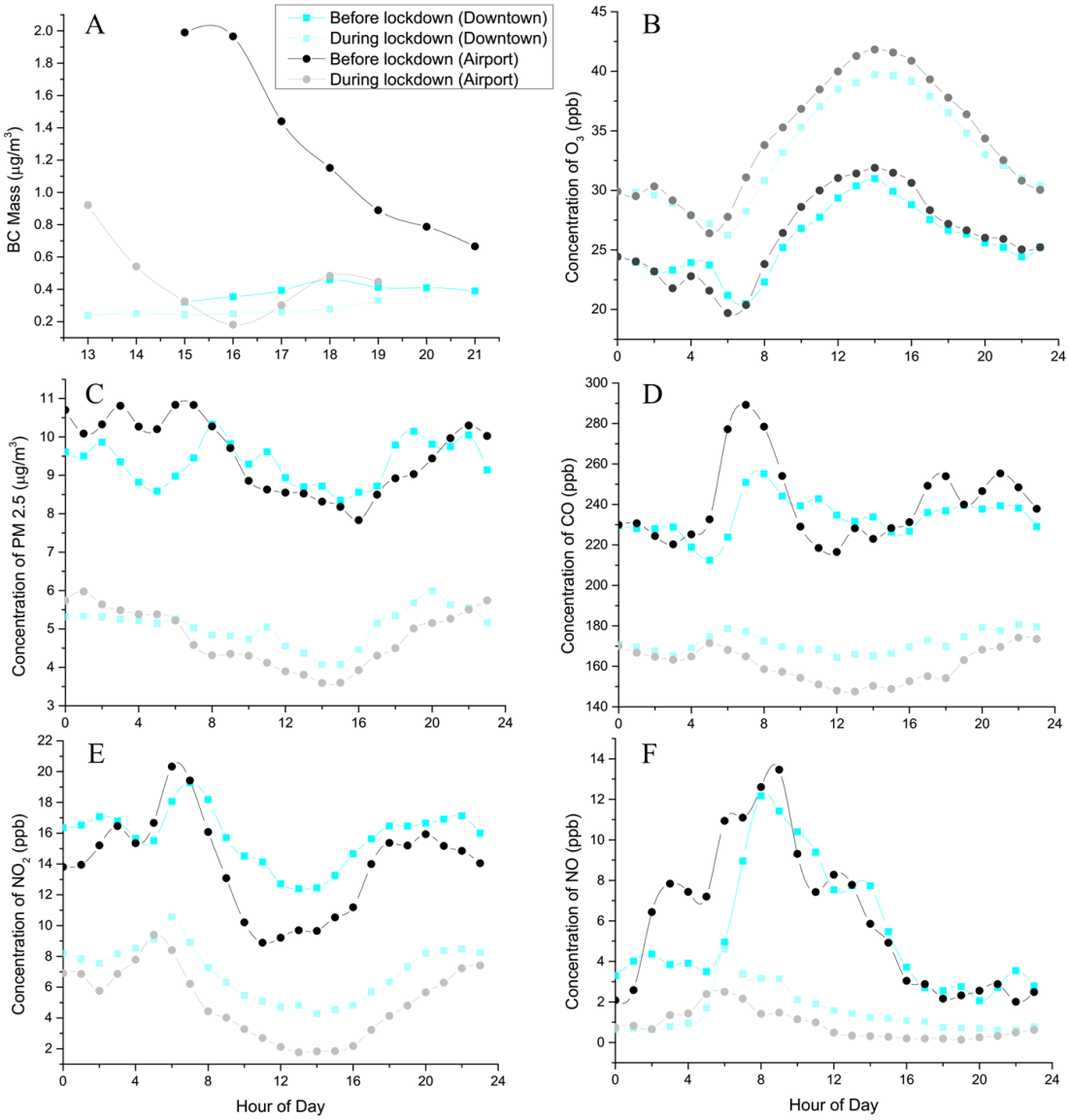

Figure 2.3. Comparisons of concentrations of BC (**A**), O_3 (**B**), $PM_{2.5}$ (**C**), CO (**D**), NO_2 (**E**) and NO (**F**) in downtown Montreal (cyan) with near YUL Airport (black) in COVID-19 Pandemic. For **A**, the period of "Before lockdown" is set from Feb. 1st to Feb. 29th, and the period of "During lockdown" is from May. 1st to May 24th. For **B** to **F**, the period of "Before lockdown" includes Feb. 1st to Mar. 15th, and the period of "During lockdown" spans from Mar. 16th to May 24th.

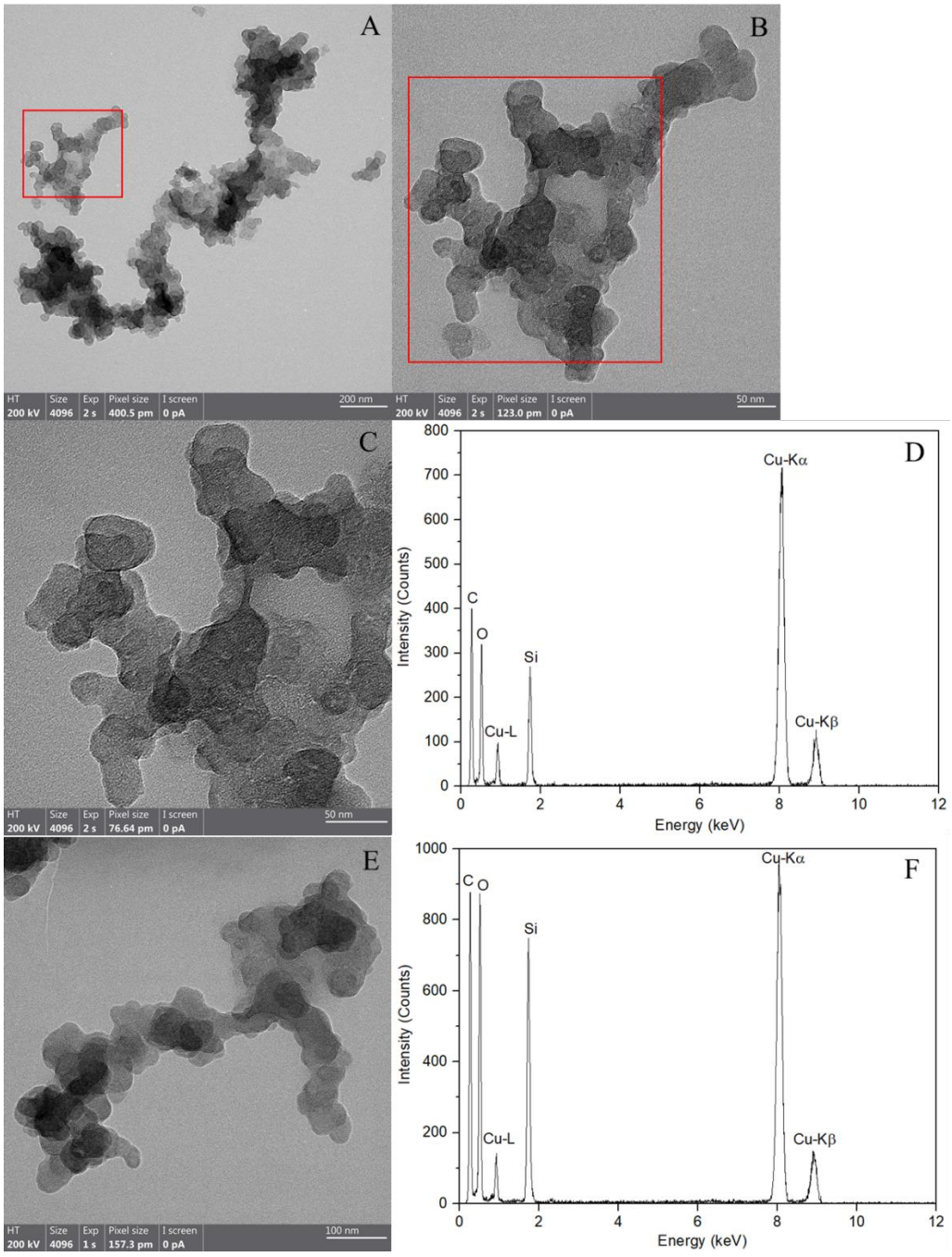

Figure 2.4. HR-S/TEM-EDS results of the aged snow samples collected from the airport. **D** and **F** are EDS results for **C** and **E**, respectively.

2.3.6 Potential added values of this BC data for cold-climate modelling

This work provides data of both BC Mass and B_{abs} in a cold-climate model city of Montreal, which is beneficial for present models of radiative forcing based on anthropogenic BC emissions in urban areas. Data on number density, size, refractive index, mass concentration and absorption coefficient of BC have been identified as key inputs to evaluate the concentrations and radiative forcing of BC in most modelling (Bond et al. 2013). Such data are rare for cold-climate cities. Considering the long winter and long duration of high BC Mass in cold urban regions, as discussed above, it is greatly recommended for future work in developing regional cold-climate models to evaluate urban air quality and climate impacts.

2.4 Concluding remarks

We herein present one-year real-time data on mass concentration of BC, together with key air co-pollutants, in a model cold-climate city of Montreal, which is crucial for various atmospheric modelling. Annual BC mass concentration exhibited a bi-modal distribution and BC winter peak lasts longer than 3 months in comparison to mild or warm-climate cities, due to distinct cold-climate meteorology. During the snow episodes, airborne BC mass concentration decreased, while black carbon particles or carbon nanomaterials appeared in the snow, indicating air-snow interaction of anthropogenic pollutants took place. Furthermore, we demonstrated that airborne BC mass concentration in the residential areas around the airport is over 400% higher than an already in a polluted downtown. During the COVID-19 lockdown period, the emission of BC and other co-pollutants decreased significantly, yet they recovered as partial opening implemented. A large part of the planet experiences cold temperatures and frozen participation every year, and it is important to implement an air quality management system, which considers the effects of the cold

climate urban sites. The emission reduction of airborne BC and selected co-pollutants in the airports and surrounding areas, which may pose threat to the health of airport workers and residents should be tailored to different urban climates. Future research on BC sources, physicochemical characteristics at different environmental conditions are recommended. Ice nucleation microphysics of BC and interactions with brown carbon should also be further studied, to accurately evaluate the impact of BC in air quality, climate change and health research.

Data Availability Statement

Data of absorption coefficient and scattering coefficient have been published on Harvard Dataverse and can be downloaded at https://doi.org/10.7910/DVN/F63IB1. Data of $PM_{2.5}$, CO, O_3, NO_2 and NO can be found on NAPS website at https://data-donnees.ec.gc.ca/data/air/monitor/national-air-pollution-surveillance-naps-program/?lang=en, as well as the website of City of Montreal: http://ville.montreal.qc.ca/portal/page?_pageid=7237,74687650&_dad=portal&_schema=PORTAL

2.5 Acknowledgments

We would like to thank the following Canadian agencies for the financial support: Natural Science and Engineering Research Council of Canada (NSERC), Canada Foundation for Innovation (CFI) and Environment of Climate Change Canada (ECCC). We acknowledge David Liu at McGill University for assistance with S/TEM. We would like to thank Dr. Rordrigo Rangel-Alvardo and Mr. Devendra Pal for their comments, inputs, field logistics and their data sharing. We are grateful to Dr. Sonia Melancon, Dr. Farbrice Godefroy and Mr. Ryan Hall for information

of the instruments of NAPS, and Mr. Hall for his time for careful proofreading of this manuscript. We gratefully acknowledge the NOAA Air Resources Laboratory (ARL) for the provision of the HYSPLIT transport and dispersion model and/or READY website (https://www.ready.noaa.gov) used in this publication.

Chapter 3 Seasonal Trend of Black Carbon and Brown Carbon in Montreal: Impacts of Canada Record-Breaking Wildfires in Summer 2023

We have evaluated the concentration of BC in urban regions, especially during wintertime. Here we present the variations of not only BC but also BrC to comprehensively evaluate the impacts of LACs as an entity. In addition, as discussed in Chapter 1, fossil fuel combustion and biomass burning are the two major sources of LACs. In Chapter 2, we covered anthropogenic sources (fossil fuel combustion) of BC in urban regions. In this Chapter, we are going to present the huge impacts from a type of biomass burning, wildfires, which bring a large amount of BC and BrC. We will also demonstrate the light absorption of BC and BrC, showing how BrC can play an essential role in light absorption at short wavelengths.

Contribution of Authors

I co-designed the studies, conducted the sampling and the experiments, analyzed the data, interpreted the results, prepared the figures, and wrote the original manuscript. I am the first author of this original article.

Dr. Devendra Pal performed HYSPLIT back-trajectory analysis, prepared the cluster analysis plots and wind rose plots, participated in interpreting results and discussions, provided insights into experiments, and edited the article.

Professor Parisa A. Ariya (supervisor) co-authored this paper and is the corresponding author. She provided continuous guidance and support, co-designed the studies, participated in interpreting results and discussions, provided insights into experiments, and edited the article.

This chapter consists of a manuscript submitted Environmental Science & Technology

Seasonal Trend of Black Carbon and Brown Carbon in Montreal: Impacts of Canada Record-Breaking Wildfires in Summer 2023

Houjie Li[1], Devendra Pal[2], Parisa A. Ariya[1,2]

[1]Department of Chemistry, McGill University, Montreal, H3A0B8, Canada

[2]Department of Atmospheric and Oceanic Sciences, McGill University, Montreal, H3A0B9, Canada

Correspondence to: Parisa A. Ariya (parisa.ariya@mcgill.ca)

Keywords: black carbon; brown carbon; wildfire; light-absorbing carbonaceous particles; climate change; air pollution.

Synopsis: Wildfires are thought to be more frequent and more severe due to climate change. This research focuses on the additional emission of black and brown carbon due to record-breaking wildfires in northern Canada in 2023 and their impacts on the metropolitan of Montreal with implications for human health.

Abstract

Light-absorbing carbonaceous particles (LACs), including black carbon (BC) and brown carbon (BrC), are crucial components of air pollution and climate change. This study presents one year of observational data on BC mass concentration, B_{abs} (370), B_{abs} (870), and B_{scat} from July 2022 to July 2023. We analyzed seasonal trends in BC and BrC in an urban area Montreal and conducted a detailed case study of 2023 summer wildfires. Our results reveal that wildfire smoke significantly contributed to a large proportion of primary BrC and secondary BrC precursors by

combining the datasets of $PM_{2.5}$ and CO from MERRA-2 reanalysis data and back-trajectory analysis. Although most of the time, fossil fuel combustion is the primary source of BC and BrC in urban regions, when biomass burning became the predominant source of LACs, BrC may contribute more to light absorption at short wavelengths as BrC accounts for more than 50% of total light absorption at 370 nm, with primary BrC accounting for 70 ~ 80 % and secondary BrC accounting for 20 ~ 30%. Wildfires increased the BC mass concentration by over 26% and caused a significant rise in $PM_{2.5}$ by more than 300%. During the wildfire events, the daily average concentration of $PM_{2.5}$ exceeded the WHO guidance limits. As climate change will likely increase wildfire frequency and intensity, the affected cities need solid and resilient air quality plans to mitigate human exposure.

3.1 Introduction

Light-absorbing carbonaceous particles (LACs) have drawn growing interest in the past decades because they are one of the most critical radiatively active components in the atmosphere (IPCC 2013; Liu et al., 2020). LACs include black carbon (BC) and light-absorbing organic carbon, or so-called “brown carbon” (BrC), which can absorb solar radiation and warm the climate. BC strongly absorbs light from UV to near-infrared wavelengths, whereas BrC demonstrates strong wavelength dependence. The light absorption of BrC sharply decreases with the wavelength increases from UV to visible light. In addition to directly affecting the climate by absorbing solar radiation, LACs could impact the climate indirectly by serving as cloud condensation nuclei and ice nuclei, leading to either warming or cooling effects in the atmosphere, which is one of the sources of uncertainty in simulating the total impacts of LACs in climate models (Bond et al., 2013).

BC and BrC originate from both sources: anthropogenic sources, such as vehicles, industries and agricultural burning, and natural sources, including wildfires and volcanos (Bond et al., 2013). BC particles are mainly emitted from incomplete combustion of fossil fuels and biomass burning (Bond et al., 2013), with anthropogenic sources being predominant in urban areas (Li & Ariya, 2021; Liu et al., 2021; Meng et al., 2023). Meanwhile for BrC, the sources are more varied. The primary and predominant source of BrC emission is biomass burning, such as wildfires. Yet BrC can also be formed by aging processes in the atmosphere, such as heterogeneous and photochemical reactions. Some organic aerosols which are originally colorless and scatters light would undergo reactions with other components such as NO_x, O_3 or NH_3 to form chromophore function groups, becoming BrC in the end (Laskin et al., 2015). Additionally, aging processes would transform BrC into colorless organic carbon by photobleaching (Laskin et al., 2015). The diverse sources and transformation processes lead to complex matrices of BrC components in the atmosphere and make it challenge to simulate the fate and impacts of BrC in the atmosphere.

The health concerns caused by LACs have been widely reported. For example, long-term exposure to BC could lead to chronic kidney disease (Zhang et al., 2023), obesity (Yang et al., 2023) and cardiovascular disease (Wen et al., 2023). Moreover, Rasking et al. (2023) reported that ambient BC reached the kidney after inhalation and circulation in the body, which might exert adverse effects on kidney function. Liu et al. (2023) detected BC in eye-washed fluid, revealing the ocular exposure risk. Meanwhile, for BrC, the health impacts are usually reported with specific components like PAHs (Sedlacek et al., 2022). Due to the health concerns caused by BC, WHO has published new guidelines for air quality and proposed to make systematic measurements of BC to complement current $PM_{2.5}$ measurements in urban areas (WHO 2021). However, continuous real-time measurements of BrC are much more difficult because of the complexity of BrC

components. Although aerosol mass spectrometer (AMS) has been utilized for online measurement of organic aerosols, including BrC (Jiang et al., 2023; Lei et al., 2023; Tasoglou et al., 2020; Zhong et al., 2023), the high cost of the instrument makes it hard to use AMS for long-time continuous measurements prevalently. Developing a stable and low-cost commercial instrument for BrC is still challenging but necessary.

Wildfires, as a format of biomass burning, can be an essential source of LACs, organic aerosols, and other air pollutants, including $PM_{2.5}$, O_3, NO_x, and CO, which not only deteriorate local air quality and visibility but also undergo long-range transport to affect areas far from the sources. For example, the smoke produced by wildfires in Quebec, Canada, reached New York City in the US after long-range transport, causing severe air pollution in June 2023 (CNN 2023). This "record-breaking" wildfire event, during which 4.5 million hectares of forest burned, including 1.1 million in inhabited areas. Megacities such as Montreal suffered severe air pollution problems due to the forest-burning events from several hundred kilometres away. The occurrence of wildfires in the world is estimated to increase gradually due to climate change (Eck et al., 2023; Jolly et al., 2015; Xu et al., 2023). It is necessary to research how the combination of wildfire emissions and local anthropogenic emissions affect cities to systematically evaluate the impacts of BC and BrC in urban areas.

This study provides a year-long continuous measurements on LACs in Montreal, Canada, focusing on the summer of 2023, when most wildfires occurred. By combining the datasets of $PM_{2.5}$ and CO acquired from MERRA-2 reanalysis data and performing cluster back-trajectory analysis, we elucidate local and wildfire-induced BC and BrC concentrations.

3.2 Methods

3.2.1 Photoacoustic Extintiometer (PAX)

A PAX (Droplet Measurement Technologies (DMT), Inc., US) with an 870 nm laser module was used to continuously measure the scattering coefficient (B_{scat}) and absorption coefficient (B_{abs}) of ambient air. Generally, PAX draws air samples into the measurement chamber with a 1 L/min flow rate by an internal vacuum pump. The airflow will be split into the reciprocal nephelometer and the photoacoustic cell to measure B_{scat} and B_{abs} simultaneously. The absorption measurement uses in-situ photoacoustic technology and assumes that only BC particles can absorb the laser at 870 nm. Then, BC particles will transfer heat to the surrounding air, generating pressure waves that can be detected by a sensitive microphone attached to the chamber to calculate B_{abs} in one-second resolution. Meanwhile, the nephelometer can measure B_{scat} and respond to all aerosols regardless of size, morphology, and chemical compositions. A more detailed description can be found in the user manual of PAX provided by DMT (DMT 2020). The B_{scat} and B_{abs} data reported in this manuscript are hourly averaged. The absorption coefficients from PAX were reported as B_{abs} (870) to distinguish the data obtained from the aethalometer described below.

3.2.2 Aethalometer (AE43)

A seven-wavelength aethalometer (AE43) was used to measure ambient BC mass concentration and absorption coefficients B_{abs}. AE43 continuously measures light attenuation of aerosol samples at wavelengths of 370, 470, 520, 590, 660, 880 and 950 nm by drawing aerosols to deposit on the quartz filter tape. AE43 reports BC mass concentration in one-minute resolution with the data obtained at 880 nm wavelength because BC is assumed to be the only light absorber

at 880nm. The data at the other wavelengths were used for source appointment by calculating the absorption Ångstrom exponent (AAE). Since Drinovec et al. (2015) adopted "DualSpot" measurement method for Model AE33 and AE43 to compensate the filter scattering effect and the loading effect, the absorption coefficients at 7 wavelengths are assumed to be in-situ B_{abs}. Thus, the absorption coefficient of BrC ($B_{abs}(\lambda)_{BrC}$) at wavelength of λ can be acquired by the Equations (1) to (3):

$$B_{abs}\,(880) = BC\ Mass\ Concetration \times MAC(880) \quad (1)$$

$$B_{abs}(\lambda) = B_{abs}(\lambda)_{BC} + B_{abs}(\lambda)_{BrC} \quad (2)$$

$$\frac{B_{abs}(\lambda)_{BC}}{B_{abs}\,(880)} = \left(\frac{\lambda}{880}\right)^{-AAE_{BC}} \quad (3)$$

where B_{abs} (λ) is the total absorption coefficient at λ, and MAC (880) is BC mass absorption cross-section at 880 nm. AAE_{BC} is assumed to be 1. In this work, B_{abs} (370) is used as an indicator of BrC. Whereas AAE values were calculate based on Equation (4):

$$AAE\ (470/950) = \frac{ln[B_{abs}(470)/B_{abs}(950)]}{ln(950/470)} \quad (4)$$

BC mass concentration, B_{abs} (370) and AAE values were calculated into hourly averages for further analysis.

For the source appointment method based on aethalometer (Magee Scientific 2021), the following equations were used:

$$\frac{B_{abs}(470)_{ff}}{B_{abs}(950)_{ff}} = \left(\frac{470}{950}\right)^{-AAE_{ff}} \quad (5)$$

$$\frac{B_{abs}(470)_{bb}}{B_{abs}(950)_{bb}} = \left(\frac{470}{950}\right)^{-AAE_{bb}} \quad (6)$$

$$B_{abs}(470) = B_{abs}(470)_{ff} + B_{abs}(470)_{bb} \quad (7)$$

$$B_{abs}(950) = B_{abs}(950)_{ff} + B_{abs}(950)_{bb} \quad (8)$$

$$BB(\%) = \frac{B_{abs}(950)_{bb}}{B_{abs}(950)} \quad (9)$$

where AAE_{ff} is 0.9 and AAE_{bb} is 1.68 (Lepisto et al., 2023; Zotter et al., 2017), which are different from the values used in the instrument. The case when the value of BB% is larger than 50% is considered as biomass burning (BB) dominated, whereas when BB% is smaller than 50%, it is fossil fuel combustion (FF) dominated.

To separate the contribution of secondary BrC from total absorption coefficient, the minimum R-square (MRS) method was applied (Wang et al., 2019; Wu et al., 2018; Wu et al., 2023). Thus, absorption coefficients from secondary BrC can be acquired by combing Equation (10) to (13):

$$B_{abs}(\lambda) = B_{abs}(\lambda)_{pri} + B_{abs}(\lambda)_{sec} = B_{abs}(\lambda)_{pri} + B_{abs}(\lambda)_{BrC,sec} \quad (10)$$

$$B_{abs}(\lambda)_{pri} = B_{abs}(\lambda)_{BC} + B_{abs}(\lambda)_{BrC,pri} \quad (11)$$

$$B_{abs}(\lambda)_{BrC} = B_{abs}(\lambda)_{BrC,pri} + B_{abs}(\lambda)_{BrC,sec} \quad (12)$$

$$B_{abs}(\lambda)_{BrC,sec} = B_{abs}(\lambda) - B_{abs}(\lambda)_{pri} = B_{abs}(\lambda) - \left(\frac{B_{abs}(\lambda)}{BC}\right)_{pri} \times [BC] \quad (13)$$

where [BC] is BC mass concentration, and $(B_{abs}(\lambda)/BC)_{pri}$ is the ratio of absorption coefficient of primary particles to BC mass concentration from primary sources. If the value of $B_{abs}(\lambda)_{BrC,\,sec}$ is less than zero, the contribution from secondary BrC is considered as zero. The primary sources here are considered as combustion sources. The non-combustion primary sources of BrC are

biogenic sources, but biogenic primary BrC has weak absorption (Peng et al., 2016; Perrino &Marcovecchio, 2016), which means the absorption of biogenic primary BrC is negligible.

3.2.3 Electron Microscopy

A Micro Orifice Uniform Deposit Impactor (MOUDI, model 100-R, MSP Corp., Shoreview, MN, USA) with an inlet flowrate of 30 L/min was used to collect aerosol samples on quartz fibre filters with transmission electron microscopy (TEM) grids attached for 12 hours. A Thermo Scientific Talos F200X G2 (S)TEM with X-FEG High Brightness Schottky Field Emission Source and Ceta 16M 4k x 4k CMOS Camera was used to analyse the size, morphology, and chemical composition of aerosol samples. A FEI Quanta 450 Environmental Scanning Electron Microscope (FE-ESEM) with EDAX Octane Super 60 mm2 SDD and TEAM EDS Analysis System was used to provide more morphology information in 3 dimensions.

3.2.4 The Hybrid Single-Particle Lagrangian Integrated Trajectory (HYSPLIT) Model

The registered desktop version of the HYSPLIT model from the Air Resources Laboratory (ARL) (Stain et al, 2015; Rolph et al, 2017) was used to analyze the origin of air masses and establish source-receptor relationships through back-trajectory analysis. Our investigation focused on estimating air mass movement through integrated trajectory clustering, particularly during June and July of 2022-2023, which coincided with the forest fire season in Quebec, and the month of October from 2021-2023 in Montreal (45°30'17.070" N, 73°34'45.000" W). The cluster analysis enabled us to examine the percentage of air mass back-trajectories reaching the study area, providing insights into long-range transport pollution source regions. The total number of back-

trajectories observed for each case study were as follows: 116 in June, 125 in July, and 121 in October, with trajectories occurring at four different times per day (00 Z, 06 Z, 12 Z, and 18 Z), resulting in four trajectories per day. During each season, 2-day back-trajectories from HYSPLIT were generated at a fixed atmospheric height of 5 km. Clustering of 24-hour trajectories was performed using a 30 percent change criterion, resulting in 20 hours of back-trajectory results per cluster. To maintain consistency in the analysis, approximately four clusters were displayed. Our observations revealed very distinct air mass movements, with more stagnant air masses observed during October 2022.

3.2.5 Ancillary data

The hourly averages of $PM_{2.5}$, O_3, and CO were acquired from the MERRA-2 reanalysis data (GMAO 2015a, 2015b). Since the resolution of MERRA-2 is 0.5° × 0.625°, the concentrations of $PM_{2.5}$, CO, and O_3 at 45.5° N, 73.750° W were selected to compare with B_{abs} and B_{scat}. The hourly averages of temperature (T) and relative humidity (RH) were acquired from the meteorological station at the downtown campus of McGill University (45°30'17.070" N, 73°34'45.000" W) conducted by the Environment and Climate Change Canada (ECCC) which is about 400 meters away from our sampling site (45° 30' 17.449” N, 73° 34' 26.555” W).

3.3 Results and Discussion

3.3.1 Seasonal Trend of BC and BrC Emissions in Montreal

Montreal is a cold climate city that receives about 2.1 m of snow yearly. According to the ECCC, a year in Montreal is divided into winter (December 1st to April 20th), spring (April 21st to June 20th), summer (June 21st to September 20th), and fall (September 21st to November 30th). In

this work, Spring 2023 spans from April 21st to May 31st. June and July 2023 are considered wildfire months and will be discussed separately.

Fig. 3.1 and 3.2 display variations of BC mass concentration, B_{abs} (370), B_{abs} (870), and B_{scat} during July 2022 to July 2023. BC mass concentration reached the peak value (0.33 ± 0.30 μg/m^3) in October 2022, instead of the wildfire-affected month, i.e. June 2023 (0.27 ± 0.25 μg/m^3) (Table 3.1). Considering the possible bias due to noncontinuous sampling of AE43, B_{abs} (870) was used to compare with BC mass concentration (Fig. 3.2). And the result shows that the variation of B_{abs} (870) was consistent with BC mass concentration for most of time. B_{abs} (870) followed a similar trend, with a peak value (2.19 ± 2.76 Mm^{-1}) in October 2022, compared to 1.47 ± 1.77 Mm^{-1} in June 2023 (Table B1). However, the main discrepancy between BC mass concentration and B_{abs} (870) appeared during December to April, the winter. The variation of B_{abs} (870) demonstrated a similar seasonal trend described in Li et al. (2021) that BC maintained a relatively high concentration during the long winter, which was not observed by AE43. One possible reason is that a $PM_{2.5}$ cyclone inlet was attached to AE43 which constrained the size of particles sampled by AE43, whereas PAX had no such a restriction. It is also likely that AE43 did not sample as many days as PAX did, which brought sampling bias, causing the overestimation of BC mass concentration among Summer and Fall 2022. It is noteworthy that both BC mass concentration and B_{abs} (870) can only demonstrate the variation of BC. The contribution of BrC was not included in these variables. Instead, the largest values of B_{abs} (370) and B_{scat} which include the contribution from both BC and BrC, are 9.18 ± 16.30 Mm^{-1} and 20.52 ± 38.39 Mm^{-1} respectively (Fig. B1, Table 3.1, Table B1), in June 2023 when the record-breaking wildfires took place in north Quebec. The high BC mass concentration in October 2022 may be attributed to local emission sources as suggested by wind pattern analysis. Monthly cluster analysis was performed to identify the wind

pattern at Montreal (Fig. B2) which shows that stagnant local air mass accounts for about 62% in October 2022, larger than its proportion in 2021 (46%) and 2023 (34%). This result suggests that the high BC mass concentration was associated with local emission sources. AAE (470/950) increased from summer of 2022 to winter, and then decreased after the winter, indicating the proportion of BrC gradually increased until the winter. However, AAE (470/950) remained between 1.2 and 1.4, suggesting BC still contributed significantly to light absorption.

Fig. 3.3 and Fig B2 show the diurnal variation of BC mass concentration, B_{abs} (370) and B_{abs} (870) in different seasons and wildfire months. No matter which season, the significant impact of anthropogenic sources in urban areas can be reflected by the clear "rush-hour" peak at around 8 am. The concentration of BC (and probably BrC) reached its maximum at 8 am due to transportation to workplaces. Then, with the development of the planetary boundary layer during daytime, along with less traffic, the concentration of BC was diluted, leading to the decline until evening. BrC, influenced by photochemical reactions and photobleaching, shows more complex diurnal behavior, which can be indicated by B_{abs} (370). Additionally, BrC could also be reduced through photobleaching processes, causing the decrement of B_{abs} (370). The results of these effects are present in the end as B_{abs} (370) decreases until evening. BC mass concentration and B_{abs} (370) increased again during nighttime (10 pm to 5 am) because the planetary boundary layer became lower at night, concentrating BC and BrC particles in the air. Furthermore, BrC could be generated by heterogenous reactions from BrC precursors (Huang et al., 2021), which could contribute to the increment of B_{abs} (370).

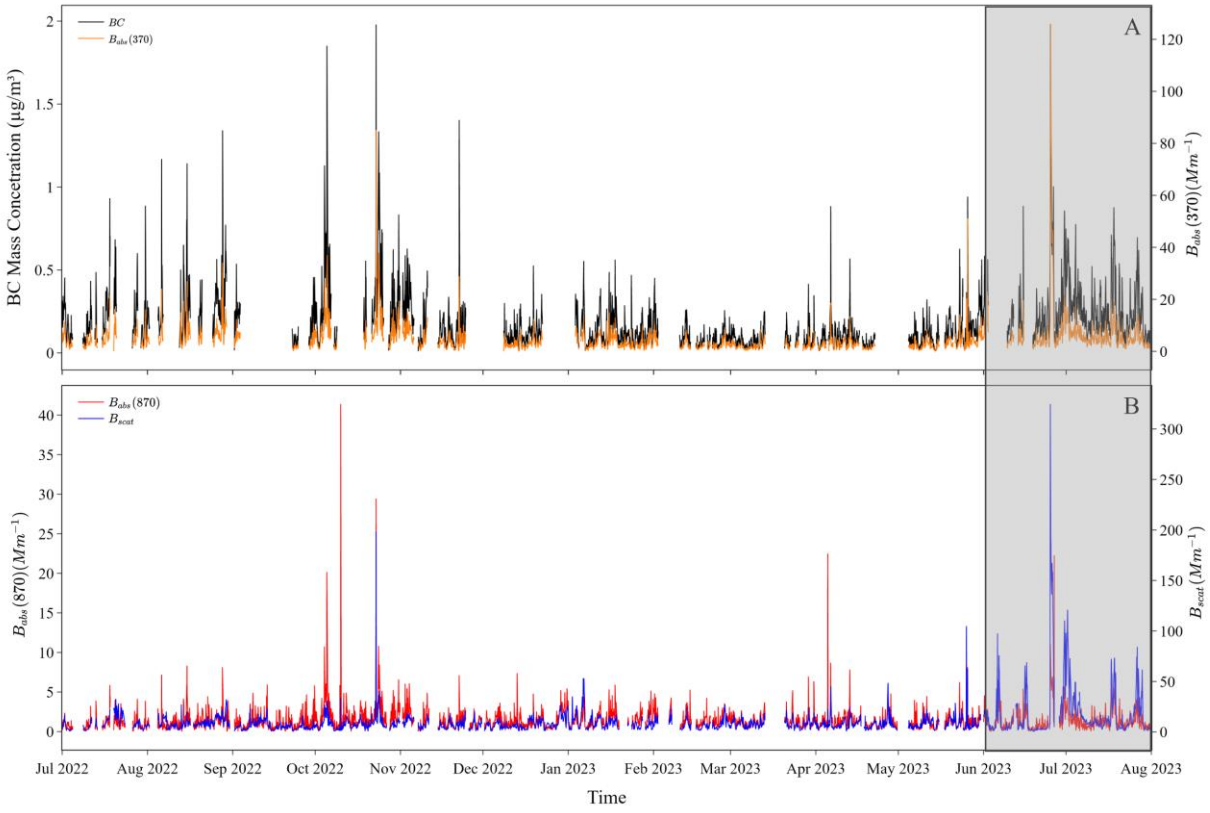

Figure 3.1. Time series hourly averages of (A) BC mass concentration and B_{abs} (370), (B) B_{abs} (870) and B_{scat}. The shadow area indicates the wildfire months (June and July) in 2023.

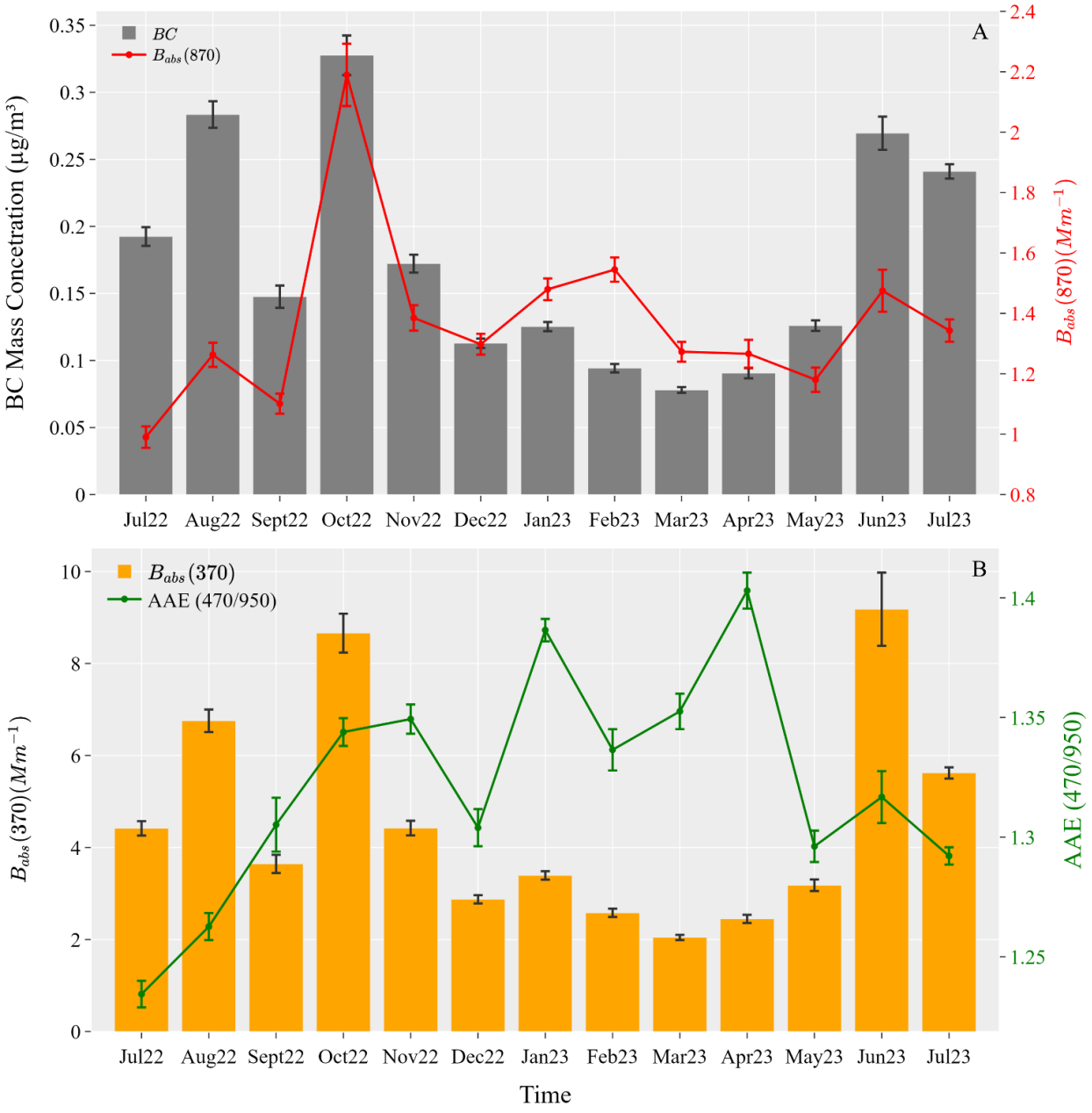

Figure 3.2. Monthly averages of (A) BC mass concentration and B_{abs} (870), (B) B_{abs} (370) and AAE (470/950). The error bars indicate the standard errors for BC mass concentration, B_{abs} (870), and B_{abs} (370) respectively for each month.

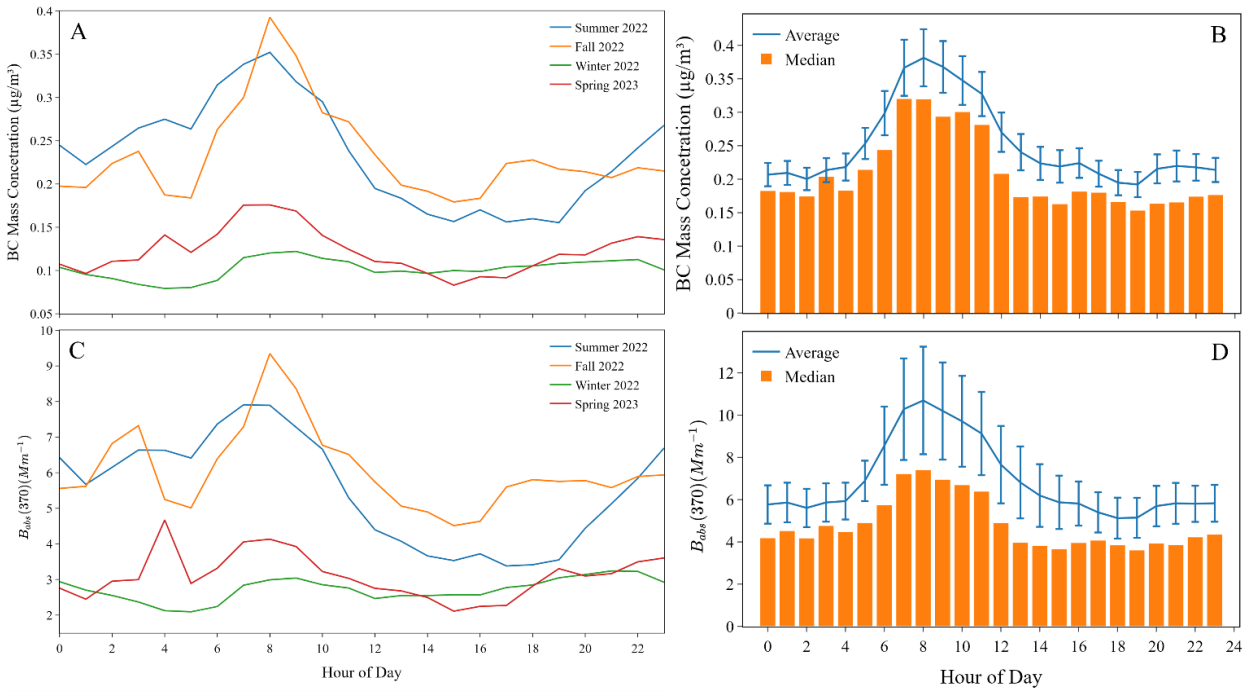

Figure 3.3. Diurnal variation of BC mass concentration (Panels A, B) and B_{abs} (370) (Panels C, D) in different seasons. Panels C and D indicate the wildfire months (June and July 2023), and the error bars on blue lines represent the standard errors.

Table 3.1. Statistic description of monthly variation of BC mass concentration and B_{abs} (370) from 2022 to 2023. "Mean" is the arithmetic average. "Std" is the standard deviation. "25%" and "75%" represent quantile values.

	BC Mass Concentration (μg/m³)						
Month	**Mean**	**Std**	**Min**	**25%**	**Median**	**75%**	**Max**
Jul-22	0.19	0.14	0.03	0.09	0.15	0.26	0.93
Aug-22	0.28	0.18	0.03	0.17	0.25	0.35	1.34
Sep-22	0.15	0.11	0.01	0.06	0.11	0.23	0.54
Oct-22	0.33	0.30	0.01	0.15	0.24	0.42	1.98
Nov-22	0.17	0.14	0.01	0.07	0.14	0.24	1.40
Dec-22	0.11	0.07	0.01	0.07	0.10	0.14	0.53
Jan-23	0.13	0.09	0.01	0.06	0.10	0.17	0.56
Feb-23	0.09	0.06	0.02	0.05	0.08	0.12	0.45
Mar-23	0.08	0.05	0.02	0.04	0.07	0.10	0.42
Apr-23	0.09	0.08	0.01	0.05	0.07	0.12	0.88
May-23	0.13	0.10	0.01	0.06	0.11	0.16	0.94
Jun-23	0.27	0.25	0.03	0.13	0.18	0.30	1.98
Jul-23	0.24	0.15	0.03	0.14	0.21	0.31	0.88
	B_{abs} (370) (Mm^{-1})						

Month	Mean	Std	Min	25%	Median	75%	Max
Jul-22	4.42	3.10	0.71	2.16	3.61	6.04	21.48
Aug-22	6.75	4.38	1.00	3.97	5.79	8.10	34.14
Sep-22	3.64	2.53	0.19	1.60	2.66	5.46	12.50
Oct-22	8.66	8.49	0.49	4.10	6.58	10.57	85.19
Nov-22	4.42	3.28	0.22	1.93	3.61	6.20	28.81
Dec-22	2.87	1.66	0.09	1.78	2.51	3.61	12.46
Jan-23	3.39	2.37	0.15	1.60	2.66	4.79	15.05
Feb-23	2.58	1.81	0.44	1.31	2.05	3.19	10.58
Mar-23	2.05	1.27	0.26	1.16	1.80	2.65	9.48
Apr-23	2.45	1.93	0.36	1.16	2.06	3.25	18.69
May-23	3.18	3.06	0.26	1.46	2.55	4.18	51.16
Jun-23	9.18	16.30	0.68	3.07	4.46	7.53	125.91
Jul-23	5.62	3.34	0.81	3.29	4.81	7.18	19.01

3.3.2 Case Study: Quebec Wildfire Events during Summer 2023

The wildfires in Canada during the summer of 2023 have been widely reported as record-breaking (CWFIS 2023). Since May 2023, wildfires occurred more than 400 times, burning more than 3.8 million-hectare areas in Quebec, Canada, breaking the record of the past ten years (Table B2, acquired from SOPFEU 2024). The wildfire smoke caused severe haze in New York City in early June after long-range transport from north Quebec (CNN2023; Fig. B4). The City of Montreal is one of Canada's most significant metropolitan areas, located between north Quebec and New York City. Although burning regions were far away from Montreal, and Montreal was not affected by wildfires directly, like New York, smoke emitted by wildfires underwent long-range transport, reaching Montreal and leading to severe air pollution during the summer of 2023. The cluster back-trajectory analysis was also performed for June and July 2023 (Fig. B5 A and B), showing that in June 2023, about 44% of air masses came from the north, which brought a large amount of smoke. Although this number reduced to about 18% in July 2023, much less than June, the smoke from the north still led to severe air pollution in Montreal, compared with July 2022. Further wind rose data suggested that the Montreal becomes centre and mixed air coming from

both northern Quebec along with Ontario, Canada and New York State, US, affecting the Montreal air quality and enhancing the BC and BrC concentrations (Fig. B5 C).

3.3.2.1 Observation of wildfire impacts on urban areas

Figure 3.4 shows that BC mass concentration and B_{abs} (370) reached the highest values from June 25th to June 26th, where BC mass concentration was 1.98 μg/m^3 and B_{abs} (370) was 125.91 Mm^{-1}. The back-trajectory analysis confirmed that it was caused by the smoke from north Quebec, where wildfires had taken place (Fig. B6). Then, in July 2023, BC mass concentration maintained relatively high values compared with the previous months, with a maximum concentration of 0.88 μg/m^3, much lower than the maximum in June. Both coefficients from PAX indicate July 2023 was impacted by wildfires longer than June 2023, which elevated the monthly average in July. Considering possible bias from those missing days in June, B_{abs} (870) and B_{scat} from PAX measurement could be regarded as a reference when comparing monthly averages.

Temperature and RH did not demonstrate noticeable changes in the variation patterns, which indicates that regional climate can hardly contribute to the high BC and BrC values (Fig. 3.4). In addition, although the concentrations of $PM_{2.5}$ and CO are acquired from MERRA-2 reanalysis data, the variation of $PM_{2.5}$ is in accord with the variation of BC mass concentration and B_{abs} (370). Yet CO did not show a similar variation with $PM_{2.5}$. Since CO is regarded as a tracer of local anthropogenic pollution in urban regions, the sharp increments in BC, B_{abs} (370) and $PM_{2.5}$ during these two months should be attributed to the smoke emitted by wildfires in north Quebec.

To further demonstrate the significant impact of wildfires, July 2022 was chosen to compare with July 2023. June 2022 was not included because AE43 was received and installed by the end of June 2022. Furthermore, as is shown in Table B2, 2022 was least affected by wildfires

among the last 5 years. Thus, the measurements in July 2022 could present the concentrations of BC, BrC, and $PM_{2.5}$ from urban anthropogenic sources, with less influence from wildfires. The average BC mass concentration in July 2022 was 0.19 $\mu g/m^3$ but increased to 0.24 $\mu g/m^3$ in July 2023. The increment was more than 26%. And for B_{abs} (370), the increment was over 27%, increasing from 4.42 Mm^{-1} to 5.62 Mm^{-1} (Table 3.1). As a reference, B_{abs} (870) was 0.99 Mm^{-1} in July 2022 but became 1.34 Mm^{-1} in July 2023. The increment was more than 35% (Table B1).

Although BC mass concentration and B_{abs} (370) were not available for June 2022, it can be speculated that the increment of BC mass concentration in June would not be less than that in July as B_{abs} (870) increased from 1.08 Mm^{-1} in July 2022 to 1.47 Mm^{-1} in July 2023, more than 36%. Since it is usually assumed that BC is the only component which absorbs radiation with 870 nm wavelength, and the contribution to B_{abs} (370) from BrC is compatible with BC, the increment of B_{abs} (370) cannot be reflected by B_{abs} (870). However, B_{scat} may give a hint to that. B_{scat} was 4.63 Mm^{-1} (June) and 8.38 Mm^{-1} (July) in 2022. These numbers sharply increased to 20.52 Mm^{-1} (June) and 18.54 Mm^{-1} (July) in 2023 (Table B1). The increment as high as 343% in June 2023 indicates that wildfire smoke brought a tremendous number of particles which include not only BC but also primary BrC, secondary BrC and probably secondary BrC precursors. This could be further supported by the variation of $PM_{2.5}$. The averages of $PM_{2.5}$, CO and O_3 in June and July during the past 10 years are summarized in Table B3. The variation of $PM_{2.5}$ shows the increment was about 349% in June and 74% in July when comparing 2023 with 2022 (Table B3). In contrast, whereas for the other years, the variations of $PM_{2.5}$ compared with 2022 were not as dramatically high as 2023. Table B3 confirms again that 2022 was the least impacted by wildfires in the past 5 years because the concentration of $PM_{2.5}$ was lowest, compared with 2019 to 2023. However, O_3 and CO did not show similar variations.

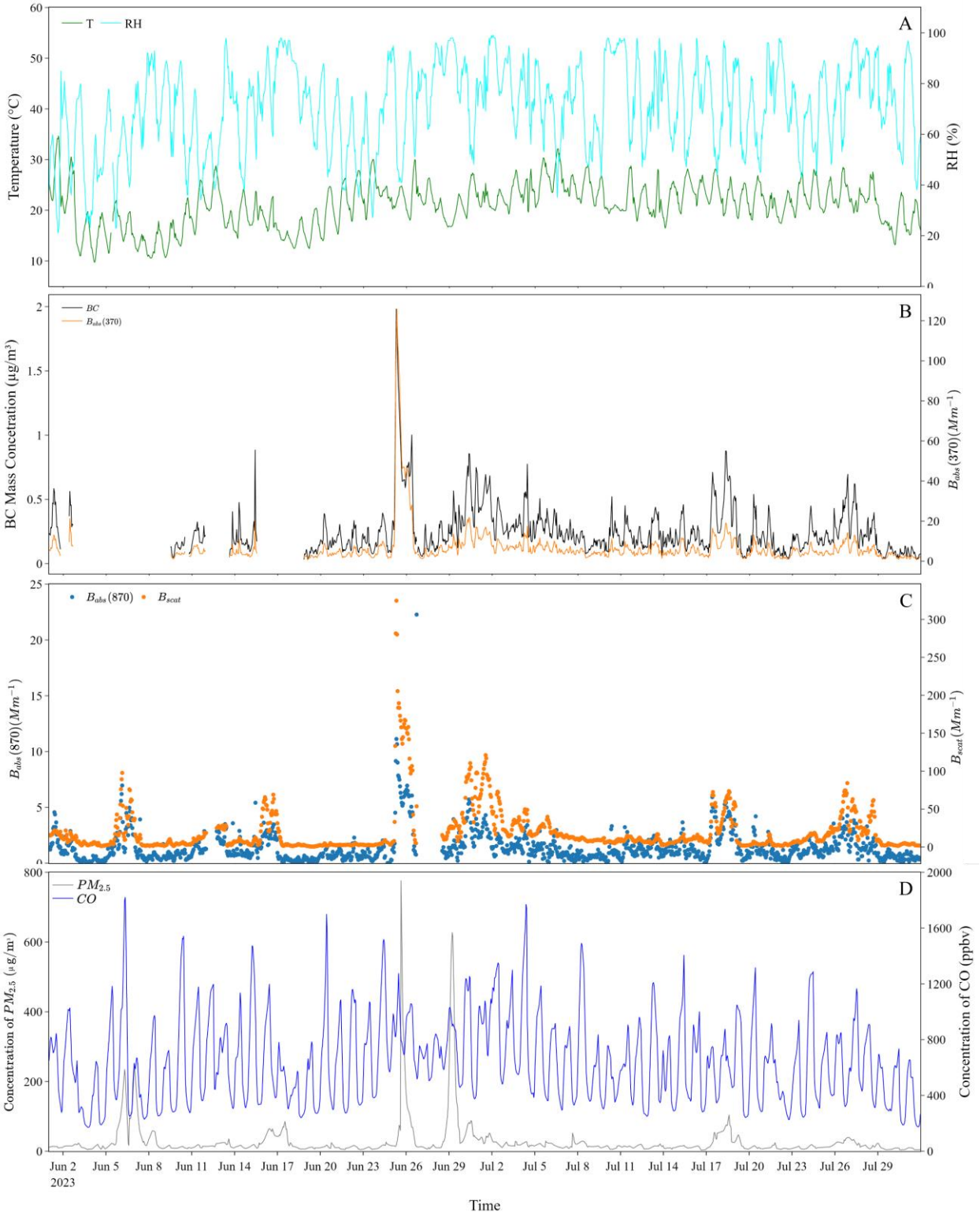

Figure 3.4. Hourly averages of (A) Temperature and RH, (B) BC mass concentration and B_{abs} (370), (C) B_{abs} (870) and B_{scat}, and (D) concentration of $PM_{2.5}$ and CO during June 1st, 2023, to July 31st, 2023.

3.3.2.2 Secondary BrC absorption and difference between fossil fuel combustion and biomass burning cases

To investigate the contribution of BrC (both primary and secondary BrC) to light absorption during the wildfire period, the MRS method mentioned in Section 3.2.2 was utilized to separate secondary BrC from primary BC and BrC. The result is shown in Fig. 3.5. Although BC is the predominant component of light absorption in most of days, it is obvious that during June 25th to 26th, when the impact from wildfire smokes was tremendous, the contribution from BrC was not negligible but as high as twice the BC absorption at 370 nm. This indicates the great potential of BrC emitted by wildfires to play a crucial role on absorption of short-wavelength radiation.

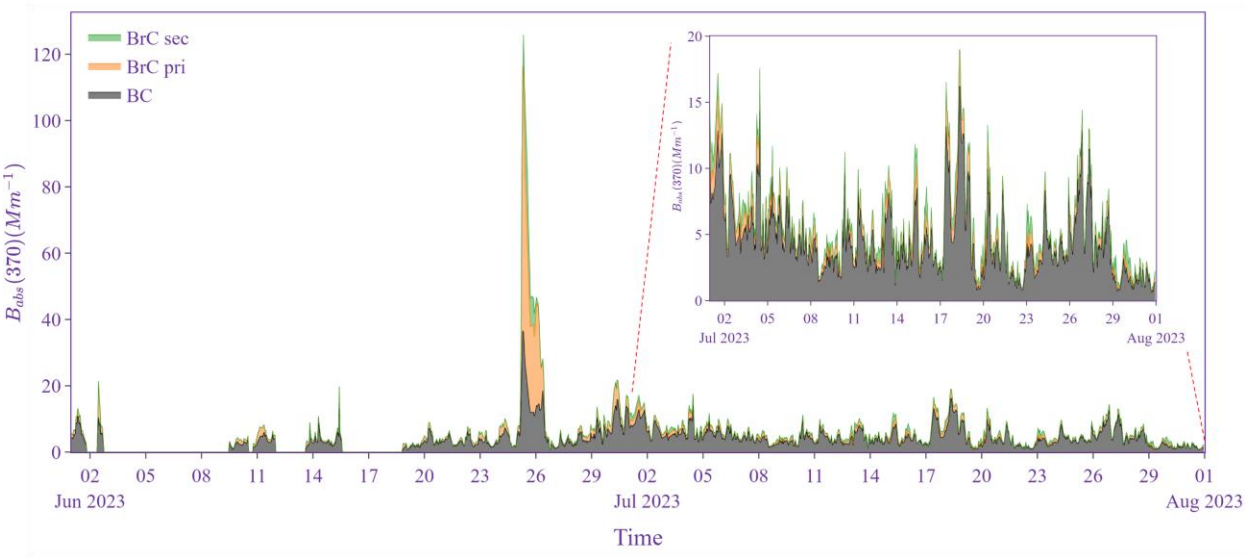

Figure 3.5. Hourly average absorption coefficients of BC, primary BrC (BrC pri), and secondary BrC (BrC sec) at 370 nm. The small figure on the top-right area shows the zoom-in plot of July 2023.

The hourly averages of B_{abs} (370) were then divided into FF-dominated cases (77%) and BB-dominated cases (23%) based on the method described in Section 3.2. Table 3.2 shows the summary of daytime and nighttime average absorption coefficients. For FF-dominated cases, BC accounts for 80% of B_{abs} (370), and there is no apparent difference between daytime and nighttime.

Primary BrC contributes to most of BrC absorption, indicating that very limited secondary BrC was formed. Yet for BB-dominated cases, the absorption of BrC became compatible with the absorption of BC, even more than BC. More interestingly, the formation of secondary BrC was promoted, especially during the daytime. It is widely known that photochemical reactions could lead to both photobleaching, reducing the absorption of BrC, and facilitating the formation of secondary BrC from BrC precursors, increasing its absorption of BrC (Laskin et al., 2015). Thus, one possible reason that $B_{abs,\ BrC\ sec}$ (370) could account for 25% of BrC absorption is that the formation of secondary BrC was more favoured during daytime for BB-dominated cases. Whereas during nighttime, heterogeneous reactions are possibly primary pathways to generate secondary BrC (Huang et al., 2021). However, this need to be further investigated once air pollutant data in 2023 are available from the City of Montreal.

Table 3.2. Daytime and nighttime averages (with unit of Mm^{-1}) of B_{abs} (370), $B_{abs,\ BC}$ (370), $B_{abs,\ BrC}$ (370), $B_{abs,\ BrC\ pri}$ (370), $B_{abs,\ BrC\ sec}$ (370), and $B_{abs,\ pri}$ (370) for all data, FF-dominated cases, and BB-dominated cases. The percentage values for $B_{abs,\ BC}$ (370) and $B_{abs,\ BrC}$ (370) indicate proportions of BC and BrC to B_{abs} (370) respectively. The percentage values for $B_{abs,\ BrC\ pri}$ (370), $B_{abs,\ BrC\ sec}$ (370) represent the proportions of primary BrC and secondary BrC to $B_{abs,\ BrC}$ (370) respectively. And the percentage values for $B_{abs,\ pri}$ (370) shows the contribution from primary sources.

		B_{abs} (370)	$B_{abs,\ BC}$ (370)	$B_{abs,\ BrC}$ (370)	$B_{abs,\ BrC\ pri}$ (370)	$B_{abs,\ BrC\ sec}$ (370)	$B_{abs,\ pri}$ (370)
Total	Day	7.41	4.99 (67%)	2.42 (33%)	1.99 (82%)	0.43 (18%)	6.98 (94%)
	Night	6.19	4.16 (67%)	2.03 (33%)	1.66 (81%)	0.37 (19%)	5.82 (94%)
FF	Day	5.78	4.70 (81%)	1.08 (19%)	1.01 (93%)	0.07 (7%)	5.71 (99%)
	Night	4.92	3.93 (80%)	0.99 (20%)	0.86 (87%)	0.13 (13%)	4.79 (97%)
BB	Day	15.64	6.42 (41%)	9.22 (59%)	6.96 (75%)	2.26 (25%)	13.38 (86%)
	Night	8.92	4.65 (52%)	4.27 (48%)	3.39 (79%)	0.88 (21%)	8.04 (90%)

Table 3.3 presents the wavelength dependence of light absorption of BC and BrC. BrC shows a strong wavelength dependence with the most significant contribution (33%) at 370 nm. And BrC still accounts for more than 10% absorption at 590 nm. The importance of BrC on light absorption could be better demonstrated if biomass burning is the predominate source of BrC (Fig.

3.6, Table B4). At 370 nm, the contribution from BrC can be more than 50%. Even at 660 nm, the proportion of BrC absorption is 10%. While for the FF-dominated case, BrC always accounts for less than 20% light absorption at all these wavelengths. This could be useful for future modelling work. When modelling the impacts of wildfires, the contribution from BrC could be treated as large as BC at short wavelengths. Whereas for fossil fuel combustion FF-dominated scenarios, such as urban areas in most of time, the contribution from BrC should be considered as less than 20% as suggested by previous research (Wu et al., 2023).

Fig. 3.7 depicts the typical morphology and EDS results of aerosol samples collected on Jun. 25th when B_{abs} (370) reached the highest value during the whole wildfire months. Fig. 3.7A shows the prevalent particles observed by TEM and SEM, which are nano-size spheres coated by organic matters to form micron-size particles. Fig. B7C and D prove that the thin coatings were organic matters. Under most circumstances, there was only one particle inside each coating. However, two or more particles in the same coating were also observed (Fig. B7A). The high abundance of potassium in the particles reveals that the source of the aerosol samples was biomass burning, i.e. wildfires in this manuscript. Fig. 3.7C demonstrates a micron-size tar ball, a known example of BrC particles, which contain mainly carbon, but the small proportions of nitrogen and oxygen (Fig. 3.7D) distinguish it from BC. All the tar balls observed by TEM were at micron sizes without any coating outside. Fig. 3.7E shows a chain-like BC aggregate. Fig. 3.7F confirms that the BC aggregate was mixed with some organic carbon and silicon. Besides, the SEM image demonstrates how BC particles could grow from spheres with diameters less than 50 nm to submicron-size aggregates shown in Fig. 3.7E to micron-size agglomerates (Fig. B7B).

Table 3.3. Averages (with unit of Mm^{-1}) of B_{abs} (λ), $B_{abs, BC}$ (λ), $B_{abs, BrC}$ (λ), $B_{abs, BrC\ pri}$ (λ), $B_{abs, BrC\ sec}$ (λ), and $B_{abs, pri}$ (λ) at different wavelengths. The percentage values for $B_{abs, BC}$ (λ) and $B_{abs, BrC}$ (λ) indicate proportions of BC and BrC to B_{abs} (λ) respectively. The percentage values for $B_{abs, BrC\ pri}$ (λ), $B_{abs, BrC\ sec}$ (λ)

represent the proportions of primary BrC and secondary BrC to $B_{abs, BrC}$ (λ) respectively. And the percentage values for $B_{abs, pri}$ (λ) shows the contribution from primary sources.

Wavelength	B_{abs} (λ)	$B_{abs, BC}$ (λ)	$B_{abs, BrC}$ (λ)	$B_{abs, BrC\ pri}$ (λ)	$B_{abs, BrC\ sec}$ (λ)	$B_{abs, pri}$ (λ)
370	6.90	4.64 (67%)	2.26 (33%)	1.85 (82%)	0.41 (18%)	6.49 (94%)
470	4.73	3.65 (77%)	1.08 (23%)	0.92 (85%)	0.16 (15%)	4.57 (97%)
520	3.96	3.30 (83%)	0.65 (17%)	0.56 (85%)	0.10 (15%)	3.86 (98%)
590	3.29	2.91 (89%)	0.38 (11%)	0.32 (85%)	0.06 (15%)	3.23 (98%)
660	2.75	2.59 (94%)	0.16 (6%)	0.13 (80%)	0.03 (20%)	2.72 (99%)

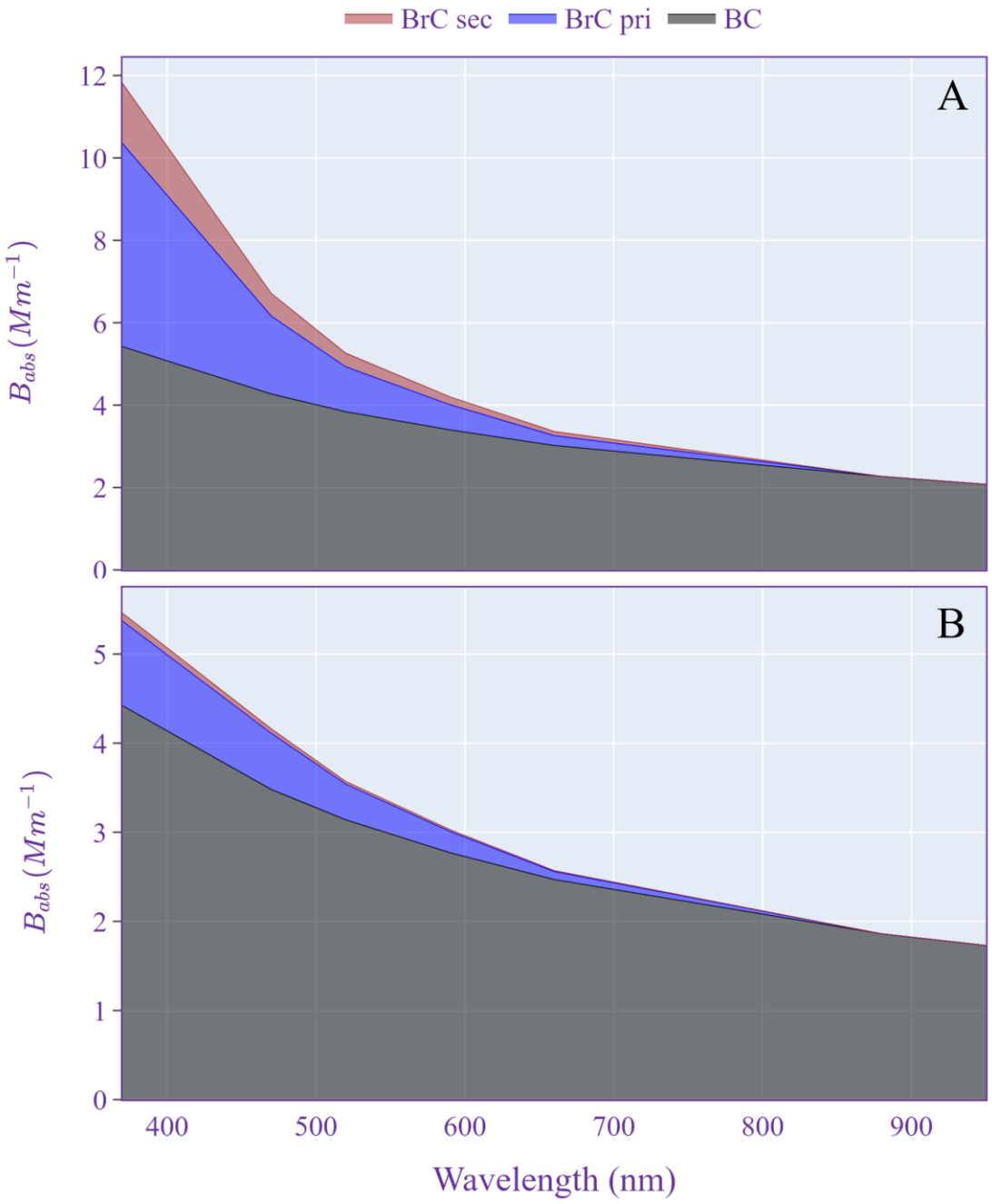

Figure 3.6. The proportion of BC, primary BrC (BrC pri), and secondary BrC (BrC sec) to absorption coefficients at seven wavelengths (370, 470, 520, 590, 660, 880, and 950 nm). Panel A shows the BB-dominated case, and Panel B shows the FF-dominated case.

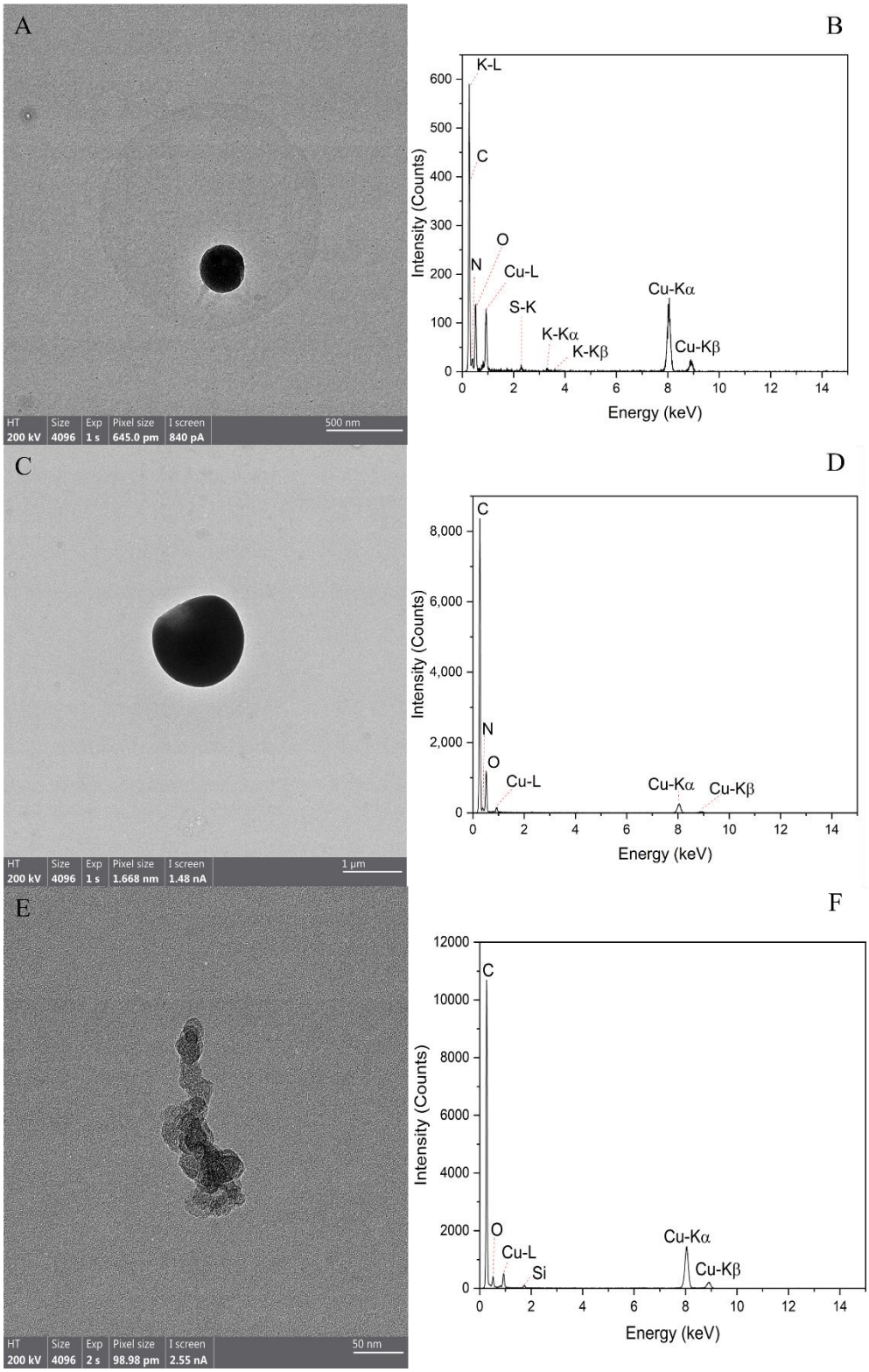

Figure 3.7. TEM images with corresponding EDS results of typical particles deposited on the grids. Panel B, D, and F indicate the EDS results of Panel A, C, and E, respectively.

3.4 Conclusion

This study presents over one-year observation data of LACs (BC and BrC) and their analysis in Montreal from Summer 2022 to Summer 2023, including the record-breaking wildfire events in Canada. We observed that BC in winter still demonstrated a high mass concentration, lasting during the long winter, consistent with previous research (Li & Ariya, 2021). We also presented an observation of LACs emitted by wildfires in Montreal, revealing, for the first time, how Canadian wildfires in the Summer of 2023 indirectly affected urban areas with ground-based observation. The significant wildfires in 2023 raised the BC mass concentration by more than 26% and caused a sharp increment of $PM_{2.5}$ by more than 300%. Besides, as an essential type of biomass burning, wildfires revealed the potential of how BrC could contribute to light absorption at short wavelengths as BrC could account for more than 50% total light absorption at 370 nm, with primary BrC accounting for 70% ~ 80% and secondary BrC accounting for 20% ~ 30%. As wildfires become more frequent and intense due to climate change, understanding BrC's role in light absorption and its broader impacts is crucial. Enhanced ground-based BrC observations and precise modeling are essential for comprehensive evaluation and policy adaptation.

Furthermore, snow is a ubiquitous feature of Canada and other Nordic countries, with meteorological winter lasting up to five months. This suggests that wildfire pollutants may travel long distances over frozen surfaces or deposit into the lithosphere, hydrosphere, biosphere, and cryosphere, interacting with the atmosphere (Ariya et al., 2018; Rangel-Alvaraz et al., 2019). Notably, there are record numbers of fires burning underneath the snow in some Canadian provinces (Alberta Wildfire 2024). Under the right conditions, these fires can re-emerge in the spring as wildfires and create additional sources of BC and BrC that can affect not only the vicinity

of the fires but also cities at long distances away, affecting human lives and damaging the ecosystem. Air quality policy should be updated for better adaptation to climate change.

Data availability

All the Data (PAX, AE43, MERRA-2) used in this work are uploaded to and available on Havard Dataverse: https://doi.org/10.7910/DVN/F63IB1.

Competing interests

The authors have declared no competing interests.

3.5 Acknowledgement

We thank the National Science and Engineering Research of Canada (NSERC), the Canadian Foundation for Innovation (CFI), and NSERC-PURE. We gratefully acknowledge the NOAA Air Resources Laboratory (ARL) for providing the HYSPLIT transport and dispersion model and/or READY website (https://www.ready.noaa.gov) used in this publication. We also thank Dr. David Liu at Facility for Electron Microscopy Research (FEMR), McGill University for helping us acquire EM images and EDS results.

Chapter 4 Using Machine Learning Model to Derive BC Mass Concentration Based on Common Air Pollutants

Although we have achieved continuous measurements on LACs in our laboratory, it is necessary to make the monitoring of LACs emissions more prevalent in a city so that researchers can better understand the impacts of LACs on local or regional climate and air quality. However, purchasing new instruments for measurement can be difficult for governments due to insufficient budgets. Thus, we developed a machine learning model to simulate the variation of BC in Montreal by using the concentrations of common air pollutants which are already continuously measured. This model could provide a feasible alternative to places where the information of BC is still rare. In the future work, we can even expand the usage of this model to estimate BrC emissions and source appointment if enough reliable data are available.

Contribution of Authors

I co-designed the studies, developed the code, analyzed the data, interpreted the results, prepared the figures, and wrote the original manuscript. I am the first author of this original manuscript.

Professor Parisa A. Ariya (supervisor) co-authored this manuscript and is the corresponding author. She provided continuous guidance and support, co-designed the studies, participated in interpreting results and discussions, and provided insights into data analysis.

The manuscript is currently in preparation.

Using Machine Learning Model to Derive BC Mass Concentration Based on Common Air Pollutants

Houjie Li[1], Parisa A. Ariya[1,2]

[1]Department of Chemistry, McGill University, Montreal, H3A0B8, Canada

[2]Department of Atmospheric and Oceanic Sciences, McGill University, Montreal, H3A0B9, Canada

Correspondence to: Parisa A. Ariya (parisa.ariya@mcgill.ca)

Abstract

BC has drawn great interest in the past decades because of its importance on climate change, air pollution and human health. The World Health Organization (WHO) has suggested monitoring BC mass concentration is necessary as a complement to current measurement of $PM_{2.5}$. However, purchasing new instruments for BC at each air quality monitoring station would require a large amount of budget, which makes it difficult to achieve. Thus, we developed a machine learning (ML) model based on recurrent neuron network (RNN) and long short-term memory (LSTM) algorithms which are good at capturing long term patterns and making more accurate predictions. We used the concentrations of common air pollutants (CO, NO_x, $PM_{2.5}$, and O_3) and time variables including "Day of Year", "Hour of Day", and "Day of Week" as inputs of the model, and the model achieved a relatively good performance on predicting BC mass concentrations.

4.1 Introduction

Black carbon is the by-product of incomplete combustion of fossil fuels and biomass burning. It is of increasing interest because of its essential role in climate change and air pollution. BC can strongly absorb solar radiation from UV to near infrared in the atmosphere, warming the climate. The climate forcing of BC is estimated to be +1.1 W/m^2 with 90% uncertainty bounds of +0.17 to +2.1W/m^2, only second to CO2 (Bond et al., 2013). Besides, BC can also serve as cloud condensation nucleus and ice nucleus, forming cloud and snow, leading to either warming or cooling effects, which brings large uncertainty for modeling the overall effects of BC in the atmosphere. Apart from its role in climate change, BC is one of the common air pollutants in urban areas. There are many studies indicating the adverse effects of BC on human health (Liu et al. 2023; Rasking et al. 2023; Sedlacek et al., 2022; Wen et al., 2023; Yang et al., 2023; Zhang et al., 2023). Although anthropogenic emissions are the predominant sources of BC in urban regions, natural sources such as wildfires could contribute to a large increment of BC mass concentration, especially when wildfires last for a lengthy period (Ref), which even complicates the situation of urban air pollution. Thus, WHO has suggested it is necessary to make systematic measurements of BC mass concentration as an addition to current prevalent air pollutant measurements (WHO, 2021). To improve the availability of BC data, modeling methods could be used to simulate the variation of BC mass concentration, considering the big budget of purchasing new diverse instruments for BC.

Data-driven machine learning (ML) models have been widely used in environmental science to predict concentrations of air pollutants. Although there are various process-driven chemical transport models (CMTs), such as NASA Goddard Earth Observing System (GEOS)-Chem and Weather Research and Forecasting model coupled to Chemistry (WRF-Chem), which

can predict concentration of air pollutants, the high computation cost and the dependence on regional or global emission inventories make CTMs inaccessible for most of places in the world. However, compared with CTMs, ML models are more flexible. ML models do not rely on physical or chemical processes to simulate the variations of air pollutants. If historical data are provided, ML models can be trained to predict future concentrations for one site, regions, or the globe.

Land use regression (LUR), support vector machine (SVM), (more specifically, support vector regression (SVR)), and tree-based methods such as random forest (RF) and extreme Gradient Boosting (XGBoost) are popular ML algorithms for regression tasks, such as predicting concentrations of air pollutants, because they perform well. More importantly, models based on these algorithms are more interpretable. It is technically feasible to explain how features (input factors) affect the outcome of these models, which could indicate physical and chemical processes that air pollutants undergo in the atmosphere. For example, Xu I. et al. (2020) employed XGBoost methods to predict ultra-fine particle concentrations. Zhou et al. (2022) used the RF algorithm to decouple the effects of meteorological factors on the variation of PM2.5 during COVID-19. Men et al. (2023) used a RF regression method predicted the concentration of PM2.5 indoor. There are also other researchers who compared the results from multiple algorithms to evaluate performance and interpretability of their models (Fung et al., 2021; Rovira et al., 2022; Sun et al., 2022; Wang A. et al., 2020a). When it comes to long-term events, the recurrent neural network (RNN) has drawn more interest because RNN could capture nonlinear relationships of physical and chemical processes better and provide higher accuracy for time series data. The Long short-term memory (LSTM) models are based on RNN but with LSTM cells to overcome the problem of losing information during the training process. As such, LSTM models perform much better for

processing and predicting very long time series patterns. Indeed, LSTM has been utilized successfully to predict air pollution (Tsai et al., 2018; Wang J. et al., 2020b; Yan et al., 2021).

In this work, we applied a LSTM model to predict BC mass concentration based on the 5-year hourly concentrations of common air pollutants including CO, NO_x, $PM_{2.5}$ and O_3 from an air pollution monitoring station which is the only site where data of BC mass concentration are available from 2018 to 2022 in Montreal, Canada. The input data are the concentrations of above air pollutants except BC, plus three time variables and the output of the model are predicted values of BC mass concentration at the same hour. The observation data of BC were used for comparison with predicted values to evaluate the performance of the LSTM model.

4.2 Methodology

4.2.1 Data acquisition and preprocessing

The hourly average concentrations of CO, NO, NO_2, $PM_{2.5}$, O_3, and BC were acquired from the air pollution monitoring station conducted by City of Montreal and Environment Canada and Climate Change (ECCC) (RSQA 2024). The station is located at 45.651722° N, 73.573896° W, and the station number is 55. The hourly average concentrations of NO_x were calculated as the sum of NO and NO_2. The station started to measure BC mass concentration in 2018. And the most recent updated data is till 2022.

Since these air pollutants are measured by several different instruments, there are some cases where the concentrations of at least one type of air pollutants were not recorded. All the data at these hours were removed from the datasets. In the end, the train/test/new datasets contain all the information of these air pollutants simultaneously. The data from 2018 to 2021 was used for

training and testing the model, which contained 28927 hours (28927 samples). And the data of 2022 (from January to June) was used to compare with the model prediction. There are 4745 hours recorded in 2022 but with 4189 hours recorded during January to June and the rest hours recorded in December. Thus, only the first 4189 hours (samples) were used for comparison. Furthermore, the outliers for each pollutant were also removed following the same manner of removing missing values. In the end, data used for training the model contained 25242 samples (22717 samples in train set and 2525 samples in test set), and the data for comparison (new data set) contained 3596 samples.

4.2.2 The LSTM model

LSTM was first proposed by Hochreiter and Schmidhuber in 1997 (Hochreiter and Schmidhuber, 1997) and was gradually improved over the years to tackle the problem of long-term memory. The common architecture of LSTM consists of a memory cell with the cell state (short-term state $h_{(t)}$ and long-term state $c_{(t)}$) and three regulatory gates: the input gate ($i_{(t)}$), the forget gate ($f_{(t)}$), and the output gate ($o_{(t)}$). The cell state enables the transmission of information. The input gate controls which part of information should be added into the long-term state. The forget gate controls what should be discarded from the long-term state. The output gate determines which parts of the long-term state should be output to the short-term state and the predicted result ($y_{(t)}$) at the timestamp *t*. The activation function of these three gates is the logistic sigmoid function (σ) whose output ranges from 0 to 1. The computation equations are listed below:

$$i_{(t)} = \sigma\left({W_{xi}}^{T} x_{(t)} + {W_{hi}}^{T} h_{(t-1)} + b_i\right) \quad (1)$$

$$f_{(t)} = \sigma\left(W_{xf}{}^{T} x_{(t)} + W_{hf}{}^{T} h_{(t-1)} + b_f\right) \quad (2)$$

$$o_{(t)} = \sigma\left(W_{xo}{}^{T} x_{(t)} + W_{ho}{}^{T} h_{(t-1)} + b_o\right) \quad (3)$$

$$g_{(t)} = tanh\left(W_{xg}{}^{T} x_{(t)} + W_{hg}{}^{T} h_{(t-1)} + b_g\right) \quad (4)$$

$$c_{(t)} = f_{(t)} \otimes c_{(t-1)} + i_{(t)} \otimes g_{(t)} \quad (5)$$

$$y_{(t)} = h_{(t)} = o_{(t)} \otimes tanh\left(c_{(t)}\right) \quad (6)$$

where *g(t)* is the candidate to be added into the long-term state. W_x and W_h are the weight matrices corresponding to the input vector *x(t)* and the short-term state *h(t)*, respectively. "T" in superscript represents transpose of matrix. "b" is the bias term.

In this work, we used hourly average concentrations of CO, NO_x, $PM_{2.5}$, O_3, "Day of Year", "Hour of Day", and "Day of Week" as inputs data which were then scaled to within 0 to 1 for training. BC mass concentrations were outputs of the model. Adaptive momentum ("Adam") was used as the optimizer to minimize the loss function. Mean square error (MSE), root mean square error (RMSE), and correlation coefficient (R^2) were used to evaluate the performance of the model.

4.3 Results and Discussion

4.3.1 The variation of air pollutants in Montreal

Fig. 4.1 shows the diurnal variations of air pollutants averaged over the 5-year dataset. All the pollutants, except O_3, demonstrated an obvious "rush-hour" peak during the morning, indicating the anthropogenic sources (transportation) of these air pollutants. With the development of planetary boundary layer (PBL) during daytime, the concentrations of CO, NO_x, $PM_{2.5}$, and BC

decreased, while the concentration of O_3 increased because of daytime photochemistry. The concentrations of CO, NO_x, $PM_{2.5}$, and BC gradually increased since afternoon and reached another peak during nighttime, because there was an evening "rush-hour" effect and PBL became lower at night. The variation of $PM_{2.5}$ was slightly different from CO, NO_x, and BC, indicating that there were probably other emission sources during nighttime. Considering the station is near a park, heterogeneous formation of SOA during nighttime could contribute to the increment of $PM_{2.5}$.

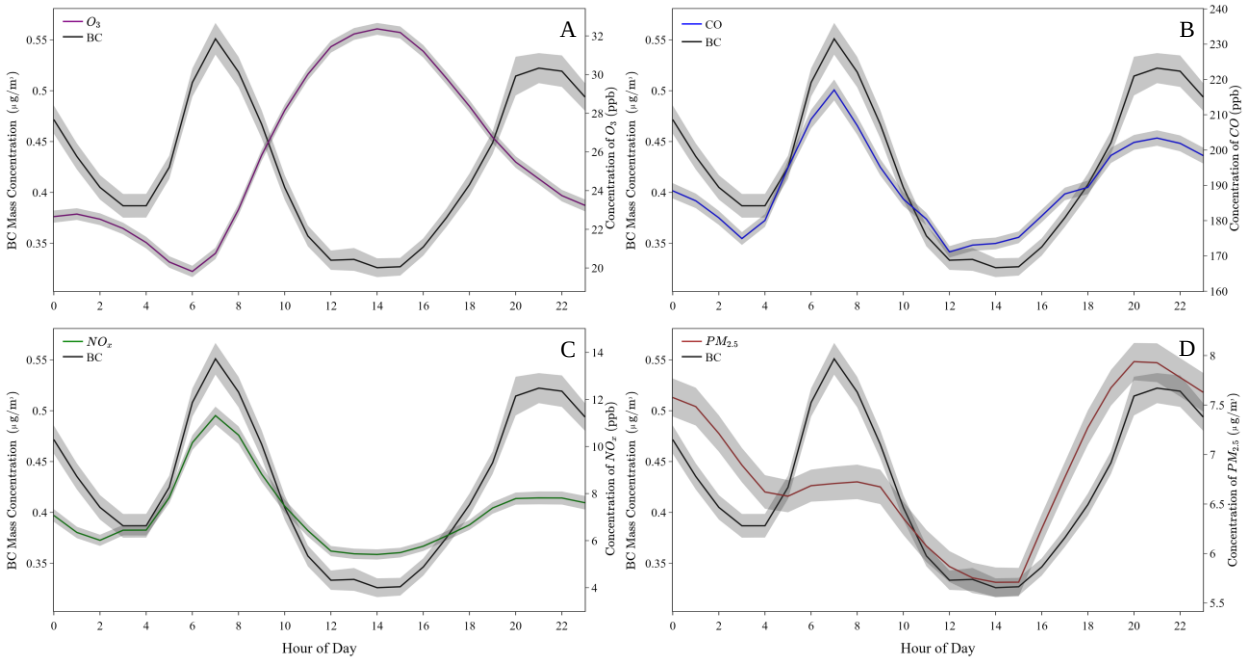

Figure 4.1. Diurnal variations of air pollutants including O_3 (A), CO (B), NO_x (C), and $PM_{2.5}$ (D), and comparison with BC. The shadow areas indicate standard errors.

Fig. C1 and Fig. 4.2 demonstrate the seasonal variations of BC and comparison between O_3, CO, NO_x, $PM_{2.5}$, and with BC respectively. The seasonal variations of CO, NO_x, $PM_{2.5}$, and BC demonstrate a winter peak, whereas $PM_{2.5}$ and BC sometimes show another peak around summer or fall, which could be due to wildfires as discussed in ***Chapter 3***. The concentration of O_3 reaches peak values during summer, as a result of photochemistry.

The similar variations of CO, NO_x, $PM_{2.5}$, and BC and the opposite variation between O_3 and BC can be confirmed by Fig. 4.3. CO, NO_x, $PM_{2.5}$, and BC show strong positive correlation coefficients, indicating a large proportion of these air pollutants come from some common sources. It is noteworthy that NO and BC are only moderately correlated. NO_2 and BC show stronger correlation. But the correlation between NO_x ($NO+NO_2$) and BC is even stronger, which is why NOx, instead of NO or NO_2, was chosen as an input feature of the model. The correlation coefficients and the variations of these air pollutants are similar to the results that were also observed in Montreal (Li & Ariya, 2021). Thus, the datasets here are considered representative.

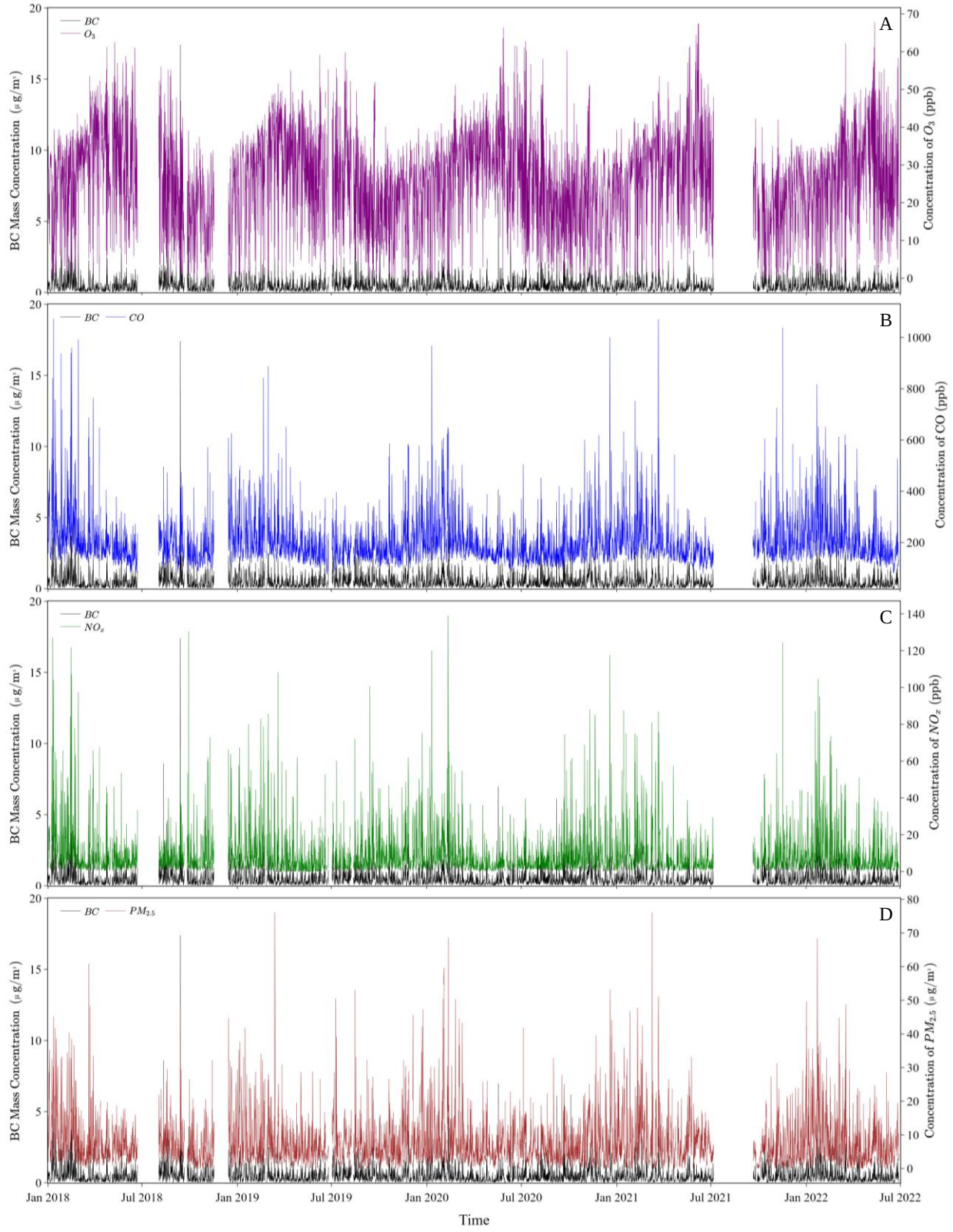

Figure 4.2. Hourly average concentrations of O_3 (A), CO (B), NO_x (C), and $PM_{2.5}$ (D), and their comparison with BC during 2018 to 2022.

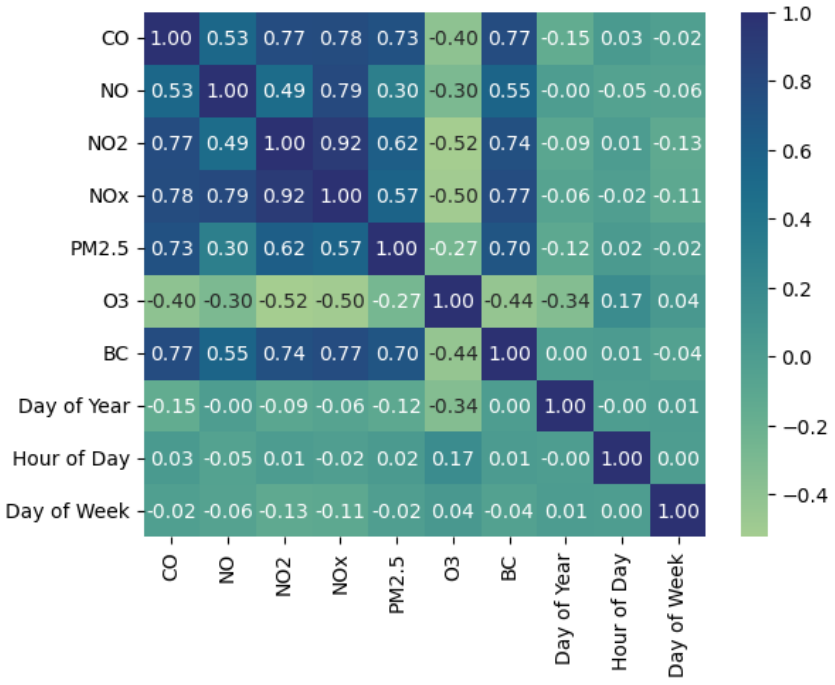

Figure 4.3. Correlation coefficients between each feature of the model.

4.3.2 Evaluation of the LSTM model performance

Table 4.1 demonstrates the performance of the model on different datasets with or without outliers included. If outlier data are included, the overall performance of the model is not so good, with R^2 is around 0.75. More importantly, if including outliers, all the metrics of the train set are worse than that of test set, which may indicate a underfitting of the model because the model was trained with the train set. Once removing outliers before training the model, the performance improved on all three datasets. The RMSE and MSE of the train set and the test set are close, showing that the model can generalize in a good way, which is also confirmed by the new data set. Fig. 4.4 provides the visualization of the modeling results by comparing measured values with predicted values. It is noteworthy that the performance of the model on the test set was worse than the others, which is possibly due to the small size of the test set. Furthermore, the scatter plots

show that the model performance is better when BC mass concentration is low, given that the data dispersion is more obvious when BC mass concentration is larger than 0.4 μg/m^3 in Fig. 4.4C and 4.4D. But it is clear the performance of the model can be further improved by adjusting the model such as adding more LSTM layers and attributing more samples to the test set.

Table 4.1. Performance of the model on different datasets with or without outliers included in the datasets.

	Dataset	**RMSE**	**MSE**	**R^2**
With outliers	Train set	0.231	0.053	0.738
	Test set	0.171	0.029	0.748
	New data set	0.558	0.311	0.759
Without outliers	Train set	0.097	0.009	0.823
	Test set	0.102	0.010	0.791
	New data set	0.284	0.081	0.806

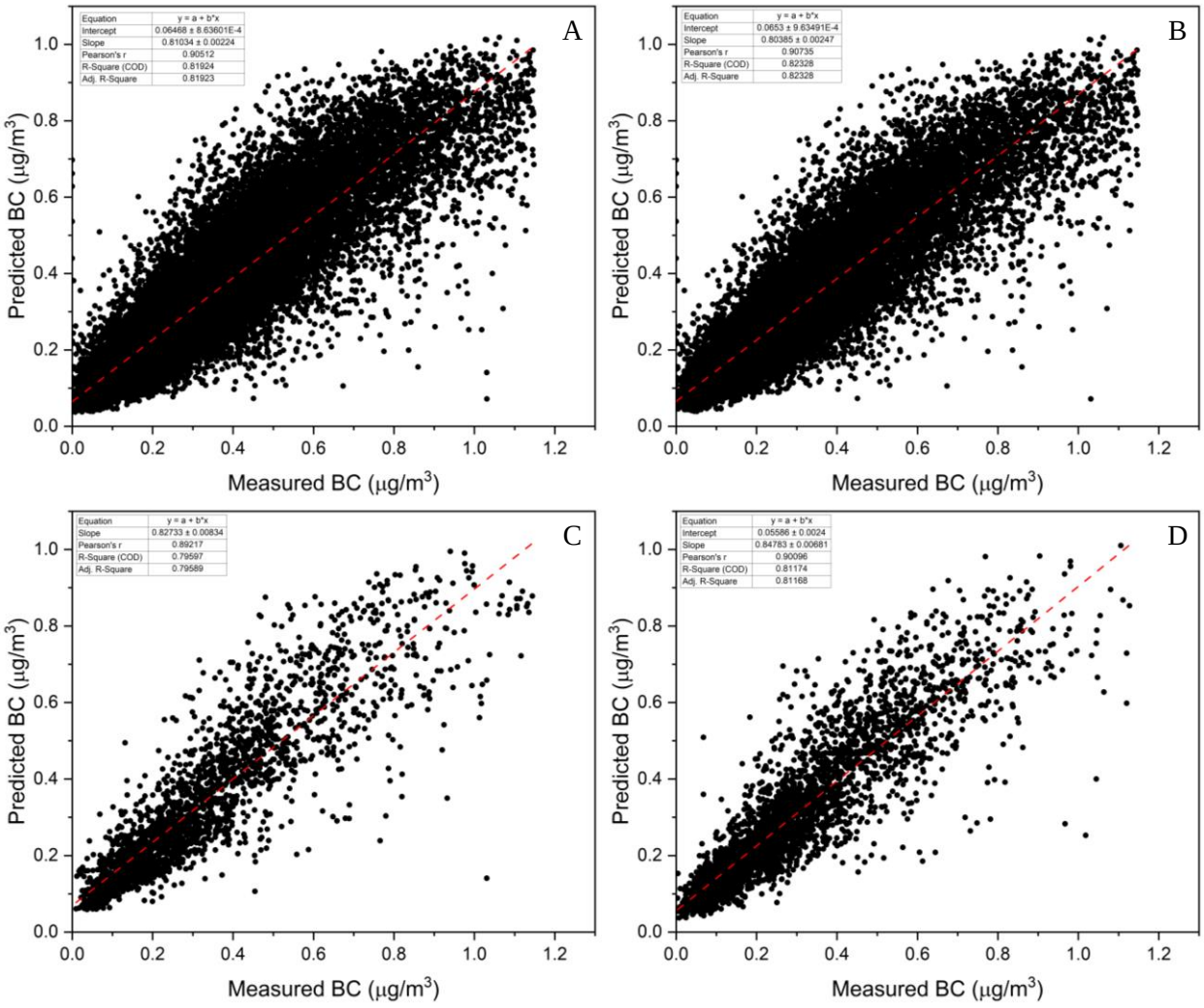

Figure 4.4. The comparison between predicted BC and measured BC in (A) the whole dataset, (B) the train dataset, (C) the test set, and (D) the new data set.

The performance of the model on various subsets divided based on different periods was also evaluated and shown in Table C1. Compared with all data, the model performs good during winter months but slightly worse during summer. One of the possible reasons is that the size of the summer dataset is small, compared with the winter dataset (Table 4.2), which constrains the performance of the model. Additionally, the winter dataset contains 12284 samples, while the summer one contains 4998 samples. The ratio of winter samples to summer samples is about 2.5,

but the ratio of winter days (140) to summer days (92) is only about 1.5, indicating the possibility of sampling bias during summer months. Another potential reason is that wildfires during summer contributed to large mass concentrations of BC and $PM_{2.5}$, which were then removed as outliers before training the model. The performance on the daytime dataset and the nighttime dataset demonstrates no evident differences, and the ratio of sample numbers of these two subsets are also in accordance with the ratio of the number of hours, indicating no sampling bias between these two subsets.

Table 4.2 and Fig. 4.5 show statistical comparisons between measured and predicted BC mass concentrations on different subsets. The mean and median values of measurement data and prediction data are only slightly different, but the standard deviations demonstrate obvious differences, indicating that the measurement datasets show larger variances than the prediction datasets. Furthermore, the model cannot predict extreme values such as minimum and maximum, indicating that the performance of the model will drop when it approaches the boundary of datasets. However, even within the range of minimum and maximum, the performance of the model also varies as suggested by 25% values and 75% values. It is likely that the model performs well on values larger than median value but less than maximum, while the performance drops between minimum and median. In summary, the model tends to overestimate BC mass concentrations when they are smaller than 0.25 $\mu g/m^3$ but underestimate when they are larger than 1 $\mu g/m^3$. Thus, the predicted values tend to be more concentrated towards mean and median values.

Table 4.2. Statistical comparisons of measured and predicted BC mass concentrations on different subsets. Winter is set from December 1st to April 20th. Summer spans from June 21st to September 20th. Daytime is from 9 am to 6 pm, whereas nighttime is from 10 pm to 5 am. "Std" means standard deviation. "25%" and "75%" are first and third quartiles.

Period	Data Type	Count	Mean	Std	Min	25%	Median	75%	Max
All data	Measurement	28840	0.312	0.226	0.000	0.134	0.253	0.433	1.148
	Prediction	28840	0.317	0.203	0.037	0.154	0.259	0.441	1.018

Winter	Measurement	12284	0.283	0.198	0.000	0.128	0.232	0.392	1.146
	Prediction	12284	0.289	0.179	0.052	0.145	0.236	0.395	0.902
Summer	Measurement	4998	0.392	0.254	0.002	0.193	0.334	0.545	1.148
	Prediction	4998	0.393	0.218	0.039	0.211	0.349	0.544	1.012
Day	Measurement	12348	0.285	0.203	0.001	0.130	0.227	0.389	1.145
	Prediction	12348	0.293	0.187	0.041	0.147	0.235	0.397	0.972
Night	Measurement	9532	0.315	0.243	0.000	0.120	0.252	0.451	1.148
	Prediction	9532	0.322	0.211	0.037	0.148	0.261	0.454	1.012

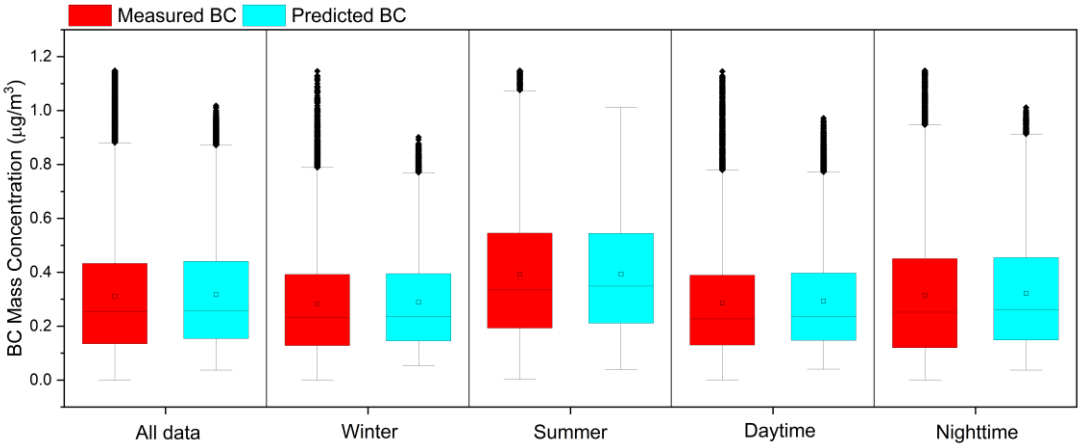

Figure 4.5. Comparison of the distributions of measured and predicted BC mass concentrations on different subsets. The squares inside the boxes show averages of the datasets, while the horizontal line inside the boxes indicate the median values of the datasets. The upper boundary and lower boundary of the box are the third quartile (75%) and the first quartile (25%). The ranges between horizontal bars and boundaries of the boxes indicate 1.5IQR (interquartile ranges). The black points outside horizontal bars are considered outliers of the datasets.

4.4 Conclusion and future work

We developed a ML model based on the LSTM algorithm to predict BC mass concentration by using common air pollutants (CO, NO_x, $PM_{2.5}$, and O_3) and time variables including "Day of Year", "Hour of Day", and "Day of Week" as inputs of the model. We evaluated the performance of the LSTM model and found that the model performed well on moderate values but with overestimation when actual BC mass concentrations was lower than 0.25 µg/m^3, and underestimation when actual BC mass concentrations was larger than 1 µg/m^3. Future work should

be focused on adjusting other hyperparameters to further improve the performance of the model. Adding more LSTM layer to achieve better performance could also be a choice, but it will make the model to be less interpretable. Developing models based on other algorithms such as RF and SVR could also be considered to compare with the LSTM model.

Chapter 5 Conclusions and future work

5.1 Conclusions

The scope of this dissertation work is aimed to characterize the physicochemical properties of LACs in urban regions and demonstrate how various sources of LACs could affect their physicochemical properties and variations. The distinct contributions of this dissertation includes: 1) demonstrating the seasonal trends of LACs concentrations and the impact of human activities in cold-climate urban areas; 2) understanding the change of light absorption of LACs due to wildfires, revealing the great potential of BrC to be a strong absorber in the atmosphere; 3) developing a data-driven ML model to estimate BC mass concentration, providing a feasible and cost-efficient method to make LACs measurement more accessible, thereby reducing the bias in current climate models.

In Chapter 2, we reported one-year measurements of BC mass concentration, along with common air pollutants, in the cold-climate city of Montreal. This dataset is beneficial for future modeling work. We discovered a bimodal distribution in the variation of BC, with one summer peak and one winter peak. The summer peak was attributed to wildfires and was further analyzed in Chapter 3. While the winter peak can last more than 4 months due to the long-winter meteorology of cold climate, highlighting the potential health impacts caused by BC in cold urban settings. Our measurements also covered the period of COVID-19 Pandemic. A lockdown was applied during the pandemic, which strongly constrained most of human activities in the city of Montreal, providing an unexpected opportunity to reveal the huge anthropogenic impacts on the environment. The lockdown led to a decrease up to 72% of all the air pollutants. Additionally, we found that BC mass concentrations near the Montreal international airport were 400% higher than in downtown Montreal, which may pose threat to the health of airport workers and residents nearby,

calling for betterment of current air pollution regulatory policy, with the expansion of aviation in the world.

In Chapter 3, we first confirmed the long-winter BC peak discovered in Chapter 2. The observation was expanded to BrC to demonstrate the variation of the whole LACs, and focused on the record-breaking wildfires in Canada, in the summer of 2023. We confirmed that the summer peak observed in Chapter 2 was due to summer wildfire events. Although the wildfires took place a few hundred kilometers away from the city of Montreal, this metropolitan area was still strongly affected by the wildfires indirectly. The concentration of $PM_{2.5}$ was elevated by more than 300%, whereas BC mass concentration increased more than 26%. Moreover, as the dominant sources of BrC, the wildfires brought a large amount of primary BrC and secondary BrC precursors. The latter were then transformed into secondary BrC during the long-range transport from the sources to urban areas of Montreal. Although the light absorption of BrC decays sharply with increasing wavelengths, BrC demonstrated strong absorption at short wavelengths like 370 nm, accounting for more than 50% of total light absorption, which surpassed the contribution of light absorption of BC at this range. Since wildfires are estimated to take place more frequently because of climate change, BrC gradually become more essential for comprehensively evaluate both global and regional impacts of wildfires, which necessitates more ground-based observation of BrC as a complement to measurement of BC for more precise modeling work in the future.

The measurements of BC are now more rely on laboratory research, and less prevalent in municipal air pollution monitoring networks. One of the important reasons is the insufficient budget for purchasing instruments specifically for BC. Thus, in Chapter 4, we developed an ML model to estimate BC mass concentrations based on the concentrations of other air pollutants, including $PM_{2.5}$, O_3, NO_x, and CO, which are now continuously measured. Our model achieved

good performance on the 5-year datasets, showing promising capability to generalize on more data. More importantly, since this model does not rely on historical observation of BC, it can be used to estimate historical BC mass concentrations as long as the concentrations of the aforementioned air pollutants are available. This can greatly benefit modeling research by providing constraints on historical impacts of BC.

5.2 Future work

This thesis mainly focuses on light absorption properties of LACs, with some offline chemical characterization such as TEM and SEM coupled. The properties of LACs are correlated with each other. A combination of information about size, morphology, mixing state, chemical composition, and light absorption of LACs would be beneficial for evaluating both climate effects and health effects of LACs. Thus, one of advancements can be done based on this work is to measure the size distribution, light absorption, and chemical compositions simultaneously, which can be achieved by coupling size scanner or SP2, multiwavelength photometer or aethalometer, and AMS. Although HPLC-MS or GC-MS could also provide chemical information of LACs, the advantage of AMS is that it can measure LACs in-situ. AMS will not change the size or morphology of particles, which is closer to real situations in the atmosphere.

Furthermore, there are studies about ice nucleation of BC but with contradictory results, while the research on ice nucleation of BrC is still limited. To better understand the indirect climate effects of LACs, it is necessary to do more laboratory research on ice nucleation of LACs. More importantly, the occurrence of wildfires is estimated to increase. Wildfires can emit smoke with BC and BrC directly into the atmosphere, and it is very likely that BC and BrC exist as mixtures

in smokes of wildfires. A better way is to study the ice nucleation of the mixture of BC and BrC, instead of each single part respectively, in laboratory research, to elucidate the indirect climate effects of LACs.

Data-driven machine learning models can be widely developed and applied in research based on specific research topics, such as predicting light absorption properties of BrC. The model we present in this work is based on air pollutants which are correlated with BC. Thus, the example we demonstrated is based on correlation inference, instead of causal inference. If data of BC sources are available, a more reliable ML model can be developed based on causal inference. The International union of pure and applied chemistry (IUPAC) has nominated large language model in chemistry as one of 2023 top ten emerging technologies in chemistry (IUPAC 2023), indicating wider application of ML models as promising methodology to help research in chemistry in the future.

Appendix A

A Chapter 2 Supplementary Information

A.1 Supplementary figures

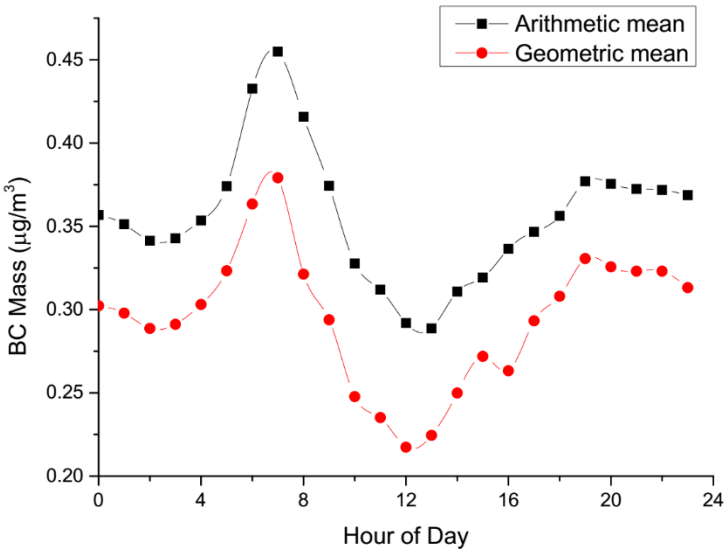

Figure A5.1. The annual arithmetic means and geometric means of BC Mass.

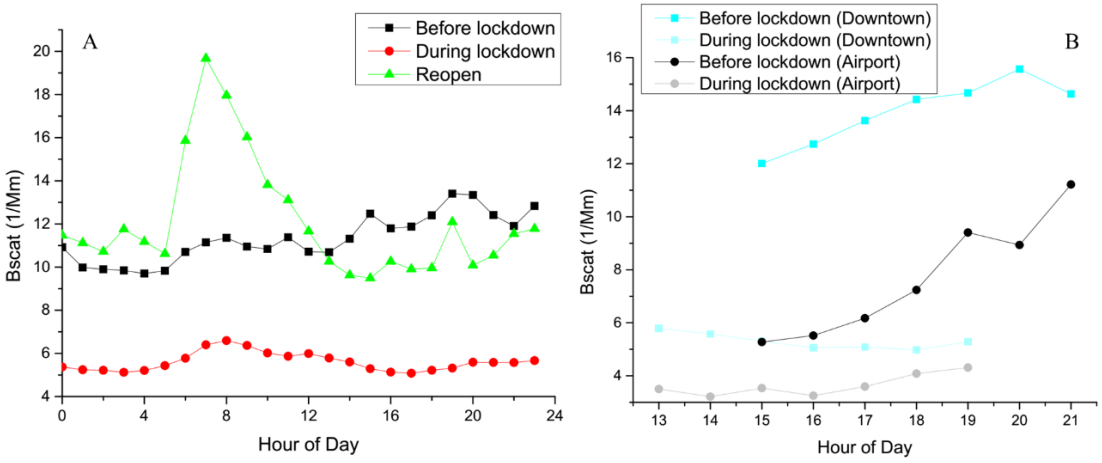

Figure A2. Diurnal variation of B_{scat} in downtown Montreal before lockdown (black line, Feb. 1st to Mar. 15th), during lockdown (red line, Mar. 16th to May 24th) and partial Reopen (green line, May 25th to Jun.

30th) (**A**); Comparisons of B_{scat} in downtown Montreal (cyan) with near YUL Airport (black) in COVID-19 Pandemic (**B**).

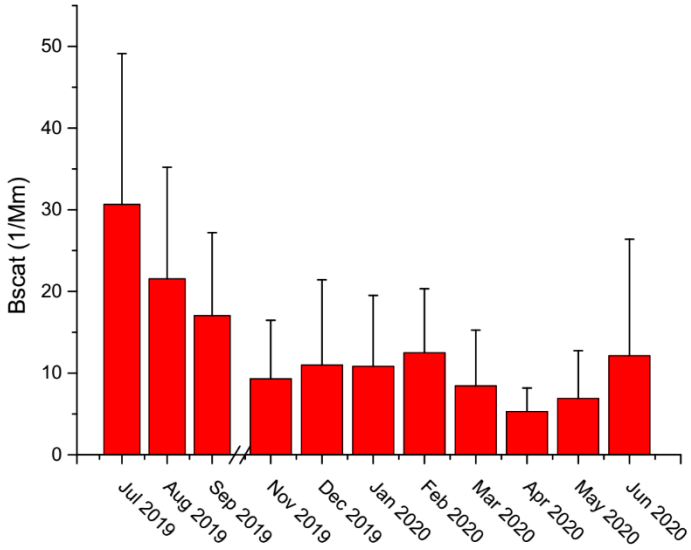

Figure A3. Monthly mean values of B_{scat}. The error bars indicate standard deviations.

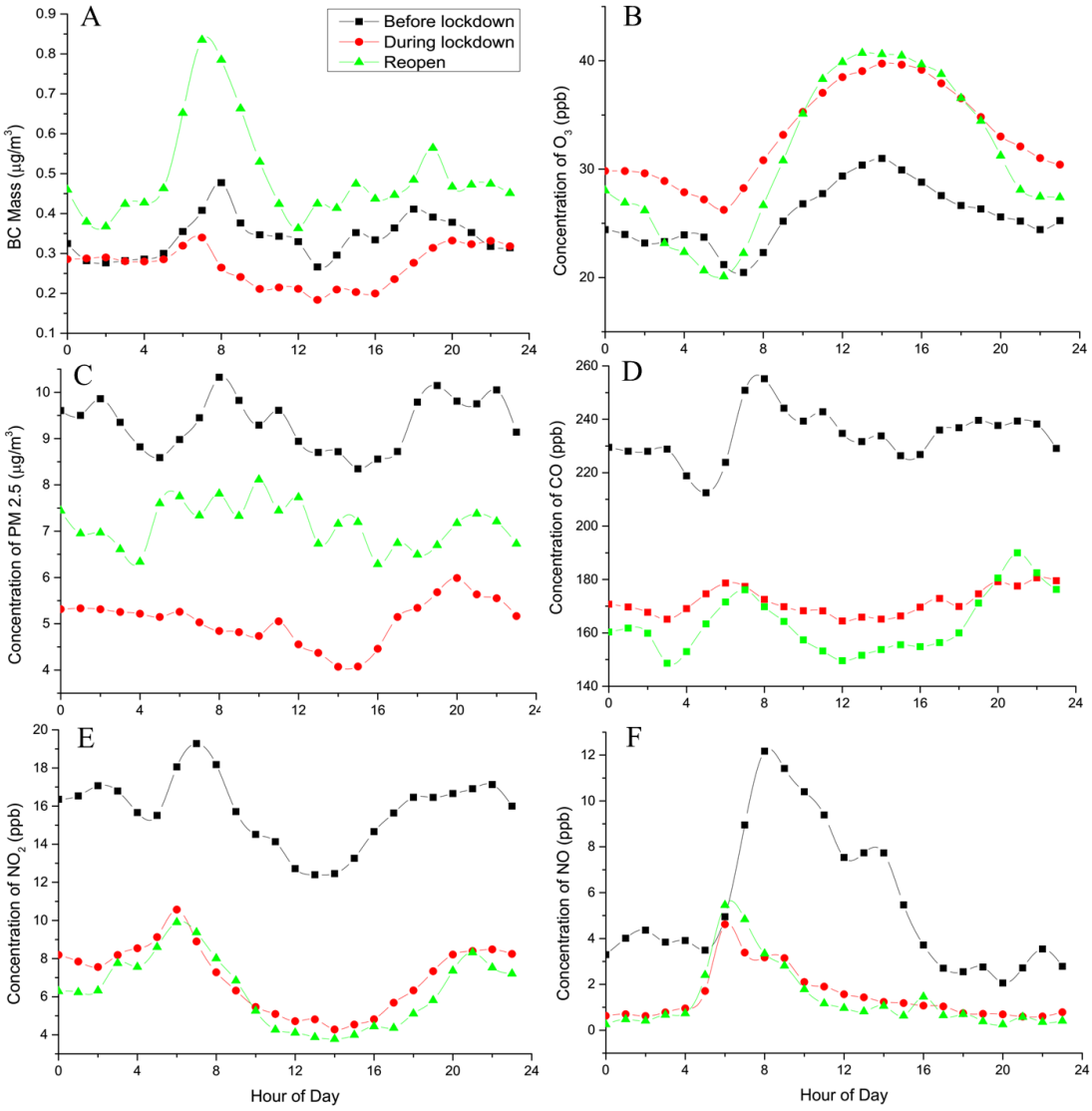

Figure A4. Diurnal variation of the concentrations of BC (**A**), O_3 (**B**), $PM_{2.5}$ (**C**), CO (**D**), NO_2 (**E**) and NO (**F**) in Montreal before (black) and during lockdown (red), and partial Reopen (green line). The period of "Before lockdown" is set from Feb. 1st to Mar. 15th. The period of "During lockdown" is set from Mar. 16th to May 24th. And the period of "partial Reopen" spans from May 25th to Jun. 30th.

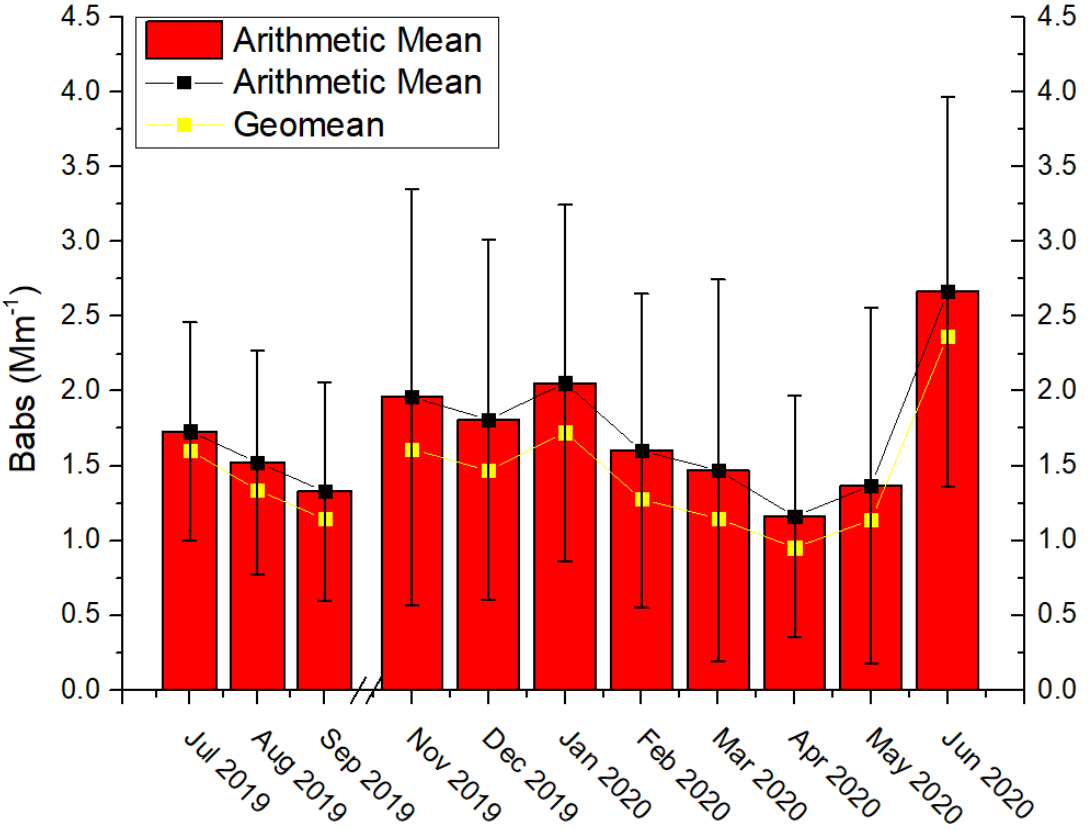

Figure A5. Monthly mean values of B_{abs}. The error bars indicate standard deviations.

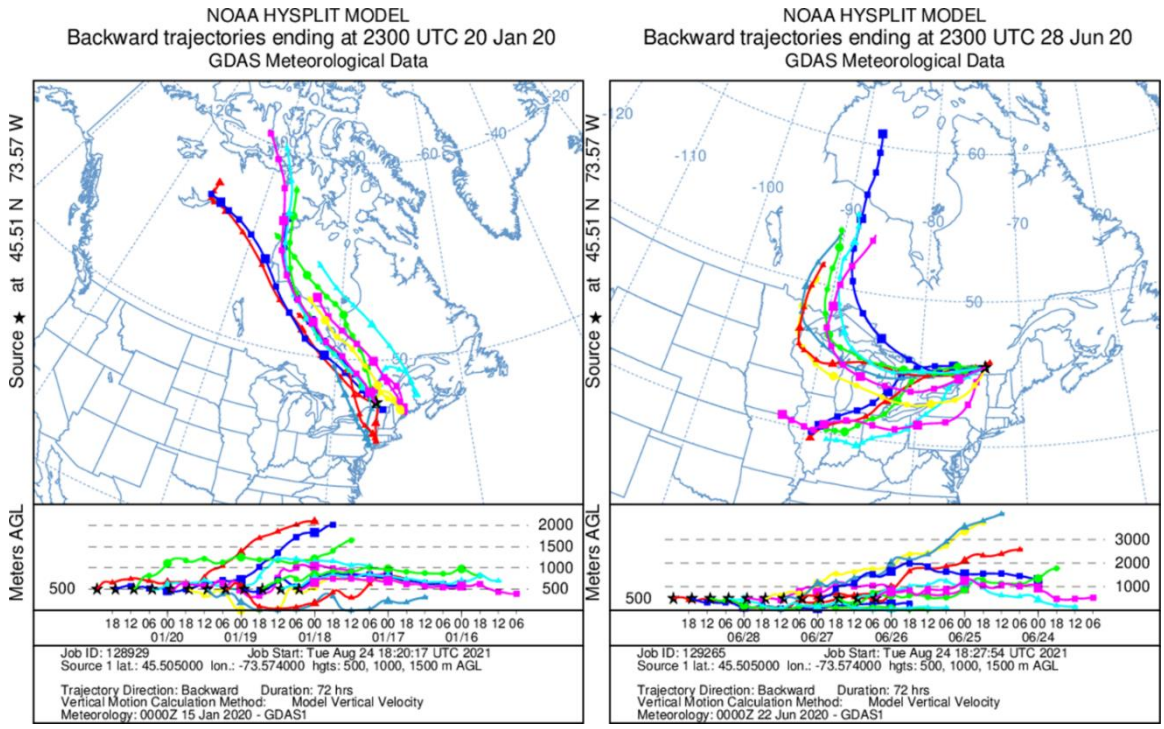

Figure A6. HYSPLIT back trajectory modeling results on a winter day (Jan. 20th, 2020) and on a summer day (Jun. 28th, 2020).

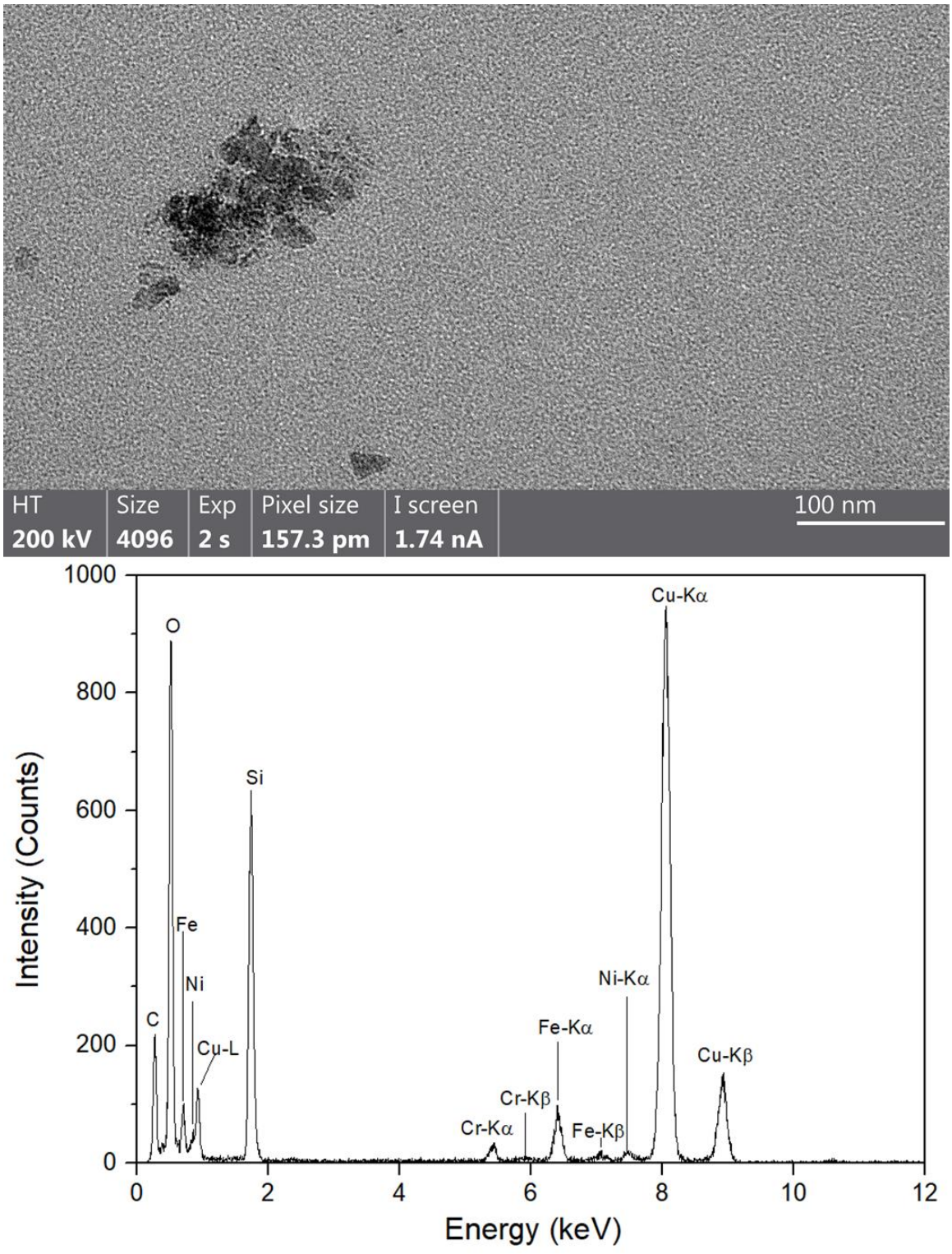

Figure A7. HR-TEM-EDS results of the aged snow samples collected from the airport, indicating the existence of emerging metal contaminants.

A.2 Supplementary tables

Table A5.1. P values of the statistics analysis within March and May.

MONTH	BC MASS	$PM_{2.5}$	CO	O_3	NO	NO_2	B_{SCAT}
MAR	0.001	<0.001	<0.001	0.01	0.002	<0.001	<0.001
MAY	<0.001	<0.001	<0.001	0.11	0.49	0.89	<0.001

Table A5.2. Concentrations of CO during January to June from 2017 to 2020. The number in the bracket of March 2020 indicates the average concentration of CO within Mar. 1st to Mar. 15th, 2020.

TIME	2017	2018	2019	2020
JAN	242.9	271.4	247.7	240.3
FEB	248.2	262.9	239.1	243.5
MAR	253.7	230.9	231.4	203.5 (212.1)
APR	208.4	214.0	201.0	166.8
MAY	179.8	201.2	181.1	166.2
JUN	164.8	172.1	181.9	161.4

Table A5.3. P values of the statistical analysis between January with February, March, April and May in the year of 2017 to 2020, respectively. The number in the bracket of March 2020 indicates the P value based on the average concentration of CO within Mar. 1st to Mar. 15th, 2020.

TIME	2017	2018	2019	2020
FEB	0.827	0.494	0.526	0.467
MAR	0.498	0.014	0.283	0.003 (0.094)
APR	0.002	0.001	P < 0.001	P < 0.001
MAY	P < 0.001	P < 0.001	P < 0.001	P < 0.001

Table A5.4. The averages, standard deviations, median values, 99th percentile values, 1st percentile values, 25th percentile values and 75th percentile values for BC Mass, O_3, $PM_{2.5}$, CO, NO, NO_2 and B_{scat} for March 2020 and May 2020.

	Average	Std	Median	99%	1%	25%	75%
				BC Mass (μg/m^3)			
3.1 ~ 3.15	0.342	0.344	0.280	2.25	0	0.146	0.445
3.16 ~ 3.31	0.285	0.187	0.276	0.769	0	0.156	0.385
5.1 ~ 5.24	0.290	0.188	0.270	0.870	0	0.171	0.395
5.25 ~ 5.31	0.501	0.335	0.498	1.70	0	0.273	0.674

	Average	Std	Median	99%	1%	25%	75%
				O_3 (ppb)			
3.1 ~ 3.15	28.8	8.5	30.8	41.0	2.5	23.9	34.7
3.16 ~ 3.31	31.2	7.1	31.7	44.2	11.9	27.3	36.4
5.1 ~ 5.24	34.1	8.8	33.0	59.2	16.0	28.2	39.6
5.25 ~ 5.31	30.9	12.3	29.1	60.2	6.4	22.4	38.7

	Average	Std	Median	99%	1%	25%	75%
				$PM_{2.5}$ (μg/m^3)			
3.1 ~ 3.15	7.5	6.3	5.5	30.4	0.7	3.4	10.1
3.16 ~ 3.31	5.5	3.1	4.7	13.7	0.7	3.2	7.0
5.1 ~ 5.24	4.9	2.2	4.6	11.7	1.3	3.3	6.0
5.25 ~ 5.31	6.9	4.6	7.5	18.1	0.0	2.8	10.0

	Average	Std	Median	99%	1%	25%	75%
				CO (ppb)			
3.1 ~ 3.15	212.1	69.9	196.9	489.4	145.7	173.1	223.9
3.16 ~ 3.31	195.4	31.0	190.0	277.3	147.5	171.8	212.7
5.1 ~ 5.24	162.0	26.7	159.6	243.3	120.7	142.1	175.9
5.25 ~ 5.31	180.7	49.8	177.1	310.3	102.3	140.3	214.4

	Average	Std	Median	99%	1%	25%	75%
				NO (ppb)			
3.1 ~ 3.15	4.0	8.4	2.1	44.8	0.4	1.3	3.7
3.16 ~ 3.31	2.0	2.0	1.4	10.1	0.1	0.8	2.7
5.1 ~ 5.24	1.2	2.0	0.6	11.0	0.0	0.3	1.3
5.25 ~ 5.31	1.0	1.7	0.5	8.8	0.0	0.2	0.9

	Average	Std	Median	99%	1%	25%	75%
				NO_2 (ppb)			
3.1 ~ 3.15	12.8	7.9	11.1	40.6	3.1	6.9	15.6
3.16 ~ 3.31	9.9	5.4	9.0	27.2	2.9	5.8	12.8
5.1 ~ 5.24	5.5	3.6	4.7	19.3	1.4	2.9	6.8
5.25 ~ 5.31	5.6	4.6	4.2	19.5	0.6	2.3	7.3

	Average	Std	Median	99%	1%	25%	75%
				B_{scat} (Mm^{-1})			
3.1 ~ 3.15	10.53	8.73	7.76	44.78	1.64	4.80	13.27

3.16 ~ 3.31	6.80	4.09	6.26	20.22	0.72	3.81	8.63
5.1 ~ 5.24	5.17	3.29	4.41	18.49	0.97	3.02	6.28
5.25 ~ 5.31	12.09	8.26	12.28	34.92	0.62	3.72	18.17

Table A5.5. Pearson correlation analysis of BC Mass with Co-pollutants.

Month	O_3	NO	NO_2	SO_2	CO	$PM_{2.5}$	B_{scat}
Jul 2019	-0.5703	0.1156	0.6057	0.2873	0.5219	-0.2766	-0.2035
Aug 2019	-0.9093	0.5834	0.8538	0.6529	0.3627	0.8007	0.2657
Sep 2019	-0.7455	0.0793	0.7749	-0.7992	0.5715	0.7007	0.0441
Nov 2019	-0.8318	0.1361	0.8095	-0.6536	0.2909	0.1761	0.1969
Dec 2019	-0.7035	0.2595	0.8300	-0.2211	0.4735	0.2113	0.2715
Jan 2020	-0.5131	0.2801	0.5910	-0.1353	0.7136	0.5242	0.1351
Feb 2020	-0.4394	-0.2508	0.6159	-0.5894	0.3738	0.2787	0.4484
Mar 2020	-0.2592	0.2064	0.6544	-0.1021	0.6280	0.5615	0.7366
Apr 2020	-0.8875	0.1121	0.9329	0.2095	0.9194	0.8141	0.5623
May 2020	-0.5137	-0.0780	0.6516	0.2573	0.5782	0.5250	-0.2554
Jun 2020	-0.6505	0.8211	0.7703	0.9008	0.6290	0.6555	0.9652

Table A5.6. An example snow event during Dec. 31st 2019 to Jan. 2nd 2020 was analyzed. The average and median values of BC Mass, total snow precipitation, snow on the ground and average temperature are given above.

Snow event	Total precipitation	Snow (ground)	BC Mass (µg/m3)		T
	mm	cm	Average	Median	℃
2019/12/31	11.3	13	0.481	0.417	-0.5
2020/1/1	3	19	0.251	0.240	0.3
2020/1/2	0	19	0.549	0.450	1.3

Appendix B

B Chapter 3 Supplementary Information

B.1 Supplementary figures

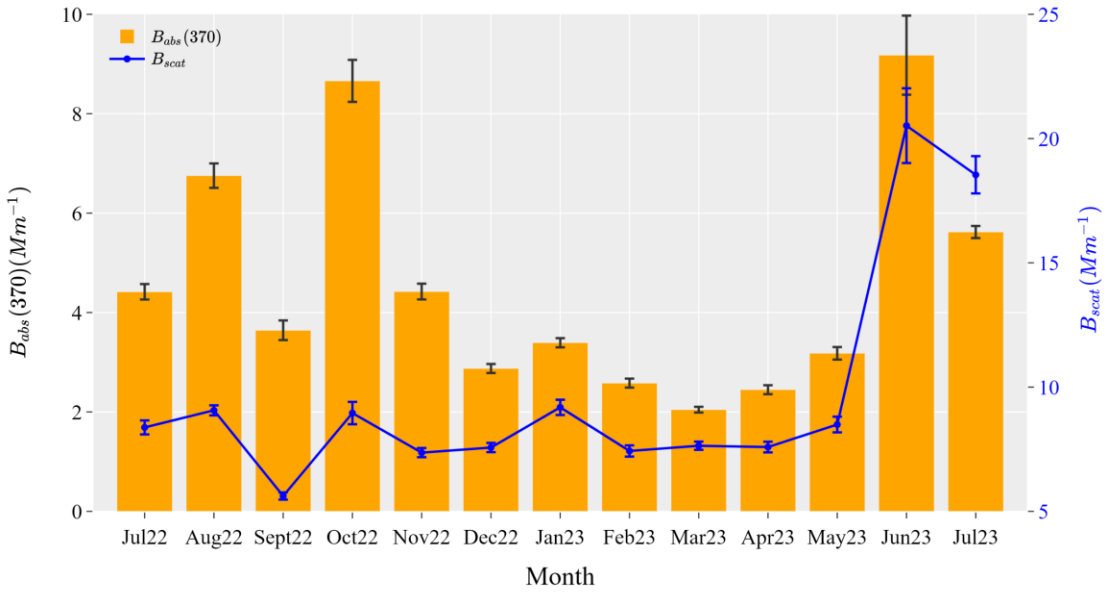

Figure B1. Monthly averages of B_{abs} (370) and B_{scat}. The error bars indicate the standard errors for B_{abs} (370) and B_{scat} for each month.

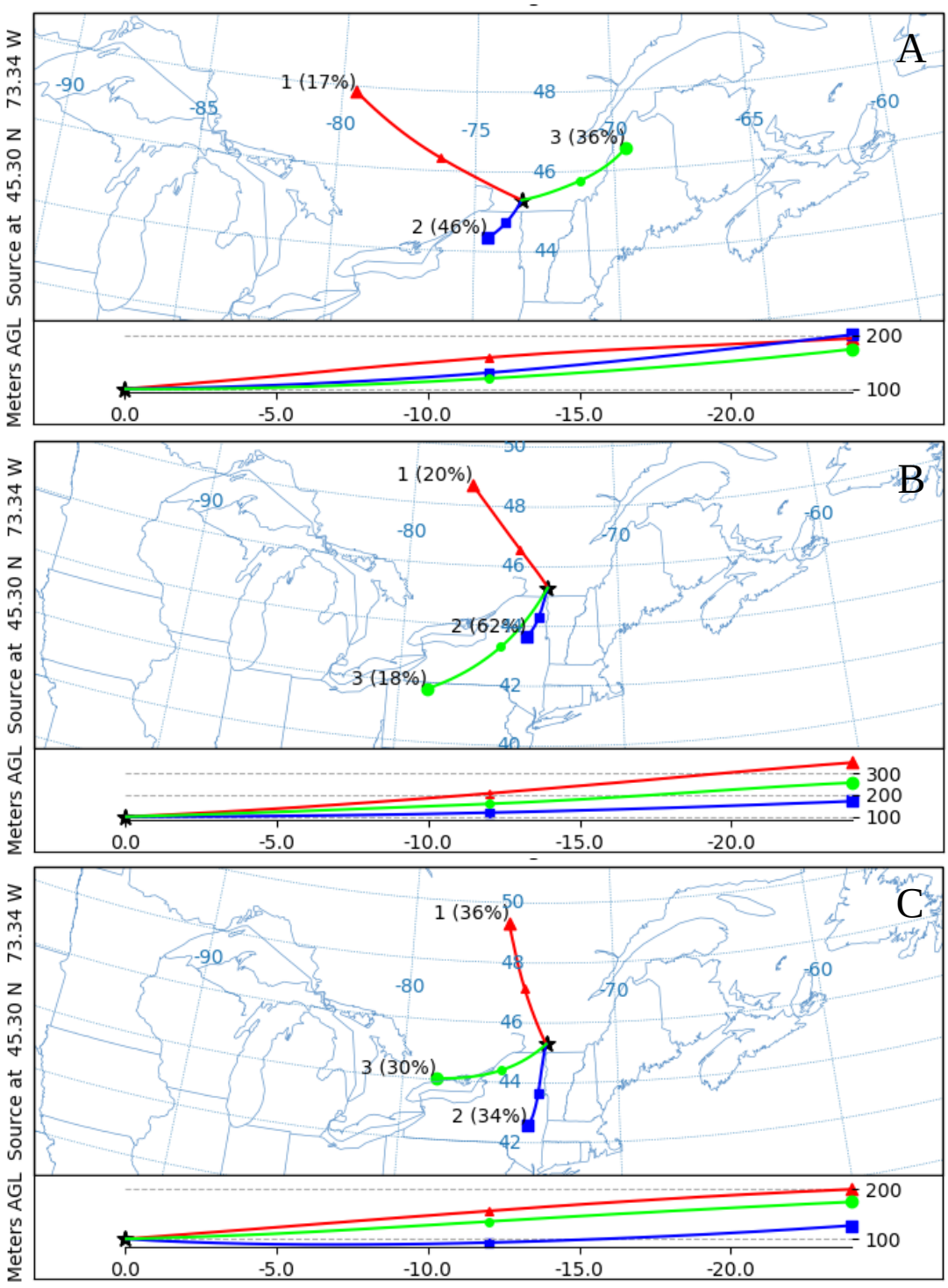

Figure B2. Monthly cluster back-trajectory analysis for October in 2021 (A), 2022 (B), and 2023 (C).

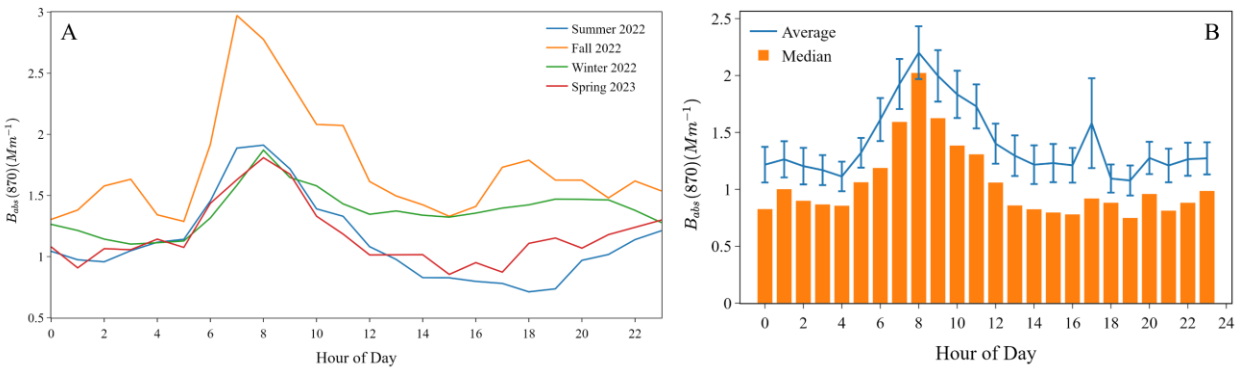

Figure B3. Diurnal variation of B_{abs} (870) in different seasons. Panel B indicates the wildfire months (June and July 2023), and the error bars on blue lines represent the standard errors.

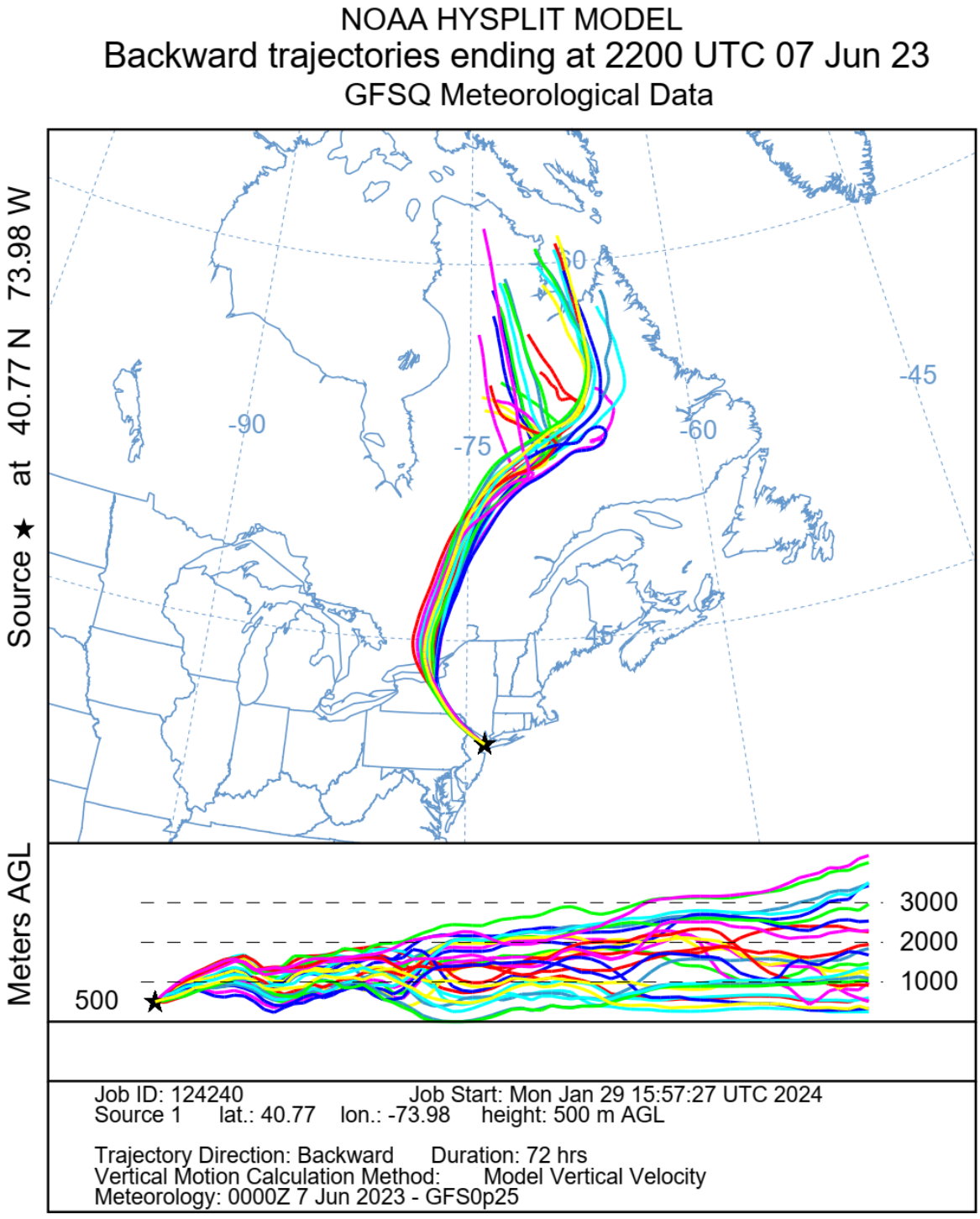

Figure B4. Back trajectory analysis on the source of smoke in New York City at 5 pm (EST) on June 7th, 2023 (Stain et al, 2015; Rolph et al, 2017).

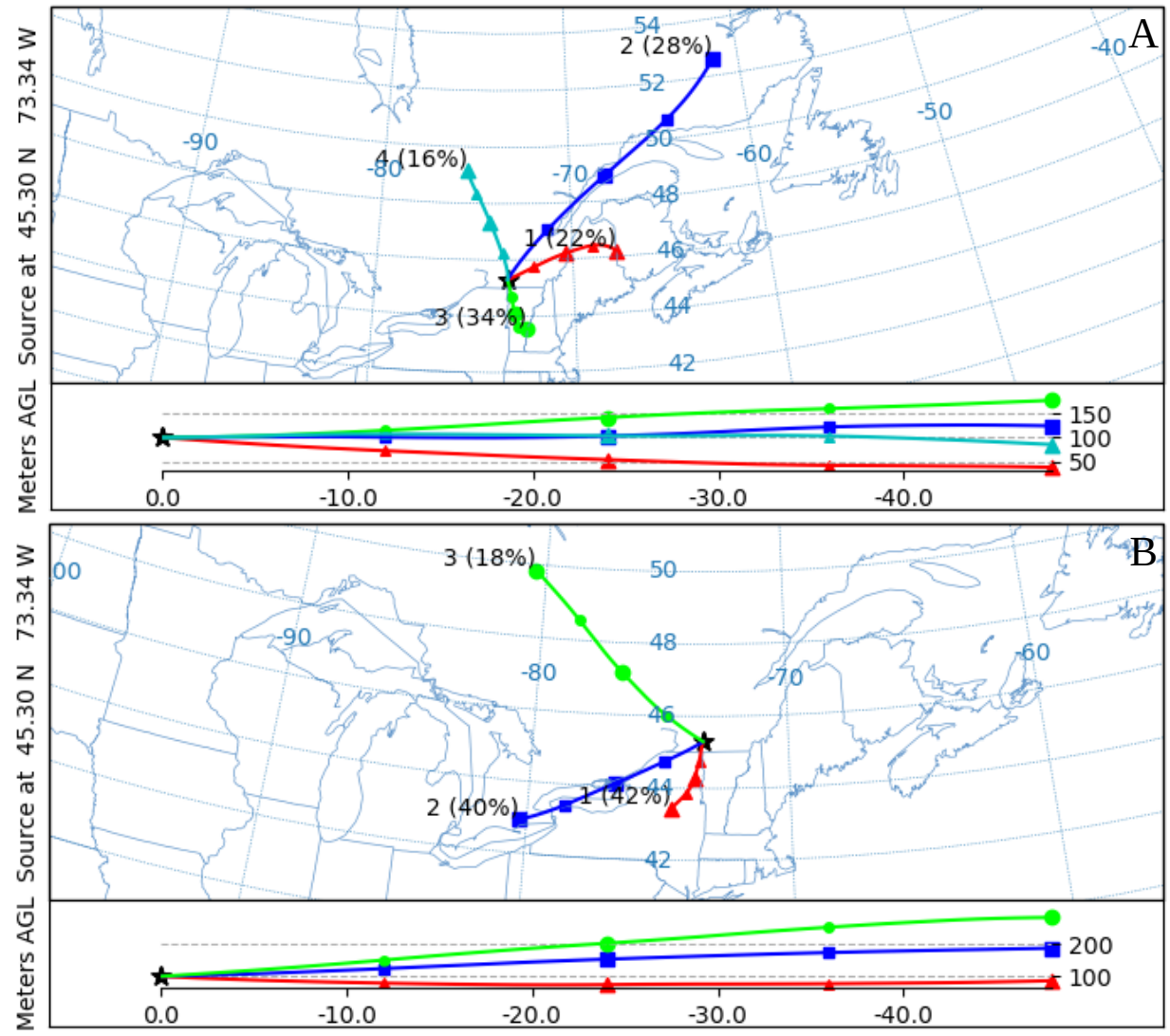
A
Source at 45.30 N 73.34 W
Meters AGL
2 (28%)
4 (16%)
1 (22%)
3 (34%)
150
100
50
0.0
-10.0
-20.0
-30.0
-40.0
B
Source at 45.30 N 73.34 W
Meters AGL
3 (18%)
2 (40%)
1 (42%)
200
100
0.0
-10.0
-20.0
-30.0
-40.0

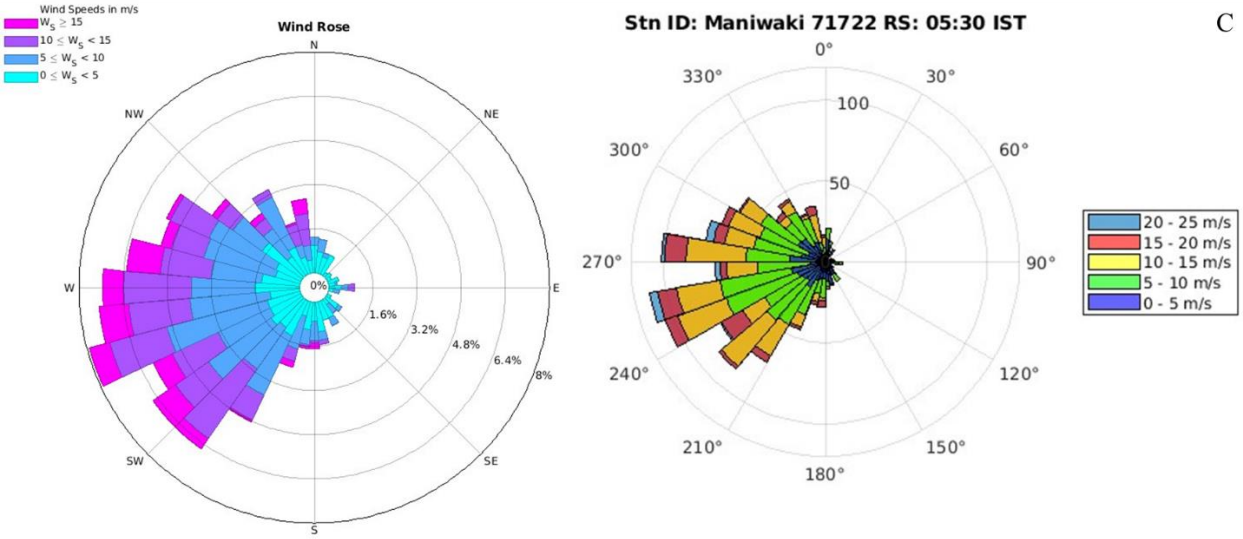
Wind Speeds in m/s
Wind Rose
Stn ID: Maniwaki 71722 RS: 05:30 IST
C
20 - 25 m/s
15 - 20 m/s
10 - 15 m/s
5 - 10 m/s
0 - 5 m/s

Figure B5. Monthly cluster back-trajectory analysis for June (A) and July (B), and wind rose plots for July (C), in 2023.

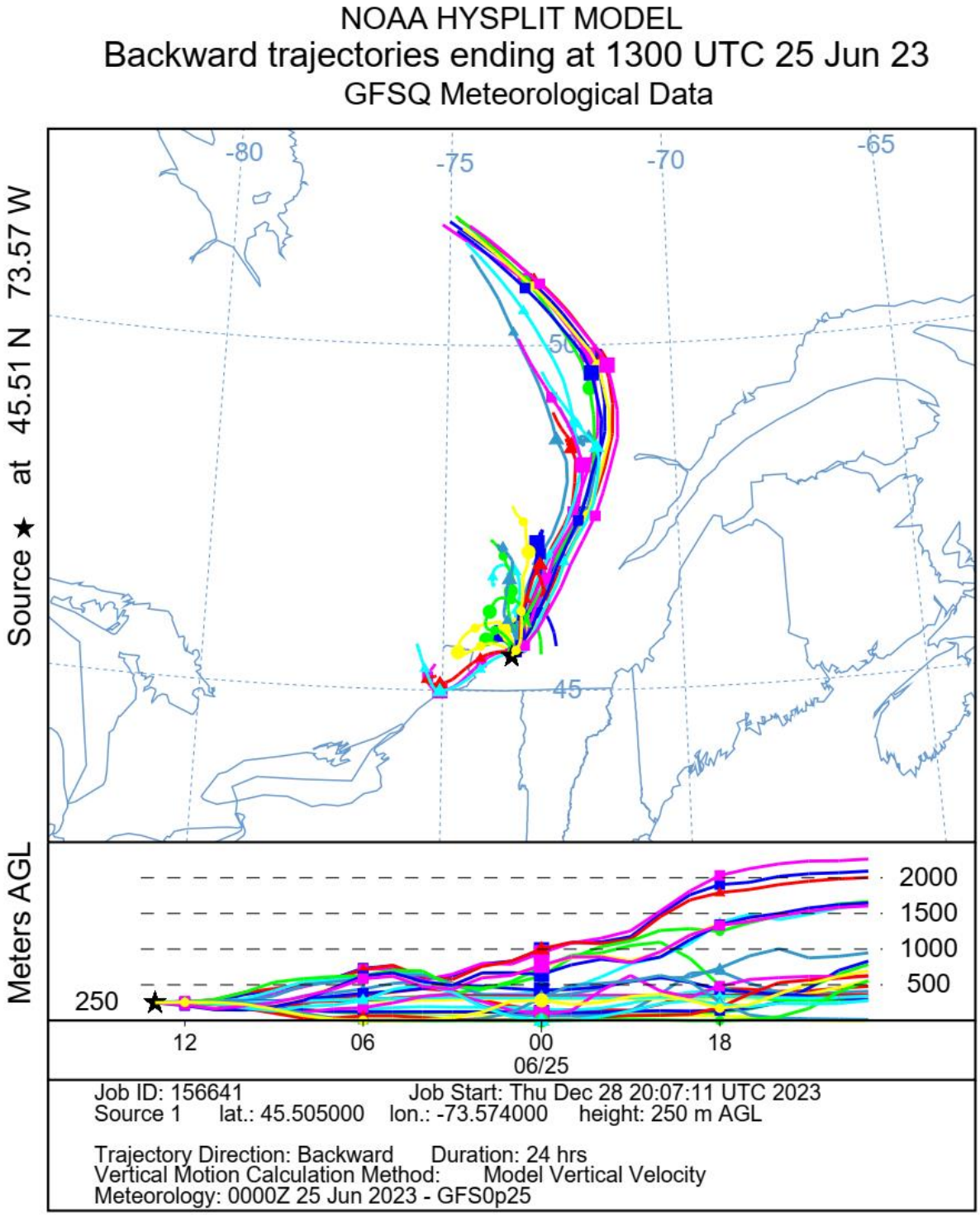

Figure B6. Back trajectory analysis on the source of smoke at the largest B_{abs} (370) moment (8 am EST) in Montreal during June 25th to June 26th, 2023 (Stain et al, 2015; Rolph et al, 2017).

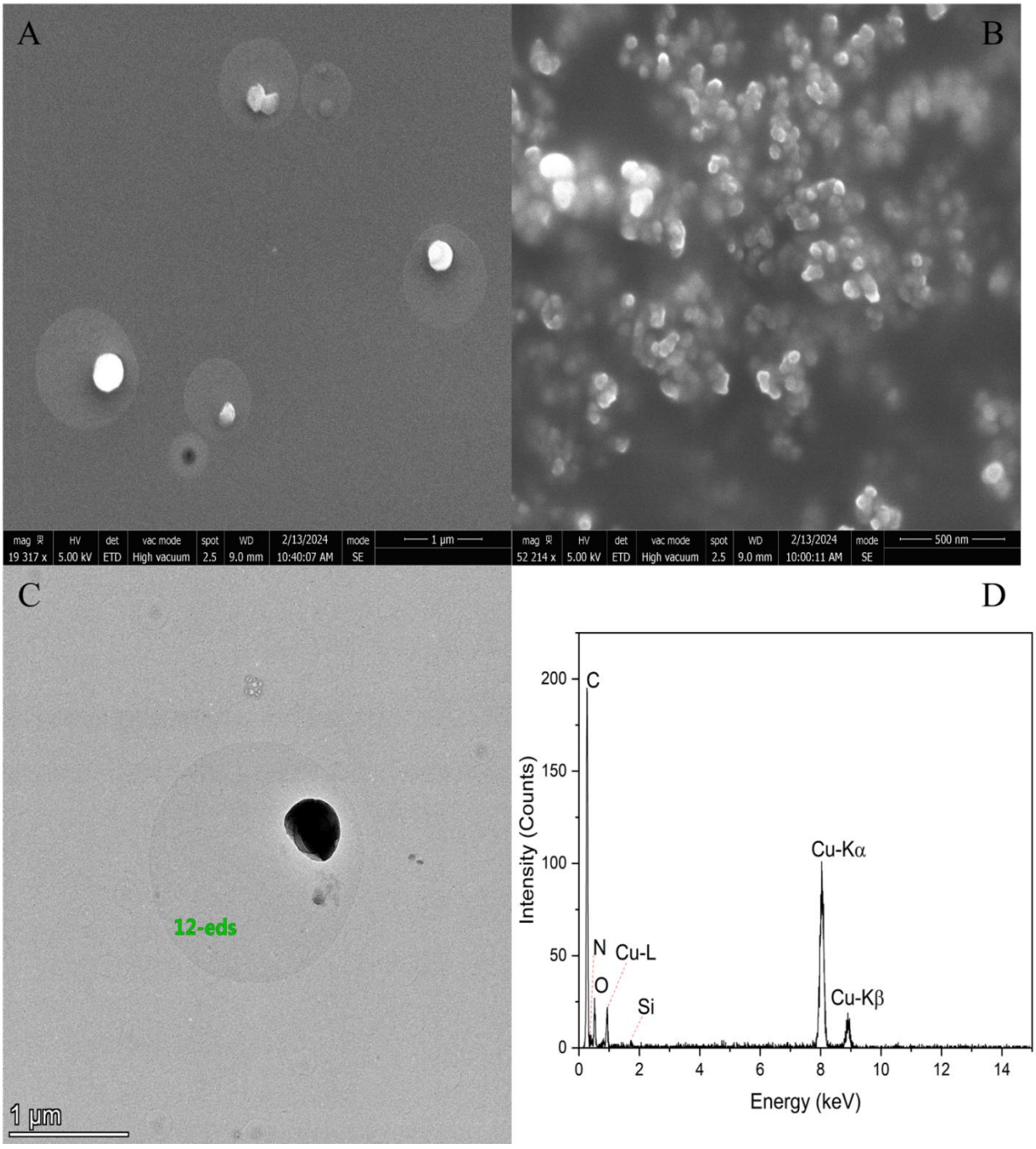

Figure B7. SEM images of aerosol samples (A) and BC agglomerates (B). Panel C shows the TEM image of particles with the coating. Panel D shows the EDS result of the coating at the site labelled with "12-eds".

B.2 Supplementary tables

Table B1. Statistic description of monthly variation of B_{abs} (870) and B_{scat} from 2022 to 2023. "Mean" is the arithmetic average. "Std" is the standard deviation. "25%" and "75%" represent quantile values.

				B_{scat} (Mm^{-1})			
Month	**Mean**	**Std**	**Min**	**25%**	**Median**	**75%**	**Max**
Jun-22	4.63	3.10	0.28	2.24	3.93	6.25	15.60
Jul-22	8.38	6.28	0.76	3.60	6.23	11.50	32.78
Aug-22	9.06	5.05	1.67	5.74	8.01	11.33	32.18
Sep-22	5.62	3.83	0.71	2.75	4.69	7.30	23.90
Oct-22	8.95	12.03	0.78	4.64	7.05	10.04	198.58
Nov-22	7.36	4.33	0.58	3.64	6.56	10.25	21.48
Dec-22	7.57	5.04	0.83	4.03	6.17	9.64	27.73
Jan-23	9.18	7.67	1.28	3.95	7.09	11.90	53.33
Feb-23	7.43	4.81	1.59	3.77	6.52	9.45	27.45
Mar-23	7.64	3.93	1.17	4.68	7.19	9.73	23.90
Apr-23	7.59	5.60	0.87	4.30	6.10	9.24	48.60
May-23	8.49	7.52	1.61	4.42	6.79	11.09	104.84
Jun-23	20.52	38.39	0.44	2.65	5.43	19.33	324.62
Jul-23	18.54	20.30	1.04	6.16	10.55	22.15	121.07

				B_{abs} (870) (Mm^{-1})			
Month	**Mean**	**Std**	**Min**	**25%**	**Median**	**75%**	**Max**
Jun-22	1.08	1.33	0.02	0.40	0.77	1.34	16.09
Jul-22	0.99	0.77	0.02	0.50	0.79	1.27	5.88
Aug-22	1.26	1.00	0.01	0.65	1.01	1.63	8.32
Sep-22	1.10	0.88	0.01	0.46	0.88	1.45	5.96
Oct-22	2.19	2.76	0.01	0.91	1.55	2.53	41.39
Nov-22	1.38	0.99	0.02	0.64	1.20	1.80	7.11
Dec-22	1.30	0.93	0.07	0.61	1.03	1.69	7.38
Jan-23	1.48	0.90	0.14	0.81	1.27	2.01	5.92
Feb-23	1.54	0.86	0.15	0.92	1.35	1.98	5.29
Mar-23	1.27	0.79	0.17	0.77	1.12	1.52	6.95
Apr-23	1.27	1.20	0.11	0.70	1.05	1.52	22.49
May-23	1.18	0.96	0.10	0.56	1.01	1.48	8.52
Jun-23	1.47	1.77	0.00	0.47	0.92	1.72	22.28
Jul-23	1.34	1.00	0.03	0.68	1.08	1.68	5.92

Table B2. Wildfire occurrence and burning areas (unit: hectare) in Quebec during the last 5 years.

COUNT	**2019**	**2020**	**2021**	**2022**	**2023**
JUNE	58	173	160	22	307
JULY	119	105	37	47	109

TOTAL	177	278	197	69	416
AREA	**2019**	**2020**	**2021**	**2022**	**2023**
JUNE	5000.8	51692.4	10664.8	29282.9	2573724.9
JULY	4549	7338.6	36797.1	77.1	1238908.4
TOTAL	9549.8	59031	47461.9	29360	3812633.3

Table B3. Monthly average concentrations and standard deviations of PM2.5, CO, and O3 in the past 10 years acquired from MERRA-2 reanalysis data.

Year	**2014**	**2015**	**2016**	**2017**	**2018**	**2019**	**2020**	**2021**	**2022**	**2023**
	Monthly average concentrations of $PM_{2.5}$ ($\mu g/m^3$)									
June	8.00	8.97	8.08	8.48	8.42	10.33	9.50	10.30	8.78	39.41
July	11.81	14.37	8.53	9.45	9.68	12.82	10.33	15.11	9.81	17.04
	Standard deviation									
June	4.37	7.36	4.99	3.84	4.08	8.85	4.14	5.56	4.05	80.14
July	6.74	9.76	3.76	5.62	4.73	7.04	5.60	14.60	5.19	13.02
	Comparing with 2022									
June	-9%	2%	-8%	-3%	-4%	18%	8%	17%		349%
July	20%	46%	-13%	-4%	-1%	31%	5%	54%		74%
	Monthly average concentrations of CO (ppbv)									
June	283.50	265.90	246.68	255.95	260.39	278.47	274.17	424.83	483.86	653.82
July	276.79	301.37	264.73	289.87	272.80	293.56	278.82	481.39	453.68	633.16
	Standard deviation									
June	131.50	111.92	110.36	97.08	109.73	140.57	137.90	193.87	256.54	317.16
July	106.36	130.51	110.40	123.57	123.50	130.78	134.60	271.48	238.21	293.68
	Comparing with 2022									
June	-41%	-45%	-49%	-47%	-46%	-42%	-43%	-12%		35%
July	-39%	-34%	-42%	-36%	-40%	-35%	-39%	6%		40%
	Monthly average concentrations of O_3 (DU)									
June	329.68	348.22	337.43	342.40	328.65	354.77	330.61	333.08	340.90	341.19
July	328.63	338.30	322.03	328.72	319.63	322.77	313.05	333.49	335.63	324.16
	Standard deviation									
June	13.66	21.59	22.58	29.25	20.59	25.00	22.62	26.40	27.49	19.93
July	16.44	19.68	19.08	18.06	19.94	20.85	15.78	17.23	16.31	17.58
	Comparing with 2022									
June	-3%	2%	-1%	0%	-4%	4%	-3%	-2%		0%
July	-2%	1%	-4%	-2%	-5%	-4%	-7%	-1%		-3%

Table B4. Averages (with unit of Mm^{-1}) of $B_{abs,\ BC}$ (λ), $B_{abs,\ BrC}$ (λ), $B_{abs,\ BrC\ pri}$ (λ), $B_{abs,\ BrC\ sec}$ (λ), and $B_{abs,\ pri}$ (λ) at different wavelengths. The percentage values for $B_{abs,\ BC}$ (λ) and $B_{abs,\ BrC}$ (λ) indicate proportions of BC and BrC to B_{abs} (λ) respectively. The percentage values for $B_{abs,\ BrC\ pri}$ (λ), $B_{abs,\ BrC\ sec}$ (λ) represent the

proportions of primary BrC and secondary BrC to $B_{abs,\ BrC}$ (λ) respectively. And the percentage values for $B_{abs,\ pri}$ (λ) shows the contribution from primary sources.

	BB dominated				FF dominated			
wavelength	**$B_{abs,\ BC}$ (λ)**	**$B_{abs,\ BrC}$ (λ)**	**$B_{abs,\ BrC\ pri}$ (λ)**	**$B_{abs,\ BrC\ sec}$ (λ)**	**$B_{abs,\ BC}$ (λ)**	**$B_{abs,\ BrC}$ (λ)**	**$B_{abs,\ BrC\ pri}$ (λ)**	**$B_{abs,\ BrC\ sec}$ (λ)**
370	5.42 (46%)	6.39 (54%)	4.93 (77%)	1.46 (23%)	4.42 (81%)	1.04 (19%)	0.95 (91%)	0.09 (9%)
470	4.27 (64%)	2.44 (36%)	1.89 (77%)	0.55 (23%)	3.48 (84%)	0.68 (16%)	0.63 (93%)	0.05 (7%)
520	3.84 (73%)	1.42 (27%)	1.09 (77%)	0.33 (23%)	3.14 (88%)	0.43 (12%)	0.40 (93%)	0.03 (7%)
590	3.40 (80%)	0.80 (20%)	0.61 (76%)	0.19 (24%)	2.77 (91%)	0.26 (9%)	0.24 (92%)	0.02 (8%)
660	3.02 (90%)	0.34 (10%)	0.24 (71%)	0.10 (29%)	2.47 (96%)	0.10 (4%)	0.09 (90%)	0.01 (10%)
880	2.27	0	0	0	1.86	0	0	0
950	2.08	0	0	0	1.73	0	0	0

Appendix C

C Chapter 4 Supplementary Information

C.1 Supplementary figures

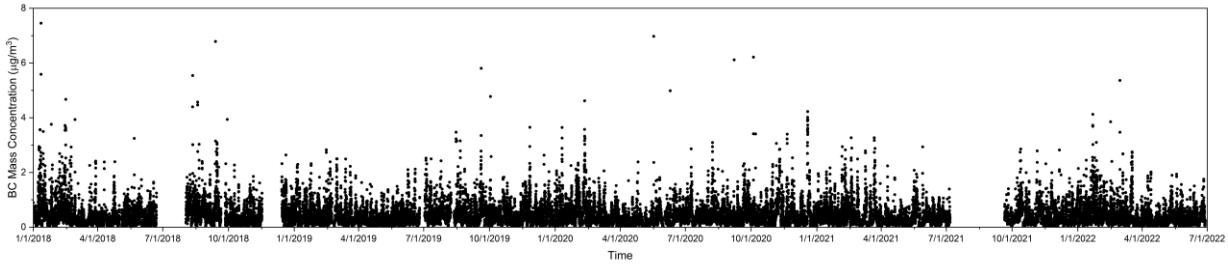

Figure C1. Variation of hourly averages of BC mass concentration during 2018 to 2022.

C.2 Supplementary tables

Table C1. Performance of the model on different subsets. Winter is set from December 1st to April 20th. Summer spans from June 21st to September 20th. Daytime is from 9 am to 6 pm, whereas nighttime is from 10 pm to 5 am.

Period	RMSE	MSE	R^2
All data	0.096	0.009	0.819
Winter	0.083	0.007	0.825
Summer	0.117	0.014	0.789
Day	0.089	0.008	0.809
Night	0.101	0.010	0.829

Chapter 6 Reference

Abegglen, M., Brem, B. T., Ellenrieder, M., Durdina, L., Rindlisbacher, T., Wang, J., et al. (2016), Chemical characterization of freshly emitted particulate matter from aircraft exhaust using single particle mass spectrometry. *Atmospheric Environment*, 134: 181-197. https://doi.org/10.1016/j.atmosenv.2016.03.051

Abu Awad, Y., P. Koutrakis, B. A. Coull, and J. Schwartz (2017), A spatio-temporal prediction model based on support vector machine regression: Ambient Black Carbon in three New England States, *Environ Res*, 159, 427-434, doi:10.1016/j.envres.2017.08.039.

Al-Abadleh, H. A. (2021), Aging of atmospheric aerosols and the role of iron in catalyzing brown carbon formation, *Environmental Science: Atmospheres*, 1(6), 297-345, doi:10.1039/d1ea00038a.

Alberta Wildfire Whitecourt Area Update (2024): https://srd.web.alberta.ca/whitecourt-area-update/2024-feb-26#:~:text=A%20fire%20lit%20in%20the,all%20fires%20are%20completely%20extinguished. Last Access Date: 2024/3/3.

Ariya P. A., Dastoor A., Nazarenko Y., and Amyot, M. (2018), Do snow and ice alter urban air quality? *Atmospheric Environment*, 186, 266–268. https://doi.org/10.1016/j.atmosenv.2018.05.028

Bahadur, R., Praveen, P. S., Xu, Y. & Ramanathan, V. (2012), Solar absorption by elemental and brown carbon determined from spectral observations. *Proceedings of the National Academy of Science of the United States of America*, 109(43): 17366-17371. https://doi.org/10.1073/pnas.1205910109

Bai, Z., W. Wen, W. Zhang, L. Li, L. Wang, and J. Chen (2023), The light absorbing and molecule characteristic of PM(2.5) brown carbon observed in urban Shanghai, *Environ Pollut*, 318, 120874, doi:10.1016/j.envpol.2022.120874.

Bao, R. & Zhang, A. (2020). Does lockdown reduce air pollution? Evidence from 44 cities in northern China. *Science of the Total Environment*, 731: 139052. https://doi.org/10.1016/j.scitotenv.2020.139052

Begam, G. R., Vachaspati, C. V., Ahammed, Y. N., Kumar, K. R., Babu, S. S. & Reddy, R. R. (2016). Measurement and analysis of black carbon aerosols over a tropical semi-arid station in Kadapa, India. *Atmospheric Research*, 171: 77–91. http://dx.doi.org/10.1016/j.atmosres.2015.12.014

Bond, T. C. & Bergstrom, R. W. (2007). Light Absorption by Carbonaceous Particles: An Investigative Review. *Aerosol Science and Technology*, 40(1): 27-67. https://doi.org/10.1080/02786820500421521

Bond, T. C., Doherty, S. J., Fahey, D. W., Forster, P. M., Berntsen, T., DeAngelo, B. J., Flanner, M. G., Ghan, S., Kärcher, B., Koch, D., Kinne, S., Kondo, Y., Quinn, P. K., Sarofim, M. C., Schultz, M. G., Schulz, M., Venkataraman, C., Zhang, H., Zhang, S., Bellouin, N., Guttikunda, S. K., Hopke, P. K., Jacobson, M. Z., Kaiser, J. W., Klimont, Z., Lohmann, U., Schwarz, J. P., Shindell,

D., Storelvmo, T., Warren, S. G., and Zender, C. S.:Bounding the role of black carbon in the climate system: A scientific assessment, *Journal of Geophysical Research: Atmospheres*, 118(11), 5380-5552, doi:10.1002/jgrd.50171, 2013.

Bond, T. C., G. Habib, and R. W. Bergstrom (2006), Limitations in the enhancement of visible light absorption due to mixing state, *Journal of Geophysical Research: Atmospheres*, 111(D20), doi:10.1029/2006jd007315.

Bove, H., Bongaerts, E., Slenders, E., Bijnens, E. M., Saenen, N. D., Gyselaers, W., et al. (2019). Ambient black carbon particles reach the fetal side of human placenta. *Nature Communication*, 10(1): 3866. https://doi.org/10.1038/s41467-019-11654-3

Briz-Redón A., Belenguer-Sapiña C., & Serrano-Aroca A. (2021). Changes in air pollution during COVID-19 lockdown in Spain: A multi-city study. *Journal of Environmental Science*, 101: 16-26. https://doi.org/10.1016/j.jes.2020.07.029

Brooks, S. D., Suter, K., & Olivarez, L. (2014). Effects of chemical aging on the ice nucleation activity of soot and polycyclic aromatic hydrocarbon aerosols. *The Journal of Physical Chemistry A*, 118(43): 10036-10047. https://doi.org/10.1021/jp508809y

Brown, A. C. (2013). Health Effects of Particulates and Black Carbon. U. S. EPA Transport and Clean Air Seminar. Retrieved from https://www.epa.gov/sites/production/files/2014-05/documents/health-effects.pdf

Browne, E. C., X. Zhang, J. P. Franklin, K. J. Ridley, T. W. Kirchstetter, K. R. Wilson, C. D. Cappa, and J. H. Kroll (2019), Effect of heterogeneous oxidative aging on light absorption by biomass burning organic aerosol, *Aerosol Science and Technology*, 53(6), 663-674, doi:10.1080/02786826.2019.1599321.

Cable News Network (CNN) (2023): June 7, 2023 Canada wildfire smoke and US air quality news, https://www.cnn.com/us/live-news/us-air-quality-canadian-wildfires-06-07-23/index.html. Last Access Date: 2024/3/3.

Camero, K. (2019). Aviation's dirty secret: Airplane contrails are a surprisingly potent cause of global warming. *Science*. https://doi:10.1126/science.aay5598

Canadian Wildland Fire Information System (CWFIS) (2023): National Wildland Fire Situation Report, https://cwfis.cfs.nrcan.gc.ca/report. Last Access Date: 2024/3/3.

Canagaratna, M. R., Massoli, P., Browne, E. C., Franklin, J. P., Wilson, K. R., Onasch, T. B., et al. (2015). Chemical Compositions of Black Carbon Particle Cores and Coatings via Soot Particle Aerosol Mass Spectrometry with Photoionization and Electron Ionization. *The Journal of Physical Chemistry A*, 119, 19, 4589-4599. https://doi.org/10.1021/jp510711u

Cappa, C. D., Onasch, T. B., Massoli, P., Worsnop, D. R., Bates, T. S., Cross, E. S., et al. (2012). Radiative Absorption Enhancements Due to the Mixing State of Atmospheric Black Carbon. *Science*, 337 (6098), 1078-1081. https://doi.org/10.1126/science.1223447

Chakrabarty, R. K., Beres, N. D., Moosmuller, H., China, S., Mazzoleni, C., Dubey, M. K., et al. (2014). Soot superaggregates from flaming wildfires and their direct radiative forcing. *Scientific Reports*, 4: 5508. https://doi.org/10.1038/srep05508

Chan, K. M. & Wood, R. (2013). The seasonal cycle of planetary boundary layer depth determined using COSMIC radio occultation data. *Journal of Geophysical Research: Atmospheres*, 118: 12422-12434. https://doi.org/10.1002/2013JD020147

Chen, J., et al. (2021), Atmospheric Humic-Like Substances (HULIS) Act as Ice Active Entities, *Geophysical Research Letters*, 48(14), doi:10.1029/2021gl092443.

Chen, L., Hu, X., Wang, J., & Yu, Y. (2019). Impacts of Alternative Fuels on Morphological and Nanostructural Characteristics of Soot Emissions from an Aviation Piston Engine. *Environmental Science & Technology*, 53(8): 4667-4674. https://doi.org/10.1021/acs.est.9b01059

Cozic, J., S. Mertes, B. Verheggen, D. J. Cziczo, S. J. Gallavardin, S. Walter, U. Baltensperger, and E. Weingartner (2008), Black carbon enrichment in atmospheric ice particle residuals observed in lower tropospheric mixed phase clouds, *Journal of Geophysical Research: Atmospheres*, 113(D15), doi:10.1029/2007jd009266.

De Haan, D. O., et al. (2017), Brown Carbon Production in Ammonium- or Amine-Containing Aerosol Particles by Reactive Uptake of Methylglyoxal and Photolytic Cloud Cycling, *Environ Sci Technol*, 51(13), 7458-7466, doi:10.1021/acs.est.7b00159.

de Oliveira Alves, N., Brito, J., Caumo, S., Arana, A., de Souza Hacon, S., Artaxo, P., et al. (2015). Biomass burning in the Amazon region: Aerosol source apportionment and associated health risk assessment. *Atmospheric Environment*, 120: 277-285. https://doi.org/10.1016/j.atmosenv.2015.08.059

DeMott P. J. (1990). An exploratory study of ice nucleation by soot aerosols. *Journal of Applied Meteorology and Climatology*, 29(10), 1072–1079. https://doi.org/10.1175/1520-0450(1990)029%3C1072:AESOIN%3E2.0.CO;2

DeMott, P. J., A. J. Prenni, X. Liu, S. M. Kreidenweis, M. D. Petters, C. H. Twohy, M. S. Richardson, T. Eidhammer, and D. C. Rogers (2010), Predicting global atmospheric ice nuclei distributions and their impacts on climate, *Proc Natl Acad Sci U S A*, 107(25), 11217-11222, doi:10.1073/pnas.0910818107.

DeMott, P. J., Y. Chen, S. M. Kreidenweis, D. C. Rogers, and D. E. Sherman (1999), Ice formation by black carbon particles, *Geophysical Research Letters*, 26(16), 2429-2432, doi:10.1029/1999gl900580.

Ding, A. J., et al. (2016), Enhanced haze pollution by black carbon in megacities in China, *Geophysical Research Letters*, 43(6), 2873-2879, doi:10.1002/2016gl067745.

DMT Photoacoustic Extinctiometer (PAX) Operator Manual DOC-0301 Revision F (2020), https://www.dropletmeasurement.com/manual/operations-manual-photoaccoustic-extinctiometer-pax/. Last Access Date: 2024/3/3.

Dou, T. F., & Xiao, C. D. (2016). An overview of black carbon deposition and its radiative forcing over the Arctic. *Advances in Climate Change Research*, 7(3): 115-122. https://doi.org/10.1016/j.accre.2016.10.003

Drinovec, L., Mocnik, G., Zotter, P., Prévôt, A. S. H., Ruckstuhl, C., Coz, E., Rupakheti, M., Sciare6, J., Müller, T., Wiedensohler, A., and Hansen, A. D. A.: The "dual-spot" Aethalometer: an improved measurement of aerosol black carbon with real-time loading compensation, *Atmospheric Measurement Techniques*, 8(5), 1965-1979, doi:10.5194/amt-8-1965-2015, 2015.

Eck, T. F., Holben, B. N., Reid, J. S., Sinyuk, A., Giles, D. M., Arola, A., Slutsker, I., Schafer, J. S., Sorokin, M. G., Smirnov, A., LaRosa, A. D., Kraft, J., Reid, E. A., O'Neill, N. T., Welton, E.J., and Menendez, A. R.: The extreme forest fires in California/Oregon in 2020: Aerosol optical and physical properties and comparisons of aged versus fresh smoke, *Atmospheric Environment*, 305, 119798, doi:10.1016/j.atmosenv.2023.119798, 2023.

Elser, M., Brem, B. T., Durdina, L., Schönenberger, D., Siegerist, F., Fischer, A., & Wang, J. (2019). Chemical composition and radiative properties of nascent particulate matter emitted by an aircraft turbofan burning conventional and alternative fuels. *Atmospheric Chemistry and Physics*, 19(10): 6809-6820. https://doi.org/10.5194/acp-19-6809-2019

Eltouny, N.A. & Ariya P. A. (2012). Fe_3O_4 Nanoparticles and Carboxymethyl Cellulose: A Green Option for the Removal of Atmospheric Benzene, Toluene, Ethylbenzene, and o-Xylene (BTEX). *Industrial & Engineering Chemistry Research*, 51(39): 12787-12795.

Fan, C., Li, Z., Li, Y., Dong, J., van der A, R. & de Leeuw, G. (2021). Variability of NO2 concentrations over China and effect on air quality derived from satellite and ground-based observations. *Atmospheric Chemistry and Physics*, 21, 7723-7748. https://doi.org/10.5194/acp-21-7723-2021

Fan, J., Wang, Y., Rosenfeld, D., & Liu, X. (2016). Review of Aerosol–Cloud Interactions: Mechanisms, Significance, and Challenges. *Journal of the Atmospheric Sciences*, 73(11): 4221-4252. https://doi.org/10.1175/JAS-D-16-0037.1

Fang, Z., et al. (2021), Secondary organic aerosols produced from photochemical oxidation of secondarily evaporated biomass burning organic gases: Chemical composition, toxicity, optical properties, and climate effect, Environ Int, 157, 106801, doi:10.1016/j.envint.2021.106801.

Feilberg, A., and Nielsen, T. (2001), Photodegradation of Nitro-PAHs in Viscous Organic Media Used as Models of Organic Aerosols, *Environmental Science & Technology* 2001 35 (1), 108-113, DOI: 10.1021/es990834l.

Feng, Y., V. Ramanathan, and V. R. Kotamarthi (2013), Brown carbon: a significant atmospheric absorber of solar radiation?, *Atmospheric Chemistry and Physics*, 13(17), 8607-8621, doi:10.5194/acp-13-8607-2013.

Finewax, Z., J. A. de Gouw, and P. J. Ziemann (2018), Identification and Quantification of 4-Nitrocatechol Formed from OH and NO(3) Radical-Initiated Reactions of Catechol in Air in the Presence of NO(x): Implications for Secondary Organic Aerosol Formation from Biomass Burning, *Environ Sci Technol*, 52(4), 1981-1989, doi:10.1021/acs.est.7b05864.

Fleming, L. T., N. N. Ali, S. L. Blair, M. Roveretto, C. George, and S. A. Nizkorodov (2019), Formation of Light-Absorbing Organosulfates during Evaporation of Secondary Organic Material Extracts in the Presence of Sulfuric Acid, *ACS Earth and Space Chemistry*, 3(6), 947-957, doi:10.1021/acsearthspacechem.9b00036.

Fung, P. L., et al. (2021), Evaluation of white-box versus black-box machine learning models in estimating ambient black carbon concentration, *Journal of Aerosol Science*, 152, doi:10.1016/j.jaerosci.2020.105694.

Fuzzi, S., Baltensperger, U., Carslaw, K., Decesari, S., Denier van der Gon, H., Facchini, M. C., et al. (2015). Particulate matter, air quality and climate: lessons learned and future needs. *Atmospheric Chemistry and Physics*, 15(14): 8217-8299. https://doi.org/10.5194/acp-15-8217-2015

Ganguly, M., & Ariya, P. A. (2019). Ice Nucleation of Model Nanoplastics and Microplastics: A Novel Synthetic Protocol and the Influence of Particle Capping at Diverse Atmospheric Environments. *ACS Earth and Space Chemistry*, 3, 9, 1729–1739. https://doi.org/10.1021/acsearthspacechem.9b00132

Gautam, S. (2020). COVID-19: air pollution remains low as people stay at home. *Air Quality, Atmosphere & Health*, 13(7): 853-857. https://doi.org/10.1007/s11869-020-00842-6

Géron, A. Hands-On Machine Learning with Scikit-Learn, Keras, and TensorFlow, 2nd ed.; O'Reilly Media: Sebastopol, CA, 2019.

Global Modeling and Assimilation Office (GMAO) (2015) a: MERRA-2 tavg1_2d_aer_Nx: 2d,1-Hourly,Time-averaged,Single-Level,Assimilation,Aerosol Diagnostics V5.12.4, Greenbelt, MD, USA, Goddard Earth Sciences Data and Information Services Center (GES DISC), Accessed: 2024/01/28, 10.5067/KLICLTZ8EM9D.

Global Modeling and Assimilation Office (GMAO) (2015) b: MERRA-2 tavg1_2d_chm_Nx: 2d,1-Hourly,Time-Averaged,Single-Level,Assimilation,Carbon Monoxide and Ozone Diagnostics V5.12.4, Greenbelt, MD, USA, Goddard Earth Sciences Data and Information Services Center (GES DISC), Accessed: 2024/01/28, 10.5067/3RQ5YS674DGQ.

Grandey, B. S., Rothenberg, D., Avramov, A., Jin, Q., Lee, H. H., Liu, X., et al. (2018). Effective radiative forcing in the aerosol–climate model CAM5.3-MARC-ARG. *Atmospheric Chemistry and Physics*, 18(21): 15783-15810. https://doi.org/10.5194/acp-18-15783-2018

Hadley, O. L., Corrigan, C. E., Kirchstetter, T. W., Cliff, S. S., & Ramanathan, V. (2010). Measured black carbon deposition on the Sierra Nevada snow pack and implication for snow pack retreat. *Atmospheric Chemistry and Physics*, 10, 7505–7513. https://doi.org/10.5194/acp-10-7505-2010

Hall, R., Nepotchatykh, O., Nepotchatykh, E., & Ariya, P. A. (2020). Anthropogenic Photolabile Chlorine in the Cold-Climate City of Montreal. *Atmosphere*, 11(8), 812. https://doi.org/10.3390/atmos11080812

Hansen, K. M., Halsall, C. J., & Christensen, J. H. (2006). A Dynamic Model to Study the Exchange of Gas-Phase Persistent Organic Pollutants between Air and a Seasonal Snowpack. *Environmental Science & Technology*, 40, 2644-2652. https://doi.org/10.1021/es051685b

Hawkins, L. N., H. G. Welsh, and M. V. Alexander (2018), Evidence for pyrazine-based chromophores in cloud water mimics containing methylglyoxal and ammonium sulfate, *Atmospheric Chemistry and Physics*, 18(16), 12413-12431, doi:10.5194/acp-18-12413-2018.

Hecobian, A., X. Zhang, M. Zheng, N. Frank, E. S. Edgerton, and R. J. Weber (2010), Water-Soluble Organic Aerosol material and the light-absorption characteristics of aqueous extracts

measured over the Southeastern United States, *Atmospheric Chemistry and Physics*, 10(13), 5965-5977, doi:10.5194/acp-10-5965-2010.

Hems, R. F., E. G. Schnitzler, C. Liu-Kang, C. D. Cappa, and J. P. D. Abbatt (2021), Aging of Atmospheric Brown Carbon Aerosol, *ACS Earth and Space Chemistry*, 5(4), 722-748, doi:10.1021/acsearthspacechem.0c00346.

Hems, R. F., E. G. Schnitzler, M. Bastawrous, R. Soong, A. J. Simpson, and J. P. D. Abbatt (2020), Aqueous Photoreactions of Wood Smoke Brown Carbon, *ACS Earth and Space Chemistry*, 4(7), 1149-1160, doi:10.1021/acsearthspacechem.0c00117.

Henry, K. M., and N. M. Donahue (2012), Photochemical aging of alpha-pinene secondary organic aerosol: effects of OH radical sources and photolysis, *J Phys Chem A*, 116(24), 5932-5940, doi:10.1021/jp210288s.

Hong, Y., F. Cao, M.-Y. Fan, Y.-C. Lin, M. Bao, Y. Xue, J. Wu, M. Yu, X. Wu, and Y.-L. Zhang (2022), Using machine learning to quantify sources of light-absorbing water-soluble humic-like substances (HULISws) in Northeast China, *Atmos Environ*, 291, doi:10.1016/j.atmosenv.2022.119371.

Huang, X., Ding, A., Gao, J., Zheng, B., Zhou, D., Qi, X., Tang, R., Wang, J., Ren, C., Nie, W., Chi, X., Xu, Z., Chen, L., Li, Y., Che, F., Pang, N., Wang, H., Tong, D., Qin, W., Cheng, W., Liu, W., Fu, Q., Liu, B., Chai, F., Davis, S. J., Zhang, Q., and He, K.: Enhanced secondary pollution offset reduction of primary emissions during COVID-19 lockdown in China, *National Science Review*, 8(2), doi: 10.1093/nsr/nwaa137, 2021.

Hudson, E. D., & Ariya, P. A. (2007). Measurements of non-methane hydrocarbons, DOC in surface ocean waters and aerosols over the Nordic seas during polarstern cruise ARK-XX/1 (2004). *Chemosphere*, 69 (9), 1474-1484. https://doi.org/10.1016/j.chemosphere.2007.04.056

Ikhenazene, R., C. Pirim, J. A. Noble, C. Irimiea, Y. Carpentier, I. K. Ortega, F.-X. Ouf, C. Focsa, and B. Chazallon (2019), Ice Nucleation Activities of Carbon-Bearing Materials in Deposition Mode: From Graphite to Airplane Soot Surrogates, The Journal of Physical Chemistry C, 124(1), 489-503, doi:10.1021/acs.jpcc.9b08715.

Intergovernmental Panel on Climate Change (IPCC): Climate change 2013: The physical science basis. Contribution of working group I to the fifth assessment report of the intergovernmental panel on climate change (p. 1535). Cambridge University Press, 2013.

International Civil Aviation Organization (ICAO, 2016). *Environmental Report 2016: Aviation and Climate Change*. Retrieved from https://www.icao.int/environmental-protection/Documents/ICAO%20Environmental%20Report%202016.pdf

International Civil Aviation Organization (ICAO, 2021). *Economic Impacts of COVID-19 on Civil Aviation*. Retrieved from https://www.icao.int/sustainability/Documents/COVID-19/ICAO_Coronavirus_Econ_Impact.pdf

IPCC (2014). *Climate Change 2014: Synthesis Report. Contribution of Working Groups I, II and III to the Fifth Assessment Report of the Intergovernmental Panel on Climate Change* [Core Writing Team, Pachauri, R.K., & Meyer, L.A. (eds.)]. IPCC, Geneva, Switzerland, 151 pp.

IPCC (2021). Climate Change 2021: The Physical Science Basis. Contribution of Working Group I to the Sixth Assessment Report of the Intergovernmental Panel on Climate Change [Masson-Delmotte, V., P. Zhai, A. Pirani, S.L. Connors, C. Péan, S. Berger, N. Caud, Y. Chen, L. Goldfarb, M.I. Gomis, M. Huang, K. Leitzell, E. Lonnoy, J.B.R. Matthews, T.K. Maycock, T. Waterfield, O. Yelekçi, R. Yu, and B. Zhou (eds.)]. Cambridge University Press, Cambridge, United Kingdom and New York, NY, USA, 2391 pp. doi:10.1017/9781009157896.

IUPAC (2023). IUPAC announces the 2023 top ten emerging technologies in chemistry. https://iupac.org/iupac-2023-top-ten/.

Järvi, L., Grimmond, C. S. B., Taka, M., Nordbo, A., Setälä, H., & Strachan, I.B. (2014). Development of the surface urban energy and water balance scheme (SUEWS) for cold climate cities. *Geoscientific Model Development*, 7, 1691–1711. https://doi.org/10.5194/gmd-7-1691-2014

Jia, S., Zhang, Q., Sarkar, S., Mao, J., Hang, J., Chen, W., et al. (2020). Size-segregated deposition of atmospheric elemental carbon (EC) in the human respiratory system: A case study of the Pearl River Delta, China. *Science of the Total Environment*, 708: 134932. https://doi.org/10.1016/j.scitotenv.2019.134932

Jiang, H., J. Li, R. Sun, C. Tian, J. Tang, B. Jiang, Y. Liao, C. E. Chen, and G. Zhang (2021), Molecular Dynamics and Light Absorption Properties of Atmospheric Dissolved Organic Matter, *Environ Sci Technol*, 55(15), 10268-10279, doi:10.1021/acs.est.1c01770.

Jiang, W., Ma, L., Niedek, C., Anastasio, C., and Zhang Q.: Chemical and Light-Absorption Properties of Water-Soluble Organic Aerosols in Northern California and Photooxidant Production by Brown Carbon Components, *ACS Earth Space Chem*, 7(5), 1107-1119, doi:10.1021/acsearthspacechem.3c00022, 2023.

Jo, D. S., R. J. Park, S. Lee, S.-W. Kim, and X. Zhang (2016), A global simulation of brown carbon: implications for photochemistry and direct radiative effect, *Atmospheric Chemistry and Physics*, 16(5), 3413-3432, doi:10.5194/acp-16-3413-2016.

Jolly, W. M., Cochrane, M. A., Freeborn, P. H., Holden, Z. A., Brown, T. J., Williamson, G. J., and Bowman, D. M.: Climate-induced variations in global wildfire danger from 1979 to 2013, *Nat Commun*, 6, 7537, doi:10.1038/ncomms8537, 2015.

Kamphus, M., M. Ettner-Mahl, T. Klimach, F. Drewnick, L. Keller, D. J. Cziczo, S. Mertes, S. Borrmann, and J. Curtius (2010), Chemical composition of ambient aerosol, ice residues and cloud droplet residues in mixed-phase clouds: single particle analysis during the Cloud and Aerosol Characterization Experiment (CLACE 6), *Atmospheric Chemistry and Physics*, 10(16), 8077-8095, doi:10.5194/acp-10-8077-2010.

Kanniah, K. D., Zaman, N. A. F. K., Kaskaoutis, D. G., & Latif, M. T. (2020). COVID-19's impact on the atmospheric environment in the Southeast Asia region. *Science of the Total Environment*, 736: 139658. https://doi.org/10.1016/j.scitotenv.2020.139658

Kitanovski, Z., J. Hovorka, J. Kuta, C. Leoni, R. Prokes, O. Sanka, P. Shahpoury, and G. Lammel (2021), Nitrated monoaromatic hydrocarbons (nitrophenols, nitrocatechols, nitrosalicylic acids) in ambient air: levels, mass size distributions and inhalation bioaccessibility, *Environ Sci Pollut Res Int*, 28(42), 59131-59140, doi:10.1007/s11356-020-09540-3.

Knopf, D. A., P. A. Alpert, and B. Wang (2018), The Role of Organic Aerosol in Atmospheric Ice Nucleation: A Review, *ACS Earth and Space Chemistry*, 2(3), 168-202, doi:10.1021/acsearthspacechem.7b00120.

Kuang, Y., J. Shang, M. Sheng, X. Shi, J. Zhu, and X. Qiu (2023), Molecular Composition of Beijing PM(2.5) Brown Carbon Revealed by an Untargeted Approach Based on Gas Chromatography and Time-of-Flight Mass Spectrometry, *Environ Sci Technol*, 57(2), 909-919, doi:10.1021/acs.est.2c05918.

Kulkarni, G., China, S., Liu, S., Nandasiri, M., Sharma, N., Wilson, J., et al. (2016). Ice nucleation activity of diesel soot particles at cirrus relevant temperature conditions: Effects of hydration, secondary organics coating, soot morphology, and coagulation. *Geophysical Research Letters*, 43(7): 3580-3588. https://doi.org/10.1002/2016GL068707

Kupiszewski, P., et al. (2016), Ice residual properties in mixed-phase clouds at the high-alpine Jungfraujoch site, *J Geophys Res Atmos*, 121(20), 12343-12362, doi:10.1002/2016JD024894.

Kuwata, M., S. R. Zorn, and S. T. Martin (2012), Using elemental ratios to predict the density of organic material composed of carbon, hydrogen, and oxygen, *Environ Sci Technol*, 46(2), 787-794, doi:10.1021/es202525q.

Lack, D. A., Moosmuller, H., McMeeking, G. R., Chakrabarty, R. K., & Baumgardner, D. (2014). Characterizing elemental, equivalent black, and refractory black carbon aerosol particles: a review of techniques, their limitations and uncertainties. *Analytical and Bioanalytical Chemistry*, 406(1): 99-122. https://doi.org/10.1007/s00216-013-7402-3.

Laskin, A., Laskin, J., and Nizkorodov, S. A. (2015). Chemistry of atmospheric brown carbon, *Chem Rev*, 115(10), 4335-4382, doi:10.1021/cr5006167.

Lee, J. D., Drysdale, W. S., Finch, D. P., Wilde, S. E., & Palmer, P. I. (2020). UK surface NO_2 levels dropped by 42 % during the COVID-19 lockdown: impact on surface O_3. *Atmospheric Chemistry and Physics*, 20, 15743–15759. https://doi.org/10.5194/acp-20-15743-2020

Lee, J. E., K. Gorkowski, A. G. Meyer, K. B. Benedict, A. C. Aiken, and M. K. Dubey (2022), Wildfire Smoke Demonstrates Significant and Predictable Black Carbon Light Absorption Enhancements, *Geophysical Research Letters*, 49(14), doi:10.1029/2022gl099334.

Lei, Y. D. & Wania, F. (2004). Is rain or snow a more efficient scavenger of organic chemicals? *Atmospheric Environment*, 38, 3557–3571. https://doi.org/10.1016/j.atmosenv.2004.03.039

Lei, Y., Zhang, K., Lu, Y., Qin, Y., Li, L., Li, J., Liu, X., Wu, C., Zhang, S., Chen, Y., Zhang, J., Zhang, F., and Wang, G.: Characterization of water-soluble brown carbon in atmospheric fine particles over Xi'an, China: Implication of aqueous brown carbon formation from biomass burning, *Sci Total Environ*, 881, 163442, doi:10.1016/j.scitotenv.2023.163442, 2023.

Lenssen, E. S., R. H. H. Pieters, S. M. Nijmeijer, M. Oldenwening, K. Meliefste, and G. Hoek (2022), Short-term associations between barbecue fumes and respiratory health in young adults, *Environ Res*, 204(Pt A), 111868, doi:10.1016/j.envres.2021.111868.

Lepisto, T., Barreira, L. M. F., Helin, A., Niemi, J. V., Kuittinen, N., Lintusaari, H., Silvonen, V., Markkula, L., Manninen, H. E., Timonen, H., Jalava, P., Saarikoski, S., and Rönkkö, T.: Snapshots of wintertime urban aerosol characteristics: Local sources emphasized in ultrafine

particle number and lung deposited surface area, *Environ Res*, 231(Pt 1), 116068, doi:10.1016/j.envres.2023.116068, 2023.

Li, C., et al. (2020), Formation of Secondary Brown Carbon in Biomass Burning Aerosol Proxies through NO(3) Radical Reactions, *Environ Sci Technol*, 54(3), 1395-1405, doi:10.1021/acs.est.9b05641.

Li, H. and Ariya, P. A.: Black Carbon Particles Physicochemical Real-Time Data Set in a Cold City: Trends of Fall-Winter BC Accumulation and COVID-19, *J Geophys Res Atmos*, 126(22), e2021JD035265, doi:10.1029/2021JD035265, 2021.

Li, W., N. Riemer, L. Xu, Y. Wang, K. Adachi, Z. Shi, D. Zhang, Z. Zheng, and A. Laskin (2024), Microphysical properties of atmospheric soot and organic particles: measurements, modeling, and impacts, *npj Climate and Atmospheric Science*, 7(1), doi:10.1038/s41612-024-00610-8.

Li, Z., J. Guo, A. Ding, H. Liao, J. Liu, Y. Sun, T. Wang, H. Xue, H. Zhang, and B. Zhu (2017), Aerosol and boundary-layer interactions and impact on air quality, *Natl Sci Rev*, 4(6), 810-833, doi:10.1093/nsr/nwx117.

Liakakou, E., Stavroulas, I., Kaskaoutis, D. G., Grivas, G., Paraskevopoulou D., Dumka, U. C., et al. (2020). Long-term variability, source apportionment and spectral properties of black carbon at an urban background site in Athens, Greece. *Atmospheric Environment*, 222: 117137. https://doi.org/10.1016/j.atmosenv.2019.117137

Lian, X., Huang, J., Huang, R., Liu, C., Wang, L., & Zhang, T. (2020). Impact of city lockdown on the air quality of COVID-19-hit of Wuhan city. *Science of the Total Environment*, 742: 140556. https://doi.org/10.1016/j.scitotenv.2020.140556

Liu, D., C. He, J. P. Schwarz, and X. Wang (2020), Lifecycle of light-absorbing carbonaceous aerosols in the atmosphere, *npj Climate and Atmospheric Science*, 3(1), doi:10.1038/s41612-020-00145-8.

Liu, H., Wang, Q., Ye, J., Su, X., Zhang, T., Zhang, Y., et al. : Changes in source-specific black carbon aerosol and the induced radiative effects due to the COVID-19 lockdown. Geophysical Research Letters, 48, e2021GL092987, doi: 10.1029/2021GL092987, 2021.

Liu, L., Lin, Y., Min, K., Xiao, K., Di, Y., Peng, L., Zhang, W., Long, Q., Liu, Q., and Jiang, G. (2023): Detection of Ambient Black Carbon in Conjunctival Sac Washed Fluid Reveals the Ocular Exposure Risks of Particulate Pollution, *Environmental Science & Technology Letters*, doi:10.1021/acs.estlett.3c00388.

Liu, Q., Harris, J. T., Chiu, L. S., Sun, D., Houser, P. R., Yu, M., et al. (2021). Spatiotemporal impacts of COVID-19 on air pollution in California, USA. *Science of the Total Environment*, 750: 141592. https://doi.org/10.1016/j.scitotenv.2020.141592

Liu, Q., Sha, D., Liu, W., Houser, P., Zhang, L., Hou, R., et al. (2020). Spatiotemporal Patterns of COVID-19 Impact on Human Activities and Environment in Mainland China Using Nighttime Light and Air Quality Data. *Remote Sensing*, 12(10), 1576. https://doi.org/10.3390/rs12101576

Liu, X., D. Lu, A. Zhang, Q. Liu, and G. Jiang (2022), Data-Driven Machine Learning in Environmental Pollution: Gains and Problems, *Environ Sci Technol*, 56(4), 2124-2133, doi:10.1021/acs.est.1c06157.

Liu-Kang, C., P. J. Gallimore, T. Liu, and J. P. D. Abbatt (2022), Photoreaction of biomass burning brown carbon aerosol particles, *Environmental Science: Atmospheres*, 2(2), 270-278, doi:10.1039/d1ea00088h.

Long, C. M., Nascarella, M. A., & Valberg, P. A. (2013). Carbon black vs. black carbon and other airborne materials containing elemental carbon: physical and chemical distinctions. *Environmental Pollution*, 181: 271-286. https://doi.org/10.1016/j.envpol.2013.06.009

Magee Scientific Aethalometer® Model AE43 User Manual, Version 1.02, July 2021.

Mahato S., Pal, S., & Ghosh, K. G. (2020). Effect of lockdown amid COVID-19 pandemic on air quality of the megacity Delhi, India. *Science of the Total Environment*, 730: 139086. https://doi.org/10.1016/j.scitotenv.2020.139086

Mahrt, F., P. A. Alpert, J. Dou, P. Gronquist, P. C. Arroyo, M. Ammann, U. Lohmann, and Z. A. Kanji (2020), Aging induced changes in ice nucleation activity of combustion aerosol as determined by near edge X-ray absorption fine structure (NEXAFS) spectroscopy, *Environ Sci Process Impacts*, 22(4), 895-907, doi:10.1039/c9em00525k.

Malavelle, F. F., Haywood, J. M., Mercado, L. M., Folberth, G. A., Bellouin, N., Sitch, S., & Artaxo, P. (2019). Studying the impact of biomass burning aerosol radiative and climate effects on the Amazon rainforest productivity with an Earth system model. *Atmospheric Chemistry and Physics*, 19(2): 1301-1326. https://doi.org/10.5194/acp-19-1301-2019

Mandal, I., & Pal, S. (2020). COVID-19 pandemic persuaded lockdown effects on environment over stone quarrying and crushing areas. *Science of the Total Environment*, 732: 139281. https://doi.org/10.1016/j.scitotenv.2020.139281

Mazaheri M., Johnson, G. R., & Morawska, L. (2011). An inventory of particle and gaseous emissions from large aircraft thrust engine operations at an airport. *Atmospheric Environment*, 45, 3500–3507. https://doi.org/10.1016/j.atmosenv.2010.12.012

Meng, L., Hao, w., Zhao, C., Li, S., Xue, J., Li, J., Tu, L., Huang, T., Yang, H., Yu, Z., Yuan, L., and Huang, C.: Anthropogenic Activities Generate High-Refractory Black Carbon along the Yangtze River Continuum, Environmental Science & Technology, 57 (23), 8598-8609, doi: 10.1021/acs.est.2c09827, 2023.

Mbengue, S., Serfozo, N., Schwarz, J., Zikova, N., Smejkalova, A. H., & Holoubek, I. (2020). Characterization of Equivalent Black Carbon at a regional background site in Central Europe: Variability and source apportionment. *Environmental Pollution*, 260: 113771. https://doi.org/10.1016/j.envpol.2019.113771

McCluskey, C. S., DeMott, P. J., Prenni, A. J., Levin, E. J. T., McMeeking, G. R., Sullivan, A. P., et al. (2014). Characteristics of atmospheric ice nucleating particles associated with biomass burning in the US: Prescribed burns and wildfires. *Journal of Geophysical Research: Atmospheres*, 119(17): 10458-10470. https://doi.org/10.1002/2014JD021980

Men, Y., Y. Li, Z. Luo, K. Jiang, F. Yi, X. Liu, R. Xing, H. Cheng, G. Shen, and S. Tao (2023), Interpreting Highly Variable Indoor PM(2.5) in Rural North China Using Machine Learning, *Environ Sci Technol*, 57(46), 18183-18192, doi:10.1021/acs.est.3c02014.

Ming, J., & Wang, F. (2021), Microplastics' hidden contribution to snow melting. *Eos*, 102. https://doi.org/10.1029/2021EO155631

Moise, T., J. M. Flores, and Y. Rudich (2015), Optical properties of secondary organic aerosols and their changes by chemical processes, *Chem Rev*, 115(10), 4400-4439, doi:10.1021/cr5005259.

Morawska, L., et al. (2021), The state of science on severe air pollution episodes: Quantitative and qualitative analysis, *Environ Int*, 156, 106732, doi:10.1016/j.envint.2021.106732.

Munoz-Alpizar, R., Pavlovic, R., Moran, M., Chen, J., Gravel, S., Henderson, S., et al. (2017). Multi-Year (2013–2016) PM2.5 Wildfire Pollution Exposure over North America as Determined from Operational Air Quality Forecasts. *Atmosphere*, 8(9), 179. https://doi.org/10.3390/atmos8090179

Murray, B. J., O'Sullivan, D., Atkinson, J. D., & Webb, M. E. (2012). Ice nucleation by particles immersed in supercooled cloud droplets. *Chemical Society Reviews*, 41(19): 6519-6554. https://doi.org/10.1039/C2CS35200A

Myhre, G., et al. (2013), Radiative forcing of the direct aerosol effect from AeroCom Phase II simulations, *Atmospheric Chemistry and Physics*, 13(4), 1853-1877, doi:10.5194/acp-13-1853-2013.

Nair, A. A., and F. Q. Yu (2020), Using machine learning to derive cloud condensation nuclei number concentrations from commonly available measurements, *Atmospheric Chemistry and Physics*, 20(21), 12853-12869, doi:10.5194/acp-20-12853-2020.

Nakada, L. Y. K., & Urban, R. C. (2020). COVID-19 pandemic: Impacts on the air quality during the partial lockdown in Sao Paulo state, Brazil. *Science of the Total Environment*,730: 139087. https://doi.org/10.1016/j.scitotenv.2020.139087

Nakayama, T., Ikeda, Y., Sawada, Y., Setoguchi, Y., Ogawa, S., Kawana, K., et al. (2014). Properties of light-absorbing aerosols in the Nagoya urban area, Japan, in August 2011 and January 2012: Contributions of brown carbon and lensing effect. *Journal of Geophysical Research: Atmospheres*, 119(22): 12721-12739. https://doi.org/10.1002/2014JD021744

National Air Pollution Surveillance program (NAPS, 2021) https://www.canada.ca/en/environment-climate-change/services/air-pollution/monitoring-networks-data/national-air-pollution-program.html

Nazarenko, Y., Fournier, S., Kurien, U., Rangel-Alvarado, R. B., Nepotchatykh, O., Seers, P., & Ariya, P. A. (2017). Role of snow in the fate of gaseous and particulate exhaust pollutants from gasoline-powered vehicles. *Environmental Pollution*, 223: 665-675. https://doi.org/10.1016/j.envpol.2017.01.082

Nazarenko, Y., Kurien, U., Nepotchatykh, O., Rangel-Alvarado, R. B., & Ariya, P. A. (2016). Role of snow and cold environment in the fate and effects of nanoparticles and select organic pollutants from gasoline engine exhaust. *Environmental Science: Processes & Impacts*, 18, 190-199. https://doi.org/10.1039/C5EM00616C

Pal, D., Dastoor, A., & Ariya, P.A. (2020). Aerosols in an urban cold climate: Physical and chemical characteristics of nanoparticles. *Urban Climate*, 34: 100713. https://doi.org/10.1016/j.uclim.2020.100713

Pang, H., Q. Zhang, X. Lu, K. Li, H. Chen, J. Chen, X. Yang, Y. Ma, J. Ma, and C. Huang (2019), Nitrite-Mediated Photooxidation of Vanillin in the Atmospheric Aqueous Phase, *Environ Sci Technol*, 53(24), 14253-14263, doi:10.1021/acs.est.9b03649.

Parent, P., Laffon, C., Marhaba, I., Ferry, D., Regier, T. Z., Ortega, I. K., et al. (2016). Nanoscale characterization of aircraft soot: A high-resolution transmission electron microscopy, Raman spectroscopy, X-ray photoelectron and near-edge X-ray absorption spectroscopy study. *Carbon*, 101: 86-100. https://doi.org/10.1016/j.carbon.2016.01.040

Park, H., Jeong, S., Koo, J. H., Sim, S., Bae, Y., Kim, Y., et al. (2021). Lessons from COVID-19 and Seoul: Effects of Reduced Human Activity from Social Distancing on Urban CO_2 Concentration and Air Quality. *Aerosol and Air Quality Research*, 21, 200376. https://doi.org/10.4209/aaqr.2020.07.0376

Peng, J., Hua, M., Guo, S., Du, Z., Zheng, J., Shang, D., Zamora, M. L., Zeng, L. , Shao, M., Wu, Y., Zheng, J., Wang, Y., Glenb, C. R., Collinsb, D. R., Molinad, M. J., and Zhang, R.: Markedly enhanced absorption and direct radiative forcing of black carbon under polluted urban environments, Proceedings of the National Academy of Sciences, 113(16), 4266-4271, doi:10.1073/pnas.1602310113, 2016.

Perrino, C. and Marcovecchio, F.: A new method for assessing the contribution of Primary Biological Atmospheric Particles to the mass concentration of the atmospheric aerosol, Environ Int, 87, 108-115, doi:10.1016/j.envint.2015.11.015, 2016.

Petters, M. D., Parsons, M. T., Prenni, A. J., DeMott, P. J., Kreidenweis, S. M., Carrico, C. M., et al. (2009). Ice nuclei emissions from biomass burning. *Journal of Geophysical Research: Atmospheres*, 114(D07209). https://doi.org/10.1029/2008JD011532

Pilania, G., C. N. Iverson, T. Lookman, and B. L. Marrone (2019), Machine-Learning-Based Predictive Modeling of Glass Transition Temperatures: A Case of Polyhydroxyalkanoate Homopolymers and Copolymers, J Chem Inf Model, 59(12), 5013-5025, doi:10.1021/acs.jcim.9b00807.

Putaud, J-P., Pozzoli, L., Pisoni, E., Santos, S. M. D., Lagler, F., Lanzani, G., et al. (2021). Impact of the COVID-19 lockdown on air pollution at regional and urban background sites in northern Italy. *Atmospheric Chemistry and Physics*, 21, 7597-7609. https://doi.org/10.5194/acp-21-7597-2021

Qian, Y., Yasunari, T. J., Doherty, S. J., Flanner, M. G., Lau, W. K. M., Ming, J., et al. (2014). Light-absorbing particles in snow and ice: Measurement and modeling of climatic and hydrological impact. *Advances in Atmospheric Sciences*, 32: 64-91. https://doi.org/10.1007/s00376-014-0010-0

Rahim, M. F., Pal, D., & Ariya, P. A. (2019). Physicochemical studies of aerosols at Montreal Trudeau Airport: The importance of airborne nanoparticles containing metal contaminants. *Environmental Pollution*, 246: 734-744. https://doi.org/10.1016/j.envpol.2018.12.050

Rangel-Alvarado, R. B., Nazarenko, Y., & Ariya, P. A. (2015), Snow-borne nanosized particles: Abundance, distribution, composition, and significance in ice nucleation processes. *Journal of Geophysical Research: Atmospheres*, 120, 11760-11774. https://doi.org/10.1002/2015JD023773

Rangel-Alvarado, R. B., Willis, C. E., Kirk, J. L., St Louis, V. L., Amyot, M., Belanger, D. & Ariya, P. A. (2019). Athabasca oil sands region snow contains efficient micron and nano-sized ice nucleating particles. *Environmental Pollution*, 252(Pt A): 289-295. https://doi.org/10.1016/j.envpol.2019.05.105

Rangel-Alvaraz, R., Willis, C., St-Louis, V., Amyot, M., and Ariya, P.A.: Athabasca Oil Sands Region Snow Contains Efficient Micron and Nano-sized Ice Nucleating Particles, Environmental Pollution, 252, 289-295, doi: 10.1016/j.envpol.2019.05.105, 2019.

Rasking, L., Koshy, P., Bongaerts, E., Bove, H., Ameloot, M., Plusquin, M., De Vusser, K., and Nawrot T. S.: Ambient black carbon reaches the kidneys, Environ Int, 177, 107997, doi:10.1016/j.envint.2023.107997, 2023.

Rivas, I., Beddows, D. C. S., Amato, F., Green, D. C., Jarvi, L., Hueglin, C., et al. (2020). Source apportionment of particle number size distribution in urban background and traffic stations in four European cities. *Environmental International*, 135: 105345. https://doi.org/10.1016/j.envint.2019.105345

Rolph, G., Stein, A. & Stunder, B. (2017). Real-time Environmental Applications and Display sYstem: READY. *Environmental Modelling & Software,* 95, 210-228. https://doi.org/10.1016/j.envsoft.2017.06.025

Rovira, J., J. A. Paredes-Ahumada, J. M. Barcelo-Ordinas, J. Garcia-Vidal, C. Reche, Y. Sola, P. L. Fung, T. Petaja, T. Hussein, and M. Viana (2022), Non-linear models for black carbon exposure modelling using air pollution datasets, Environ Res, 212(Pt B), 113269, doi:10.1016/j.envres.2022.113269.

Hochreiter S., and Schmidhuber, J., Long Short-Term Memory, Neural Computation, vol. 9, no. 8, pp. 1735-1780, 15 Nov. 1997, doi: 10.1162/neco.1997.9.8.1735.

Saleh, R. (2020), From Measurements to Models: Toward Accurate Representation of Brown Carbon in Climate Calculations, Current Pollution Reports, 6(2), 90-104, doi:10.1007/s40726-020-00139-3.

Saleh, R., M. Marks, J. Heo, P. J. Adams, N. M. Donahue, and A. L. Robinson (2015), Contribution of brown carbon and lensing to the direct radiative effect of carbonaceous aerosols from biomass and biofuel burning emissions, Journal of Geophysical Research: Atmospheres, 120(19), doi:10.1002/2015jd023697.

Samburova, V., J. Connolly, M. Gyawali, R. L. N. Yatavelli, A. C. Watts, R. K. Chakrabarty, B. Zielinska, H. Moosmuller, and A. Khlystov (2016), Polycyclic aromatic hydrocarbons in biomass-burning emissions and their contribution to light absorption and aerosol toxicity, Sci Total Environ, 568, 391-401, doi:10.1016/j.scitotenv.2016.06.026.

Sareen, N., S. G. Moussa, and V. F. McNeill (2013), Photochemical aging of light-absorbing secondary organic aerosol material, J Phys Chem A, 117(14), 2987-2996, doi:10.1021/jp309413j.

Sedlacek, A. J., Lewis, E. R., Onasch, T. B., Zuidema, P., Redemann, J., Jaffe, D., and Kleinman, L. I.: Using the Black Carbon Particle Mixing State to Characterize the Lifecycle of Biomass Burning Aerosols, Environmental Science & Technology, 56(20), 14315-14325, doi:10.1021/acs.est.2c03851, 2022.

Selimovic, V., Yokelson, R. J., McMeeking, G. R., & Coefield, S. (2019). In situ measurements of trace gases, PM, and aerosol optical properties during the 2017 NW US wildfire smoke event. *Atmospheric Chemistry and Physics*, 19(6): 3905-3926. https://doi.org/10.5194/acp-19-3905-2019

Shu, Z., C. Huang, K. Min, C. Long, L. Liu, J. Tan, Q. Liu, and G. Jiang (2023), Analysis of black carbon in environmental and biological media: Recent progresses and challenges, TrAC Trends in Analytical Chemistry, 169, doi:10.1016/j.trac.2023.117347.

Société de protection des forêts contre le feu (SOPFEU) 2024: https://sopfeu.qc.ca/en/statistics/. Last Access Date: 2024/3/3.

Soleimanian, E., A. Mousavi, S. Taghvaee, M. M. Shafer, and C. Sioutas (2020), Impact of secondary and primary particulate matter (PM) sources on the enhanced light absorption by brown carbon (BrC) particles in central Los Angeles, Sci Total Environ, 705, 135902, doi:10.1016/j.scitotenv.2019.135902.

Stangl, C. M., and M. V. Johnston (2017), Aqueous Reaction of Dicarbonyls with Ammonia as a Potential Source of Organic Nitrogen in Airborne Nanoparticles, J Phys Chem A, 121(19), 3720-3727, doi:10.1021/acs.jpca.7b02464.

Stein, A. F., Draxler, R. R., Rolph, G. D., Stunder, B. J. B., Cohen, M. D. & Ngan, F. (2015). NOAA's HYSPLIT atmospheric transport and dispersion modeling system. *Bulletin of the American Meteorological Society*, 96, 2059-2077. https://doi.org/10.1175/BAMS-D-14-00110.1

Sumlin, B. J., A. Pandey, M. J. Walker, R. S. Pattison, B. J. Williams, and R. K. Chakrabarty (2017), Atmospheric Photooxidation Diminishes Light Absorption by Primary Brown Carbon Aerosol from Biomass Burning, Environmental Science & Technology Letters, 4(12), 540-545, doi:10.1021/acs.estlett.7b00393.

Sun, Y., L. Lu, Y. K. Cai, and P. Lee (2022), Prediction of black carbon in marine engines and correlation analysis of model characteristics based on multiple machine learning algorithms, Environ Sci Pollut Res Int, 29(52), 78509-78525, doi:10.1007/s11356-022-20496-4.

Tan, Y., Wang, H., Shi, S., Shen, L., Zhang, C., Zhu, B., et al. (2020). Annual variations of black carbon over the Yangtze River Delta from 2015 to 2018. *Journal of Environmental Science*, 96: 72-84. https://doi.org/10.1016/j.jes.2020.04.019

Tasoglou, A., Louvaris, E., Florou, K., Liangou, A., Karnezi, E., Kaltsonoudis, C.,Wang, N., and Pandis, S. N.: Aerosol light absorption and the role of extremely low volatility organic

compounds, Atmospheric Chemistry and Physics, 20(19), 11625-11637, doi:10.5194/acp-20-11625-2020, 2020.

Thornburg, J., Y. Halchenko, M. McCombs, N. Siripanichgon, E. Dowell, S. H. Cho, J. Egner, V. Sayarath, and M. R. Karagas (2021), Children's Particulate Matter Exposure Characterization as Part of the New Hampshire Birth Cohort Study, Int J Environ Res Public Health, 18(22), doi:10.3390/ijerph182212109.

Thornhill, G. D., et al. (2021), Effective radiative forcing from emissions of reactive gases and aerosols – a multi-model comparison, Atmospheric Chemistry and Physics, 21(2), 853-874, doi:10.5194/acp-21-853-2021.

Tsai, Y.-T., Y.-R. Zeng, and Y.-S. Chang (2018), Air Pollution Forecasting Using RNN with LSTM, in 2018 IEEE 16th Intl Conf on Dependable, Autonomic and Secure Computing, 16th Intl Conf on Pervasive Intelligence and Computing, 4th Intl Conf on Big Data Intelligence and Computing and Cyber Science and Technology Congress(DASC/PiCom/DataCom/CyberSciTech), edited, pp. 1074-1079, doi:10.1109/DASC/PiCom/DataCom/CyberSciTec.2018.00178.

Vergara-Temprado, J., Holden, M. A., Orton, T. R., O'Sullivan, D., Umo, N. S., Browse, J., et al. (2018). Is Black Carbon an Unimportant Ice-Nucleating Particle in Mixed-Phase Clouds? *Journal of Geophysical Research: Atmospheres*, 123(8): 4273-4283. https://doi.org/10.1002/2017JD027831

Vidović, K., A. Kroflič, M. Šala, and I. Grgić (2020), Aqueous-Phase Brown Carbon Formation from Aromatic Precursors under Sunlight Conditions, Atmosphere, 11(2), doi:10.3390/atmos11020131.

Vivanco-Hidalgo, R. M., et al. (2018), Short-term exposure to traffic-related air pollution and ischemic stroke onset in Barcelona, Spain, Environ Res, 162, 160-165, doi:10.1016/j.envres.2017.12.024.

von Schneidemesser, E., et al. (2015), Chemistry and the Linkages between Air Quality and Climate Change, Chem Rev, 115(10), 3856-3897, doi:10.1021/acs.chemrev.5b00089.

Vreeland, H., J. J. Schauer, A. G. Russell, J. D. Marshall, A. Fushimi, G. Jain, K. Sethuraman, V. Verma, S. N. Tripathi, and M. H. Bergin (2016), Chemical characterization and toxicity of particulate matter emissions from roadside trash combustion in urban India, Atmospheric Environment, 147, 22-30, doi:10.1016/j.atmosenv.2016.09.041.

Wang, A., J. Xu, R. Tu, M. Saleh, and M. Hatzopoulou (2020a), Potential of machine learning for prediction of traffic related air pollution, Transportation Research Part D: Transport and Environment, 88, doi:10.1016/j.trd.2020.102599.

Wang, J., J. Li, X. Wang, J. Wang, and M. Huang (2020b), Air quality prediction using CT-LSTM, Neural Computing and Applications, 33(10), 4779-4792, doi:10.1007/s00521-020-05535-w.

Wang, Q., Han, Y., Ye, J., Liu, S., Pongpiachan, S., Zhang, N., Han, Y., Tian, J., Wu, C., Long, X., Zhang, Q., Zhang, W., Zhao, Z., and Cao, J.: High Contribution of Secondary Brown Carbon to Aerosol Light Absorption in the Southeastern Margin of Tibetan Plateau, Geophysical Research Letters, 46(9), 4962-4970, doi:10.1029/2019gl082731, 2019.

Wang, S., Y. Ren, and B. Xia (2023), PM2.5 and O3 concentration estimation based on interpretable machine learning, Atmos Pollut Res, 14(9), doi:10.1016/j.apr.2023.101866.

Wang, Y., P. Liu, Y. J. Li, A. P. Bateman, S. T. Martin, and H. M. Hung (2018), The Reactivity of Toluene-Derived Secondary Organic Material with Ammonia and the Influence of Water Vapor, J Phys Chem A, 122(38), 7739-7747, doi:10.1021/acs.jpca.8b06685.

Wang, Z., Saade, N. K., & Ariya, P. A. (2021). Advances in Ultra-Trace Analytical Capability for Micro/Nanoplastics and Water-Soluble Polymers in the Environment: Fresh Falling Urban Snow. *Environmental Pollution*, 276: 116698. https://doi.org/10.1016/j.envpol.2021.116698

Washenfelder, R. A., Attwood, A. R., Brock, C. A., Guo, H., Xu, L., Weber, R. J., et al. (2015). Biomass burning dominates brown carbon absorption in the rural southeastern United States. *Geophysical Research Letters*, 42(2): 653-664. https://doi.org/10.1002/2014GL062444

Wen, F., B. Li, H. Cao, P. Li, Y. Xie, F. Zhang, Y. Sun, and L. Zhang (2023a), Association of long-term exposure to air pollutant mixture and incident cardiovascular disease in a highly polluted region of China, Environ Pollut, 328, 121647, doi:10.1016/j.envpol.2023.121647.

Wen, F., Y. Xie, B. Li, P. Li, H. Qi, F. Zhang, Y. Sun, and L. Zhang (2023b), Combined effects of ambient air pollution and PM(2.5) components on renal function and the potential mediation effects of metabolic risk factors in China, Ecotoxicol Environ Saf, 259, 115039, doi:10.1016/j.ecoenv.2023.115039.

World Health Organization (2021 a): WHO global air quality guidelines: particulate matter (PM2.5 and PM10), ozone, nitrogen dioxide, sulfur dioxide and carbon monoxide.

WHO (2021b), *Air pollution*. https://www.who.int/health-topics/air-pollution#tab=tab_1.

WHO (2021c), *COVID-19 Situation Reports*. https://www.who.int/emergencies/diseases/novel-coronavirus-2019/situation-reports

Wu, C., C. He, Z. E. Brown, B. Miljevic, C. Zhang, H. Wang, B. Wang, L. Morawska, and Z. Ristovski (2023), Light absorption properties of black and brown carbon during the prescribed burning season at an urban background site in Brisbane, Australia, Atmospheric Environment, 313, doi:10.1016/j.atmosenv.2023.120072.

Wu, C., Wu, D., and Yu, J. Z.: Quantifying black carbon light absorption enhancement with a novel statistical approach, Atmospheric Chemistry and Physics, 18(1), 289-309, doi:10.5194/acp-18-289-2018, 2018.

Wu, G., X. Wan, S. Gao, P. Fu, Y. Yin, G. Li, G. Zhang, S. Kang, K. Ram, and Z. Cong (2018), Humic-Like Substances (HULIS) in Aerosols of Central Tibetan Plateau (Nam Co, 4730 m asl): Abundance, Light Absorption Properties, and Sources, Environ Sci Technol, 52(13), 7203-7211, doi:10.1021/acs.est.8b01251.

Xu, J., A. Wang, N. Schmidt, M. Adams, and M. Hatzopoulou (2020), A gradient boost approach for predicting near-road ultrafine particle concentrations using detailed traffic characterization, Environ Pollut, 265(Pt B), 114777, doi:10.1016/j.envpol.2020.114777.

Xu, J., Zhang, J., Liu, J., Yi, K., Xiang, S., Hu, X., et al. (2019). Influence of cloud microphysical processes on black carbon wet removal, global distributions, and radiative forcing. *Atmospheric Chemistry and Physics*, 19(3): 1587-1603. https://doi.org/10.5194/acp-19-1587-2019

Xu, R., Ye, T., Yue, X., Yang, Z., Yu, W., Zhang, Y., Bell, M. L., Morawska, L., Yu, P., Zhang, Y., Wu, Y., Liu, Y., Johnston, F., Lei, Y., Abramson, M. J., Guo, Y., and Li, S.: Global population exposure to landscape fire air pollution from 2000 to 2019, Nature, 621(7979), 521-529, doi:10.1038/s41586-023-06398-6, 2023.

Xu, X., Yang, X., Zhu, B., Tang, Z., Wu, H., & Xie, L. (2020). Characteristics of MERRA-2 black carbon variation in east China during 2000–2016. *Atmospheric Environment*, 222, 117140. https://doi.org/10.1016/j.atmosenv.2019.117140

Yan, R., J. Liao, J. Yang, W. Sun, M. Nong, and F. Li (2021), Multi-hour and multi-site air quality index forecasting in Beijing using CNN, LSTM, CNN-LSTM, and spatiotemporal clustering, Expert Systems with Applications, 169, doi:10.1016/j.eswa.2020.114513.

Yang, F., Tan, J., Zhao, Q., Du, Z., He, K., Ma, Y., et al. (2011). Characteristics of PM 2.5 speciation in representative megacities and across China. *Atmospheric Chemistry and Physics*, 11(11): 5207-5219. https://doi.org/10.5194/acp-11-5207-2011

Yang, S., Hong, F., Li, S., Han, X., Li, J., Wang, X., Chen, L., Zhang, X., Tan, X., Xu, J., Duoji, Z., Ciren, Z., Guo, B., Zhang, J., and Zhao, X.: The association between chemical constituents of ambient fine particulate matter and obesity in adults: A large population-based cohort study, Environ Res, 231(Pt 2), 116228, doi:10.1016/j.envres.2023.116228, 2023.

Yu, G., A. R. Bayer, M. M. Galloway, K. J. Korshavn, C. G. Fry, and F. N. Keutsch (2011), Glyoxal in aqueous ammonium sulfate solutions: products, kinetics and hydration effects, Environ Sci Technol, 45(15), 6336-6342, doi:10.1021/es200989n.

Zhang, F., et al. (2020), An unexpected catalyst dominates formation and radiative forcing of regional haze, Proc Natl Acad Sci U S A, 117(8), 3960-3966, doi:10.1073/pnas.1919343117.

Zhang, Q., Shen, Z., Lei, Y., Zhang, T., Zeng, Y., Ning, Z., et al. (2019). Optical properties and source identification of black carbon and brown carbon: comparison of winter and summer haze episodes in Xi'an, Northwest China. *Environmental Science: Processes & Impacts*, 21, 2058-2069. https://doi.org/10.1039/C9EM00320G

Zhang, R., Zhang, Y., Lin, H., Feng, X., Fu, T. M., & Wang, Y. (2020). NO_x Emission Reduction and Recovery during COVID-19 in East China. *Atmosphere*, 11(4), 433. https://doi.org/10.3390/atmos11040433

Zhang, X., Tao, J., Lei, F., Sun, T., Lin, L., Huang, X., Zhang, P., Ji, Y.X., Cai, J., Zhang, X. J., and Li, H. (2023a), Association of the components of ambient fine particulate matter (PM(2.5)) and chronic kidney disease prevalence in China, J Environ Manage, 339, 117885, doi:10.1016/j.jenvman.2023.117885.

Zhang, Y., et al. (2023b), Strong Haze-Black Carbon-Climate Connections Observed Across Northern and Eastern China, Journal of Geophysical Research: Atmospheres, 128(16), doi:10.1029/2023jd038505.

Zhang, Z., Y. Cheng, L. Liang, and J. Liu (2023c), The Measurement of Atmospheric Black Carbon: A Review, Toxics, 11(12), doi:10.3390/toxics11120975.

Zhong, M., Xu, J., Wang, H., Gao, L., Zhu, H., Zhai, L., Zhang, X., and Zhao, W.: Characterizing water-soluble brown carbon in fine particles in four typical cities in northwestern China during wintertime: integrating optical properties with chemical processes, Atmospheric Chemistry and Physics, 23(19), 12609-12630, doi:10.5194/acp-23-12609-2023, 2023.

Zhong, S., et al. (2021), Machine Learning: New Ideas and Tools in Environmental Science and Engineering, Environ Sci Technol, 55(19), 12741-12754, doi:10.1021/acs.est.1c01339.

Zhou, W., et al. (2022), Unexpected Increases of Severe Haze Pollution During the Post COVID-19 Period: Effects of Emissions, Meteorology, and Secondary Production, Journal of Geophysical Research: Atmospheres, 127(3), doi:10.1029/2021jd035710.

Zhu, J. J., M. Yang, and Z. J. Ren (2023), Machine Learning in Environmental Research: Common Pitfalls and Best Practices, Environ Sci Technol, doi:10.1021/acs.est.3c00026.

Zotter, P., Herich, H., Gysel, M., El-Haddad, I., Zhang, Y., Močnik, G., Hüglin, C., Baltensperger, U., Szidat, S., and Prévôt, A. S. H.: Evaluation of the absorption Ångström exponents for traffic and wood burning in the Aethalometer-based source apportionment using radiocarbon measurements of ambient aerosol, Atmospheric Chemistry and Physics, 17(6), 4229-4249, doi:10.5194/acp-17-4229-2017, 2017.